

ISSN 2732-0189 (Online)
ISSN 1586-2070 (Print)

JOURNAL OF COMPUTATIONAL AND APPLIED MECHANICS

An Open Access International Journal

Published by the University of Miskolc

VOLUME 15, NUMBER 1 (2020)



MISKOLC UNIVERSITY PRESS

ISSN 2732-0189 (Online)
ISSN 1586-2070 (Print)

JOURNAL OF COMPUTATIONAL AND APPLIED MECHANICS

An Open Access International Journal

Published by the University of Miskolc

VOLUME 15 NUMBER 1 (2020)



MISKOLC UNIVERSITY PRESS

EDITORS

László **BARANYI**, Institute of Energy Engineering and Chemical Machinery, University of Miskolc, H-3515 MISKOLC, Hungary, e-mail: arambl@uni-miskolc.hu

István **PÁCZELT**, Institute of Applied Mechanics, University of Miskolc, H-3515 MISKOLC, Hungary e-mail: mechpacz@uni-miskolc.hu

György **SZEIDL**, Institute of Applied Mechanics, University of Miskolc, H-3515 MISKOLC, Hungary e-mail: Gyorgy.SZEIDL@uni-miskolc.hu

EDITORIAL BOARD

Edgár **BERTÓTI**, Institute of Applied Mechanics, University of Miskolc, H-3515 MISKOLC, Hungary, e-mail: edgar.bertoti@uni-miskolc.hu

Attila **BAKSA**, Institute of Applied Mechanics, University of Miskolc, H-3515 MISKOLC, Hungary, attila.baksa@uni-miskolc.hu

István **ECSEDI**, Institute of Applied Mechanics, University of Miskolc, H-3515 MISKOLC, Hungary, mechecs@uni-miskolc.hu

Ulrich **GABBERT**, Institut für Mechanik, Otto-von-Guericke-Universität Magdeburg, Universitätsplatz 2, 39106 MAGDEBURG, Germany, ulrich.gabbert@mb.uni-magdeburg.de

Zsolt **GÁSPÁR**, Department of Structural Mechanics, Budapest University of Technology and Economics, Műegyetem rkp. 3, 1111 BUDAPEST, Hungary, gaspar@ep-mech.me.bme.hu

Robert **HABER**, Department of Theoretical and Applied Mechanics, University of Illinois at Urbana-Champaign, 216 Talbot Lab., 104 S. Wright St., URBANA, IL 61801, USA, r-haber@uiuc.edu

Csaba **HŐS**, Department of Hydraulic Machines, Budapest University of Technology and Economics, Műegyetem rkp. 3, 1111 BUDAPEST, Hungary, hosc_saba@vizgep.bme.hu

Károly **JÁRMAI**, Institute of Energy Engineering and Chemical Industry, University of Miskolc, H-3515 MISKOLC, Hungary, altjar@uni-miskolc.hu

László **KOLLÁR**, Department of Structural Engineering, Budapest University of Technology and Economics, Műegyetem rkp. 3. K.II.42., 1521 BUDAPEST, Hungary, lkollar@eik.bme.hu

József **KÖVECSES**, Mechanical Engineering Department 817 Sherbrooke Street West, MD163 MONTREAL, Quebec H3A 2K6 jozsef.kovecses@mcgill.ca

Márta **KURUTZ**, Department of Structural Mechanics, Budapest University of Technology and Economics, Műegyetem rkp. 3, 1111 BUDAPEST, Hungary, kurutzm@eik.bme.hu

Lin **LU**, Center for Deepwater Engineering, Dalian University of Technology, Dalian, China lulin@dlut.edu.cn

Herbert **MANG**, Institute for Strength of Materials, University of Technology, Karlsplatz 13, 1040 VIENNA, Austria, Herbert.Mang@tuwien.ac.at

Sanjay **MITTAL**, Department of Aerospace Engineering, Indian Institute of Technology, KANPUR, UP 208 016, India, smittal@iitk.ac.in

Zenon **MRÓZ**, Polish Academy of Sciences, Institute of Fundamental Technological Research, Swietokrzyska 21, WARSAW, Poland zmroz@ippt.gov.pl

Gyula **PATKÓ**, Institute of Machine Tools and Mechatronics, University of Miskolc, H-3515 MISKOLC, Hungary, patko@uni-miskolc.hu

Jan **SLADEK**, Ústav stavbenictva a architektúry, Slovenskej akadémie vied, Dubróvska cesta 9, 842 20 BRATISLAVA, Slovakia, usarslad@savba.sk

Gábor **STÉPÁN**, Department of Applied Mechanics, Budapest University of Technology and Economics, Műegyetem rkp. 3, 1111 BUDAPEST, Hungary, stepan@mm.bme.hu

Barna **SZABÓ**, Department of Mechanical Engineering and Materials Science, Washington University, Campus Box 1185, ST. LOUIS, MO 63130, USA, szabo@wustl.edu

Balázs **TÓTH**, Institute of Applied Mechanics, University of Miskolc, 3515 MISKOLC, Hungary, balazs.toth@uni-miskolc.hu

HONORARY EDITORIAL BOARD MEMBERS

Tibor **CZIBERE**, Department of Fluid and Heat Engineering, University of Miskolc, H-3515 Miskolc-Egyetemváros, Hungary

Gábor **HALÁSZ**, Department of Hydraulic Machines, Budapest University of Technology and Economics, Műegyetem rkp. 3, 1111 BUDAPEST, Hungary,

NEW STABLE, EXPLICIT, FIRST ORDER METHOD TO SOLVE THE HEAT CONDUCTION EQUATION

ENDRE KOVÁCS

Department of Physics and Electrical Engineering, University of Miskolc
H-3515 Miskolc-Egyetemváros, Hungary
kendre01@gmail.com

[Received: May 29, 2020, Accepted: June 12, 2020]

Abstract. In this paper a novel explicit and unconditionally stable numerical algorithm is introduced to solve the inhomogeneous non-stationary heat or diffusion equation. Spatial discretization of these problems usually yields huge and stiff ordinary differential equation systems, the solution of which is still time-consuming. The performance of the new method is compared with analytical and numerical solutions. It is proven exactly as well as demonstrated numerically that the new method is first order in time and can give approximate results for extremely large systems faster than the commonly used explicit or implicit methods. The new method can be easily parallelized and it is handy to apply regardless of space dimensions and grid irregularity

Mathematical Subject Classification: 65L04, 65N40, 80M25

Keywords: Heat equation, explicit methods, stable schemes, stiff equations

1. INTRODUCTION

It is well known that the simplest Fourier-type heat conduction phenomena are described by the heat equation, which is a second-order parabolic partial differential equation (PDE), with the following form.

$$\frac{\partial T}{\partial t} = \alpha \nabla^2 T + q,$$

where $\alpha = k/(c\rho) > 0$ is the thermal diffusivity, q , k , c and ρ are the volumetric intensity of heat sources (radiation, chemical reactions radioactive decay, etc.), heat conductivity, specific heat and (mass) density, respectively. This equation describes heat conduction in solid materials, not only in the walls of residential buildings but in different kinds of technical equipment like chimneys, heat exchangers and electronic circuits as well.

The PDEs for real-life problems can rarely be solved analytically. The new numerical procedure starts like the standard method of lines: the whole spatial domain is divided into smaller cells. However, this discretization must reflect the material properties of the system, thus we perform it more generally than numerical analysis textbooks usually do. We calculate three quantities for each cell. The first one is the heat capacity of the cell: $C = cm = c\rho V$, where m is the mass, V is the volume

of the cell. Now the (thermal) energy of a cell can be expressed as $C_i T_i$, where T_i is the average temperature of the cell. The second quantity is the heat or thermal conductance U , which can be approximated as

$$U_{ij} \approx k \frac{A_{ij}}{d_{ij}},$$

where A_{ij} is the surface area between the two cells i and j , while d_{ij} is the distance between the centres of the cells. In a one dimensional non-uniform grid, $d_{ij} = (\Delta x_i + \Delta x_j) / 2$. The third quantity is Q_i , the heat source term:

$$Q_i = \frac{1}{V_i} \int_{V_i} q dV, \quad \text{in } \left[\frac{\text{K}}{\text{s}} \right] \text{ units.}$$

After the discretization of the second spatial derivatives according to the most common second order central difference formula, we obtain an ordinary differential equation (ODE) system which gives the time derivative of each cell's temperature

$$\frac{dT_i}{dt} = \sum_{j=\text{neigh}} \frac{U_{ij}}{C_i} (T_j - T_i) + Q_i,$$

where the summation is carried out for the neighboring the cells. We can write it in a matrix form:

$$\frac{d\vec{T}}{dt} = M\vec{T} + \vec{Q}. \quad (1)$$

To help the reader visualize, we present the arrangement of the variables in Figure 1 for a 2D system of 3 cells.

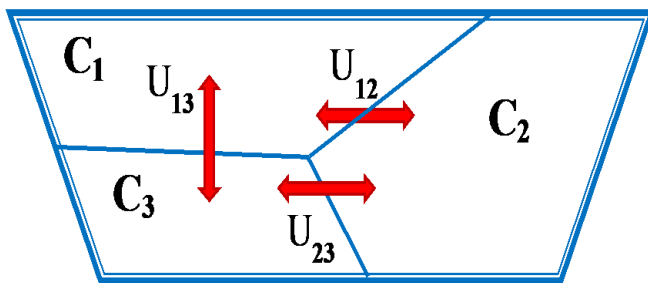


Figure 1. Notations in the case of three cells. The outer double line represents thermal isolation. Note that the shape and arrangement of the cells are not necessarily regular.

The ODE system in a matrix form for this small system:

$$\frac{d\vec{T}}{dt} = \begin{bmatrix} -\frac{U_{12}}{C_1} - \frac{U_{13}}{C_1} & \frac{U_{12}}{C_1} & \frac{U_{13}}{C_1} \\ \frac{U_{12}}{C_2} & -\frac{U_{12}}{C_2} - \frac{U_{23}}{C_2} & \frac{U_{23}}{C_2} \\ \frac{U_{13}}{C_3} & \frac{U_{23}}{C_3} & -\frac{U_{13}}{C_3} - \frac{U_{23}}{C_3} \end{bmatrix} \vec{T} + \begin{bmatrix} Q_1 \\ Q_2 \\ Q_3 \end{bmatrix}.$$

Suppose now that one quickly needs approximate results about the temperature distribution as a function of time in an extremely large and complicated system, where the physical properties of the material like the specific heat and the thermal diffusivity widely vary from point to point. In this case the size of the matrix is huge, while the magnitude of the matrix elements and that of the eigenvalues has a range of several orders of magnitude, which means it is an extremely stiff system. Which method can be recommended to solve this problem?

It is widely believed that conventional explicit methods are inappropriate because of unacceptably small timesteps due to stiffness [1, 2]. That is why implicit methods are almost exclusively used in the industry [3], as they have excellent stability properties. The famous book of Hairer and Wanner [4] even devotes a separate, second volume to stiff (and differential-algebraic) problems, where they almost exclusively deal with implicit methods. The disadvantage of the implicit methods is that they require the solution of an algebraic equation system at each time-step, predominantly by iterative methods, which is slow because of the necessity to store and handle huge matrices. Moreover, parallelization of implicit methods is not straightforward, although some moderate progress has been achieved [5–7]. However, as the clock frequency increase of CPUs has significantly slowed down in the last two decades, parallel programming has become the dominant paradigm in high performance computing [8]. The easily parallelizable explicit methods with better stability properties like Runge–Kutta–Chebyshev, ADE (Alternating Direction Explicit), Hopscotch or Dufort–Frankel methods are very rarely used, as they usually have other disadvantages: they can hardly be applied for irregular grids, they can be rather inaccurate, complicated to implement, or they can only be conditionally consistent [2, 9–13].

We have to conclude that conventional methods provide no convenient solution. In order to fill this gap and solve these systems more effectively, we started to elaborate a family of fundamentally new explicit methods. The simplest version for transient problems (i.e. when $q \equiv 0$) has already been published [14]. The version of the algorithm and the logic by which we obtained that algorithm was not suitable for further work, i.e. for the generalization of the method. Moreover, [14] contains no verification by comparing the results to analytical solutions, and the proof for the rate of the convergence is presented only in the current paper. The numerical results presented here are for a larger and stiffer system than those shown in [14].

2. THE PROPOSED METHOD

Now we introduce the core method to solve the ODE system (1) through the following two steps:

1. We make a simplification: when we calculate the new value of a variable T_i , we neglect the fact that other variables are also changing during the timestep. This means that we consider T_j a constant if $j \neq i$, thus we can call it “constant-neighbour method”, abbreviated by CN. So we have to solve uncoupled, linear ODEs:

$$T_i' = a_i - T_i/\tau_i \quad (2)$$

where

$$a_i = \sum_{j \neq i} m_{ij} T_{0,j} + Q_i$$

is considered as a constant. We also introduce

$$\tau_i = -\frac{1}{m_{ii}} = \frac{C_i}{\sum_{j=neigh} U_{ij}},$$

which is a time-constant for the cells, while $T_{0,j}$ is the initial temperature.

2. The equations obtained are solved analytically. The analytical solution of equation (2) is given by

$$T_i(t) = T_{0,i} e^{-\frac{t}{\tau_i}} + a_i \tau_i \left(1 - e^{-\frac{t}{\tau_i}}\right).$$

Thus the following simple formula is proposed to obtain the values of T at the end of the first timestep using the values of $T_{0,i}$ only at the beginning of the timestep:

$$T_i(h) = \left\{ T_{0,i} e^{-\frac{h}{\tau_i}} + \frac{\sum_{j=neigh} U_{ij} T_{0,j}}{\sum_{j=neigh} U_{ij}} \left(1 - e^{-\frac{h}{\tau_i}}\right) \right\} + Q_i \tau_i \left(1 - e^{-\frac{h}{\tau_i}}\right). \quad (3)$$

Using the identity $e^x = 1 + (e^x - 1)$ and the definition of τ , we can write (3) into the following form

$$\begin{aligned} T_i(h) &= T_{0,i} + \left\{ \frac{m_{ii}}{T_{0,i}} m_{ii} + \frac{\sum_{j \neq i} m_{ij} T_{0,j}}{m_{ii}} + \frac{Q_i}{m_{ii}} \right\} (e^{m_{ii} h} - 1) = \\ &= T_{0,i} + \left(\sum_j m_{ij} T_{0,j} + Q_i \right) \frac{e^{m_{ii} h} - 1}{m_{ii}}. \end{aligned}$$

Now one can see that this algorithm looks similar to the explicit Euler method, which would give:

$$\vec{T}(h) = \vec{T}_0 + h \left(M \vec{T}_0 + \vec{Q} \right),$$

which shows than in our case $(e^{m_{ii}h} - 1)/m_{ii}$ stand for h . Using the power series of the exponential function, we can write

$$(e^{m_{ii}h} - 1)/m_{ii} = h + m_{ii} \frac{h^2}{2} + \dots$$

which means that, regarding one timestep, the new method is identical to the explicit Euler method up to first order. However, because of the exponential terms, formula (3) contains h up to infinite order, which is crucial for the unconditional stability.

The first two terms on the right hand side of (3), in curly brackets describe the transient process. As physically justifiable, the temperature of each cell exponentially tends to the temperature of its neighbors: the new value of the variable T_i is the weighted average of the old value of T_i and its neighbors T_j . It is easy to see that the coefficients of the initial temperatures $T_{0,j}$ are non-negative and the sum of them is 1. That is why the result is always bounded: the method cannot be unstable for the heat conduction equation. It is also obvious that the new method is explicit, one can calculate the new values without solving a system of equations or even without using matrices. It also implies that the process is obviously parallelizable and hopefully even vectorizable. Moreover, it can be easily applied regardless of the number of space dimensions, grid irregularity or inhomogeneity of the heat conduction medium. To examine the performance of the method, several numerical tests have been made, but here we present only two different examples.

3. VERIFICATION: COMPARISON WITH AN EXACT RESULT

If there are only two variables and one heat source, equation (1) has the following analytical solution

$$\begin{aligned} T_1(t) &= T_{0,1} \exp(-t/\tau) + T_a (1 - \exp(-t/\tau)) + St + S\tau \frac{C_2}{C_1} (1 - \exp(-t/\tau)) , \\ T_2(t) &= T_{0,2} \exp(-t/\tau) + T_a (1 - \exp(-t/\tau)) + St - S\tau (1 - \exp(-t/\tau)) , \end{aligned}$$

where

$$\tau = \frac{C_1 C_2}{U(C_1 + C_2)}, \quad T_a = \frac{T_{0,1} C_1 + T_{0,2} C_2}{C_1 + C_2} \quad \text{and} \quad S = \frac{Q_1}{C_1 + C_2}$$

are the common time constant, the final temperature without external source (weighted average of the initial temperatures) and the common increment of the temperatures due to the Q_1 source in one time unit, respectively. The results obtained by the new method fit the exact values very well at the final time t_{fin} . An example for the errors as a function of the stepsize is presented in Figure 2. Error here means the absolute value of the difference between the exact temperature and the temperature obtained by the new method $|T^{\text{ex}}(t_{\text{fin}}) - T^{\text{CN}}(t_{\text{fin}})|$.

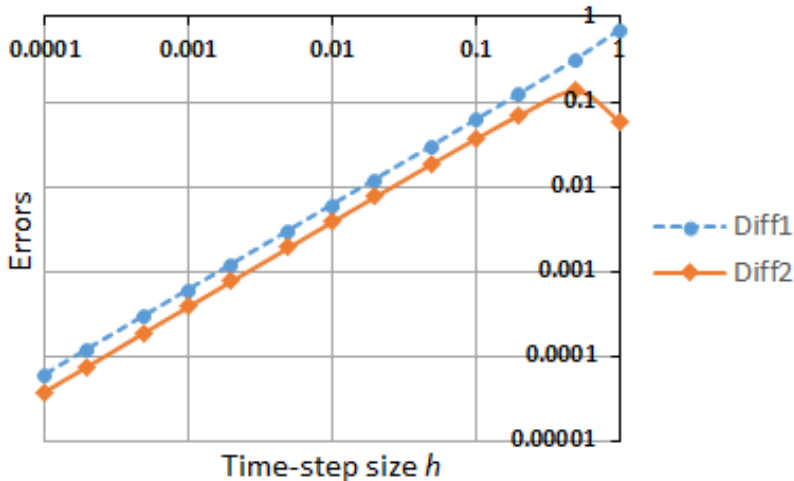


Figure 2. Absolute value of errors as a function of the timestep size for $U = 0$, $C_1 = 5$, $C_2 = 1$, $T_{01} = 10$, $T_{02} = 0$, $Q_1 = 8$ and $t_{\text{fin}} = 1$. Diff1 is for the first, Diff2 is for the second cell.

It is well known that a method is called p^{th} order if the local error is $O(h^{p+1})$ or (equivalently for normal systems) if the global error is $O(h^p)$. It can be seen from Figure 2 that the global error decreases with the first power of the stepsize, thus one can conclude that this method is first order. The analytical proof of this statement is presented in the Appendix.

4. COMPARISON WITH NUMERICAL RESULTS FOR A STIFF SYSTEM

The second system is a regular rectangle-shaped lattice, $N_x = 100$, $N_y = 50$. A value $10^{(3-7 \times \text{rand})}$ is given to the capacities C_i and to the inverse conductances $1/U_{xi}$, $1/U_{yi}$ (the resistances), where rand is a random number generated by MATLAB uniformly in the $(0, 1)$ interval for each quantity. This means that the capacities (the resistances) follow a log-uniform distribution between 0.0001 and 1000. The initial temperatures are uniformly zero, the sources have a uniform distribution between 0 and 100, $Q_i = 100 \times (1 - \text{rand})$. The task is to solve this system for the temperatures between $t_0 = 0$ s and $t_{\text{FIN}} = 10$ s.

It is well known that the stiffness ratio is the ratio of the extreme eigenvalues $\lambda_{\min}/\lambda_{\max}$, where λ_{\min} (λ_{\max}) is the (negative) eigenvalue of the matrix with the largest (smallest) absolute value. In this case the stiffness ratio is 7.6×10^{12} , which means that this is a seriously stiff problem. For the explicit Euler method (which is equivalent to the forward-time central-space FTCS scheme), the maximum possible timestep is

$$h_{\text{MAX}}^{\text{E}} = |2/\lambda_{\max}| = 1.45 \times 10^{-8} \text{ s}.$$

Note that above this threshold instability necessarily occurs. For this system, the widely used (conditionally stable) explicit methods are impractical, as they would require at least a day to reach any result. Therefore, to provide a reference solution, an implicit ode15s solver of MATLAB has been used, which is variable-step, variable-order, based on the numerical differentiation formulas (NDFs) of orders 1 to 5, where the letter *s* indicates that the codes were designed especially for stiff systems. With strict error tolerance ('RelTol' = 10^{-8} , 'AbsTol' = 10^{-7}), our computer needs 677 s to give a high precision solution using this routine.

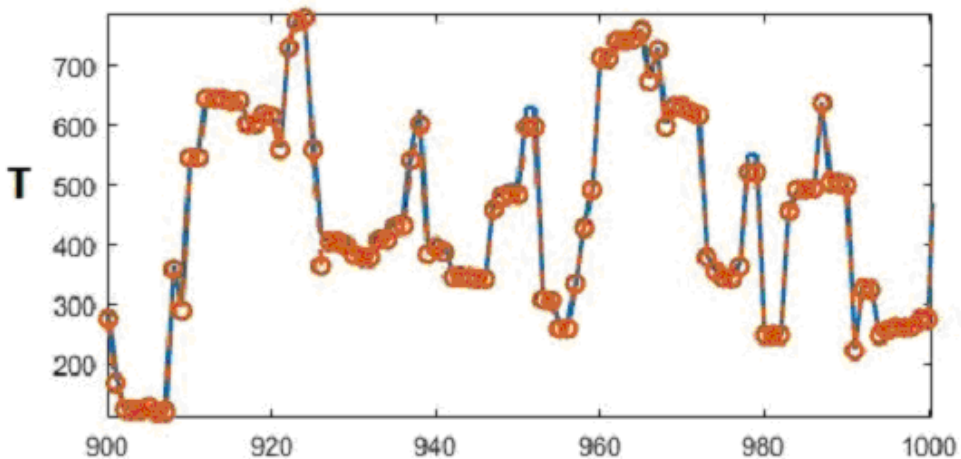


Figure 3. A randomly selected part of the graph of the temperature as a function of the space variable. The blue line is the high-precision solution while the orange circles are the values produced by the new algorithm for $h = 0.0002$.

With the new “constant-neighbour” method, one timestep takes roughly 0.0004 s. We found that if $h = 0.0002$, then the produced results already fit quite well to the exact curve. The result is presented in Figure 3. One can see that it is possible to obtain a reasonable solution in $t_{\text{FIN}} \times 0.0004 \text{ s}/h \approx 20 \text{ s}$ (in reality, 14 s), much faster than the conventional explicit or implicit methods.

In Table 1 some results obtained by MATLAB routines ode15s, ode23s and the new method, are summarised. We note that no matter how huge the error tolerance is set to enhance speed, we were not able to obtain any results in 3 minutes by any MATLAB routines. From the data one can see that when a larger error tolerance is set, the new method is at least comparable with the standard solvers.

Table 1. Performance of 3 different solvers, CN is for “Constant-Neighbour”. The first error quantity, MaxD, is the maximum deviation (absolute value of the difference) from the reference solution. The second one, SumD, is the sum of these deviations for all of the cells.

Method	Runtime (s)	MaxD	SumD
ode15s	181	7.7	4890
ode15s	248	0.49	266.4
ode15s	400	0.001	0.506
ode23s	2112	0.146	79.6
CN, 2×10^{-4}	14	340.9	38702
CN, 2×10^{-5}	142	36.65	3570
CN, 10^{-4}	307	15.75	1715
CN, 10^{-6}	556	7.06	823

On the other hand, if a high-precision solution is needed, then the proposed method could not be recommended, but first order methods are not for this purpose, anyway. However, the following facts should be emphasized:

- This is still a small system with 5000 cells, and for larger numbers of cells implicit methods have more serious drawbacks. We note that the reason we have not used larger systems for testing purposes is that our computer cannot solve them by implicit methods because of the huge memory requirements.
- This is the simplest, “raw” version of the new method, without any optimization, adaptive stepsize control, parallelization or vectorization, which could immensely enhance computing speed.

In Figure 4 we present the two different kinds of error as a function of the stepsize h . One can see that for smaller stepsizes, the errors are decreasing slightly faster than the stepsize, which underpins that the convergence-rate of the method is (at least) one.

It can be seen that the error function is almost horizontal at the right side of Figure 4. The reason for this is that there are tiny cells with very small time constant τ , which means that their temperatures change very rapidly. In this case, the constant-neighbour approximation we used in Section 2 step 1 is very crude for large time-step sizes and the method underestimates the speed of the processes in the system. The right side of the diagram also reinforces the statement that the method is stable for arbitrarily large step sizes, as the error does increase quite slowly with increasing stepsize and tends to a constant, thus they are always bounded and the method is stable.

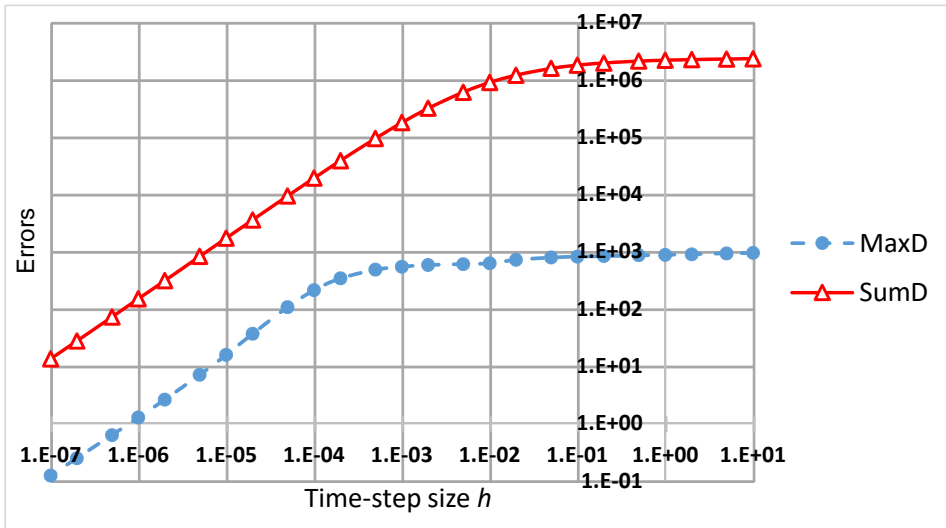


Figure 4. Different kinds of errors as function of the timestep size. For the definition of the error quantities, see the caption of Table 1.

5. SUMMARY

In this paper a new explicit numerical algorithm was presented to solve the time-dependent heat conduction or diffusion equation with external sources. After the spatial discretization of these parabolic partial differential equations, one obtains systems of ordinary differential equations which consist of several equations and which can be extremely stiff. When applied to these equation systems, the new method is unconditionally stable and first order in time. The performance of the method has been illustrated for a simple, analytically soluble case and in the case of a two-dimensional system with highly inhomogeneous random parameters. The obtained data suggest that if quick results are required for a huge number of cells, the new method has a remarkable advantage, even without parallelization. We have also proven analytically that the method is first order in time. We note that we are currently working on the second order version and also on extending the method to equations with other terms besides the diffusion term.

REFERENCES

1. U. M. Ascher, S. J. Ruuth, and B. T. R. Wetton. “Implicit-explicit methods for time-dependent partial differential equations.” *SIAM Journal on Numerical Analysis*, **32**(3), (1995), pp. 797–823. DOI: 10.1137/0732037.
2. Vabishchevich P. N. and Zakharov P. E. “Explicit-implicit splitting schemes for parabolic equations and systems.” *Lecture Notes in Computer Science*, 2015. DOI: 10.1007/978-3-319-15585-2_18.

3. M. Cusini. “Dynamic Multilevel Methods for Simulation of Multiphase Flow in Heterogeneous Porous Media.” PhD. Delft University of Technology, 2019. DOI: 10.4233/uuid:c624cd58-25e0-4bf9-bf36-025e08c46169.
4. E. Hairer and G. Wanner. *Solving Ordinary Differential Equations II. Stiff and Differential-Algebraic Problems*. Berlin: Springer-Verlag, 1991. DOI: 10.1007/978-3-319-15585-2_18.
5. M. S. A. Taj. “Higher Order Parallel Splitting Methods for Parabolic Partial Differential Equations.” PhD. Brunel University, Uxbridge, England, 1995.
6. A. B. Gumel, W. T. Ang, and E. H. Twizell. “Efficient parallel algorithm for the two-dimensional diffusion equation subject to specification of mass.” *International Journal of Computer Mathematics*, **64**, (1997), pp. 153–163. DOI: 10.1080/00207169708804580.
7. G. Xue and H. Feng. “A new parallel algorithm for solving parabolic equations.” *Advances in Difference Equations*, **20**(1), (2018). DOI: 10.1186/s13662-018-1617-8.
8. G. Martin, B. Bailey, and A. Piziali. *ESL Design and Verification: A Prescription for Electronic System Level Methodology*. Elsevier, 2010.
9. L. Skvortsov. “Explicit stabilized Runge-Kutta methods.” *Computational Mathematics and Mathematical Physics*, **51**(7), (2011), pp. 1153–1166. DOI: 10.1134/S0965542511070165.
10. J. G. Verwer, W. H. Hundsdorfer, and B. P. Sommeijer. “Convergence properties of the Runge-Kutta-Chebyshev method.” *Numerische Mathematik*, **57**(1), (1990), 157–178. DOI: 10.1007/BF01386405.
11. M. N. Özisik, H. R. B. Orlande, M. J. Colaço, and R. M. Cotta. *ESL Design and Verification: A Prescription for Electronic System Level Methodology*. Boca Raton: CRC Press, 2010. DOI: 10.1201/9781315121457.
12. M. Hochbruck and A. Ostermann. “Exponential integrators.” *Acta Numerica*, **19**, (2010), pp. 209–286. DOI: 10.1017/S0962492910000048.
13. A. R. Gourlay and S. McKee. “The construction of hopscotch methods for parabolic and elliptic equations in two space dimensions with a mixed derivative.” *Journal of Computational and Applied Mathematics*, **3**,(3) (1977), pp. 201–206. DOI: 10.1016/S0377-0427(77)80009-5.
14. E. Kovács and A. Gilicz. “New stable method to solve heat conduction problems in extremely large systems.” *Design of Machines and Structures*, **8**,(2) (2018), pp. 30–38. DOI: 10.1016/S0377-0427(77)80009-5.

APPENDIX A. THE PROOF THAT THE METHOD IS FIRST ORDER IN TIME

Using the power series form of the exponential function, the exact solution of (1) is the following:

$$\begin{aligned} \vec{T}(t) &= e^{Mt}\vec{T}_0 + (e^{Mt} - 1)M^{-1}\vec{Q} = \\ &= \left(1 + Mt + M^2\frac{t^2}{2} + M^3\frac{t^3}{3!} + \dots\right)\vec{T}_0 + \left(t + M\frac{t^2}{2} + M^2\frac{t^3}{3!} + \dots\right)\vec{Q}. \end{aligned}$$

The 0^{th} and first order terms in the exact solution at $t = h$ are given by:

$$\begin{aligned} T_i(h) &= T_{0,i} (1 + m_{ii}h) + h \sum_{j \neq i} m_{ij} T_{0,j} + Q_i h = \\ &= T_{0,i} \left(1 - \frac{h}{\tau_i} \right) + h \sum_{j=neigh} \frac{U_{ij}}{C_i} T_{0,j} + Q_i h, \end{aligned}$$

where we used the fact that $U_{ij} \equiv 0$ if and only if the two cells are neighbours and thus the summation can be performed only to the neighbours. Let us compare it to the new ‘‘Constant Neighbour’’ solution. We obtain from (3) that

$$T_i(h) = T_{0,i} \left(1 - \frac{h}{\tau_i} + O(h^2) \right) + \left(\frac{\sum_{j=neigh} U_{ij} T_{0,j}}{\sum_{j=neigh} U_{ij}} + Q_i \tau_i \right) \left(1 - 1 + \frac{h}{\tau_i} - O(h^2) \right).$$

Considering only the 0^{th} and first order terms yields

$$\begin{aligned} T_i(h) &\approx T_{0,i} \left(1 - \frac{h}{\tau_i} \right) + \left(\frac{\sum_{j=neigh} U_{ij} T_{0,j}}{\sum_{j=neigh} U_{ij}} + Q_i \tau_i \right) \frac{h}{\tau_i} = \\ &= T_{0,i} \left(1 - \frac{h}{\tau_i} \right) + h \frac{\sum_{j=neigh} U_{ij} T_{0,j}}{\sum_{j=neigh} U_{ij}} \frac{\sum_{j=neigh} U_{ij}}{C_i} + Q_i h. \end{aligned}$$

After simplification we obtain the statement that the difference between the exact solution and the new method, i.e., the local error is second order in time.

AN INVESTIGATION ON TRANSMISSION LOSS OF CLAMPED DOUBLED THIN PLATE WITH ADDED MASS

AKINTOYE OLUMIDE OYELADE

Department of Civil and Environmental Engineering,
University of Lagos, Akoka, Lagos, Nigeria
aoyelade@unilag.edu.ng

[Received: March 16, 2019, Accepted: May 12, 2020]

Abstract. Thin plate acoustic metamaterials (TAM) have demonstrated uncommon capacity in controlling low-frequency sound transmission. This paper concentrates on a theoretical and experimental investigation of clamped double polylactic acid (PLA) thin plates with attached mass. The theoretical formulation was done using a rectangular duct below the first cut off frequency. The sound transmission loss (STL) of the plates is calculated for plane wave condition, then the accuracy and capability of the theoretical model is verified through the comparison with the finite element method and experiment. The influence of several key parameters on the STL of the double-panel configuration is then systematically studied, including thickness of air cavity, magnitude of mass attached, and mode shapes. New peak and dip frequencies are found for the TAM with attached masses. The developed model can serve as an efficient tool for the design of such thin plate metamaterials.

Mathematical Subject Classification: 74H45, 74K20

Keywords: Polylactic acid, acoustic metamaterials, sound transmission loss, clamped plate

1. INTRODUCTION

Double-leaf partition membranes and thin plates structures have found increasingly wide applications in sound control engineering due to their superior sound insulation capability over single-leaf configurations. Typical examples include automotive, marine, aircraft, construction industries and so on [1–3]. Double-wall structures, however, are less efficient at low frequency around the mass–air–mass resonance at which the model for infinite panels reveals an out-of-phase motion of the two walls [4]. Until quite recently, there has been a persistent effort to explore the prospect of using acoustic metamaterials to increase the transmission loss of double-wall partitions at low frequencies [5, 6]. In these works, analytical and numerical investigation of the STL features are controlled by the magnitude of the added mass and/or pretension of the membrane. However, only the effect of mass and tensions were examined, and no further detailed analysis and experimental verification were presented. Thus, to the author’s best knowledge, very few experimental studies have been reported on the coupled vibroacoustic problems of double thin plates with added mass in a rigid duct, and that would be solved in this paper. The thin plate acoustic metamaterial (TAM) can be described as an elastic plate carrying a concentrated mass or masses on each side. The vibration eigenfrequencies of the thin plate acoustic metamaterials

(TAM) can be tuned by varying the thin plate and mass properties. In this paper, we present the experimental realization and theoretical understanding of a double thin plate metamaterial with one mass resonator on each face to further study and verify the work carried out previously numerically. What distinguishes this study from others is that the effect of cavity gaps in relation with the attached mass and the mode shapes characteristics of the plates are investigated. In the first instance, a brief overview of the structural and acoustic models is presented. Results for the experiments, theory and numerical investigation are then presented and discussed, followed by concluding remarks.

2. THEORETICAL FORMULATION

Consider now TAM, as shown in Figure 1(a), where the thin plate is attached by N point masses on each plate. The case of $N = 1$ is illustrated in Figure 1(b), and the mass is located at (x_h, y_h) . The upper plate is excited by a plane harmonic sound wave. The two elastic thin plates are fully clamped along their edges to an infinite rigid acoustic baffle.

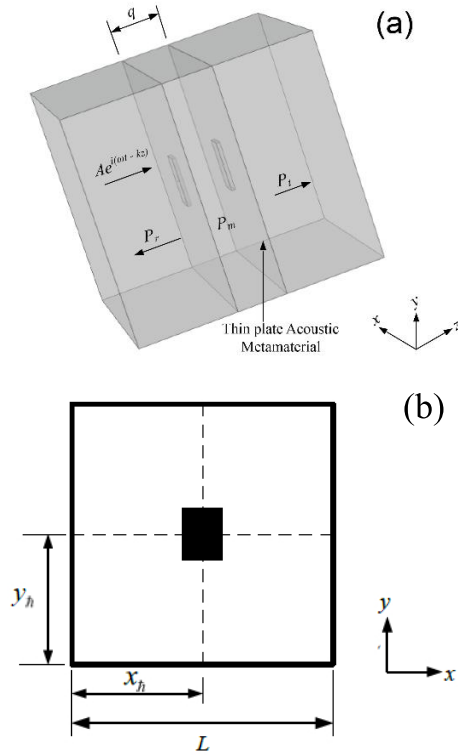


Figure 1. (a) TAM subjected to a plain wave loading in a rectangular duct (b) TAM attached with a centrally placed mass

The flexural motions equation of two thin plates connected each by N number of point masses and air cavity is given by

$$\begin{aligned} D_1 \nabla^4 \bar{\xi}_1 - M_1 \omega^2 \bar{\xi}_1 - \sum_{\hbar=1}^N \bar{M}_1 \omega^2 \bar{\xi}_1 \delta \{x - x_{\hbar}, y - y_{\hbar}\} = \\ = 2A + \sum_{m=0}^{N_m} \sum_{n=0}^{N_n} [e_{mn} - b_{mn} - c_{mn}] \cos(\pi m x / L) \cos(\pi n x / L) \end{aligned} \quad (1)$$

for panel 1, and

$$\begin{aligned} D_2 \nabla^4 \bar{\xi}_2 - \bar{M}_2 \omega^2 \bar{\xi}_2 - \sum_{\hbar=1}^N \bar{M}_2 \omega^2 \bar{\xi}_2 \delta \{x - x_{\hbar}, y - y_{\hbar}\} = \\ = \sum_{m=0}^{N_m} \sum_{n=0}^{N_n} [b_{mn} e^{-ik_z q} + c_{mn} e^{ik_z q} - d_{mn} e^{-ik_z q}] \cos(\pi m x / L) \cos(\pi n x / L) \end{aligned} \quad (2)$$

for panel 2. In the above equations $\bar{\xi}_1$, D_1 , M_1 and \bar{M}_1 are the transverse displacement, the flexible rigidity, the mass density and the discrete mass (attached) of panel 1, respectively. Symbols with subscript 2 have the same meanings as defined above but applied to panel 2. e_{mn} , b_{mn} , c_{mn} , d_{mn} and A are amplitude constants related to the waves in the duct as shown in Figure 1. This is given by Kim et al. [7]:

$$Q_1 = A e^{i(\omega t + k_z z)} + \sum_{m=0}^{N_r} \sum_{n=0}^{N_s} e_{mn} e^{i(\omega t + k_z z)} \cos(\pi m x / L) \cos(\pi n x / L), \quad (3)$$

$$Q_2 = \sum_{m=0}^{N_r} \sum_{n=0}^{N_s} [b_{mn} e^{i(\omega t - k_z z)} + c_{mn} e^{i(\omega t + k_z z)}] \cos(\pi m x / L) \cos(\pi n x / L), \quad (4)$$

$$Q_3 = \sum_{m=0}^{N_r} \sum_{n=0}^{N_s} d_{mn} e^{i(\omega t - k_z z)} \cos(\pi m x / L) \cos(\pi n x / L), \quad (5)$$

where L is the height of the plate, ω is the angular frequency, and $i = \sqrt{-1}$. Wave number k_z in z direction satisfies the following relation:

$$k_z = \left[k^2 - \frac{\pi^2 (m^2 + n^2)}{L^2} \right]^{1/2}, \quad (6)$$

which shows that the axial wavenumber k_z depends on m and n . When $m = n = 0$, which can be recognized as the one-dimensional sound field assumed in this work. The plane wave is the fundamental duct mode. The displacement of the plates

can be expressed as a harmonic function:

$$\xi_1 = \bar{\xi}_1 e^{i\omega t}, \xi_2 = \bar{\xi}_2 e^{i\omega t}. \quad (7)$$

At the air panel interface, the boundary conditions at thin plate surfaces give

$$\frac{1}{\rho} \frac{\partial Q}{\partial z} = -\frac{\partial^2 \xi_1}{\partial t^2} = \omega^2 \xi_1 \quad \text{at} \quad z = 0, \quad (8)$$

$$\frac{1}{\rho} \frac{\partial Q}{\partial z} = -\frac{\partial^2 \xi_2}{\partial t^2} = \omega^2 \xi_2 \quad \text{at} \quad z = q, \quad (9)$$

where ρ is the density of air. For clamped plates, the flexural displacements of the incident and radiating plates can be expressed as

$$\bar{\xi}_1(x, y) = \sum_{j=1}^7 a_j \Phi_j(x, y), \bar{\xi}_2(x, y) = \sum_{j=1}^7 T_j \Phi_j(x, y), \quad (10)$$

where $\Phi_j(x, y)$ is the j^{th} mode of the clamped plate. Approximate solution for the first 36-term modes as proposed by Young [8] is defined as

$$\Phi_j(x, y) = \sum_{r=1}^6 \sum_{s=1}^6 A_{rs}^j \phi_r(x) \phi_s(y), \quad (11)$$

where $\phi_r(y)$ is the r^{th} mode of the clamped beam vibration defined by the following relation:

$$\phi_r(x) = \cosh(\varepsilon_r x/L) - \cos(\varepsilon_r x/L) - \alpha_r \{ \sinh(\varepsilon_r x/L) - \sin(\varepsilon_r x/L) \} \quad (12)$$

in which parameter ε_r and α_r can be found in mechanics books [9, 10]. The natural frequency corresponding to the j^{th} mode is given by

$$\omega_j = \frac{\lambda_j h}{L^2} \sqrt{\frac{E}{12\rho_p(1-\nu^2)}}, \quad (13)$$

where h , E , ν and ρ_p are the thickness, Young modulus, Poisson ratio and density of the plate. The coefficients A_{rs}^j and λ_j are found in Leissa [11]. Using displacement functions in equation (7), equations (1) and (2) become

$$\begin{aligned} \sum_{j=1}^7 \bar{M}_1 a_j \{ \omega_j^2 - \omega^2 \} \Phi_j - \sum_{h=1}^N \bar{M}_1 \omega^2 a_j \delta \{ x - x_h, y - y_h \} \Phi_j = \\ = 2A - 2 \sum_{m=0}^{N_m} \sum_{n=0}^{N_n} b_{mn} \cos(\pi m x/L) \cos(\pi n x/L), \quad (14) \end{aligned}$$

$$\begin{aligned} \sum_{j=1}^7 \tilde{M}_2 T_j \{ \Omega_j^2 - \omega^2 \} \Phi_j - \sum_{\hbar=1}^N \tilde{M}_2 \omega^2 T_j \delta \{ x - x_{\hbar}, y - y_{\hbar} \} \Phi_j \\ = 2 \sum_{m=0}^{N_m} \sum_{n=0}^{N_n} c_{mn} e^{ik_z q} \cos(\pi m x / L) \cos(\pi n x / L), \end{aligned} \quad (15)$$

where ω_j and Ω_j are the natural frequencies of the j^{th} mode of plates 1 and 2, respectively. Multiply this equation by $\Phi_M(x, y)$ and integrate over the entire region. Then combining the acoustic part at low frequency can be obtained as [12]:

$$\tilde{M}_1 \Gamma_{jM} (\omega_j^2 - \omega^2) a_j - \tilde{M}_1 \omega^2 a_j Z_{jM} = 2\beta_{M,00} (A - b_{00}), \quad (16)$$

$$\tilde{M}_2 \Gamma_{jM} (\Omega_j^2 - \omega^2) T_j - \tilde{M}_2 \omega^2 T_j Z_{jM} = 2c_{00} \beta_{M,00} e^{ikq}, \quad (17)$$

$$b_{00} - c_{00} = \sum_{j=1}^7 i\rho c \omega a_j \beta_{j,00}, \quad (18)$$

$$b_{00} e^{-ikq} - c_{00} e^{ikq} = \sum_{j=1}^7 i\rho c \omega T_j \beta_{j,00}, \quad (19)$$

where

$$\begin{aligned} \Gamma_{jM} &= \frac{1}{L^2} \int_A \Phi_j(x, y) \Phi_M(x, y) dx dy, \\ Z_{jM} &= \frac{1}{L^2} \sum_{k\alpha=1}^N (\Phi_j(x_{\hbar}, y_{\hbar}) \Phi_M(x_{\hbar}, y_{\hbar})), \\ \beta_{M,rs} &= \frac{1}{L^2} \int_A \cos\left(\frac{\pi r x}{L}\right) \cos\left(\frac{\pi s y}{L}\right) \Phi_M(x, y) dx dy. \end{aligned} \quad (20)$$

Equations (16), (17), (18) and (19) can be combined in matrix form:

$$\begin{bmatrix} L_{11} & 0 & L_{13} & 0 \\ 0 & L_{22} & 0 & L_{24} \\ L_{31} & L_{32} & L_{33} & L_{34} \\ 0 & L_{42} & L_{43} & L_{44} \end{bmatrix} \begin{Bmatrix} A \\ B \\ C \\ D \end{Bmatrix} = \begin{Bmatrix} F \\ 0 \\ 0 \\ 0 \end{Bmatrix} \quad (21)$$

where the coefficients L_{11}, \dots, L_{44} are given by the following equations:

$$\begin{aligned}
 L_{11} &= \bar{M}_1 (\omega_j^2 - \omega^2) \Gamma_{jM} - \hat{m}_1 \omega^2 Z_{jM}, & L_{13} &= 2\beta_{M,00}, \\
 L_{22} &= \bar{M}_2 (\Omega_j^2 - \omega^2) \Gamma_{jM} - \hat{m}_2 \omega^2 Z_{jM}, & L_{24} &= -2\beta_{M,00} e^{ikq}, \\
 L_{31} &= -i\rho c \omega \beta_{j,00}, & L_{33} &= -1, \\
 L_{34} &= -1, & L_{42} &= -i\rho c \omega \beta_{j,00}, \\
 L_{43} &= e^{-ikq}, & L_{44} &= -e^{ikq}.
 \end{aligned} \tag{22}$$

The elements of the displacement coefficient vectors A, B, C, D and the generalized force vector F take the form:

$$\begin{aligned}
 A_{j \times 1} &= \{a_1, \dots, a_7\}^T, & B_{j \times 1} &= \{T_1, \dots, T_7\}^T, \\
 C &= b_{00}, & D &= c_{00},
 \end{aligned} \tag{23}$$

$$F_{M \times 1} = 2\beta_{M,00}, \quad A = \{F_1, \dots, F_7\}^T. \tag{24}$$

Equation (22) describes the vibroacoustic behavior of the coupled system, which can be used to calculate various coefficients for constructing the displacement of each mode of the panels and the amplitudes inside the cavity. The sound transmission coefficient (τ) is expressed as:

$$\tau = \left| \frac{d_{00}}{A} \right|^2 = \left| \frac{b_{00} - c_{00} e^{2ikq}}{A} \right|^2. \tag{25}$$

The sound transmission loss for a single incident wave, therefore, is calculated in decibel scale via

$$STL = -10 \log_{10} \left(\frac{1}{\tau} \right). \tag{26}$$

3. EXPERIMENTAL INVESTIGATION

3.1. Experimental set up. The experimental set up is shown in Figure 2. The procedure and the method of converting the rectangular plate to circular plate was established in our earlier paper [13]. Briefly explained, the apparatus consists of Bruel & Kjaer type 4206 impedance tubes with the sample sandwiched inbetween. The front tube has a loudspeaker at one end to generate a plane wave in the tube. There are two sensors in the front tube to sense the incident and reflected waves. The third sensor in the back tube, terminated with an anechoic sponge, senses the transmitted wave. The signals from the three sensors are sufficient to resolve the transmitted and reflected wave amplitudes [13]. The outer of the PLA plates is 120 mm while the inner diameter for the experiment is 100 mm. The experiment samples were attached to a sample holder in the tube to provide a reliable boundary condition for each experiment.

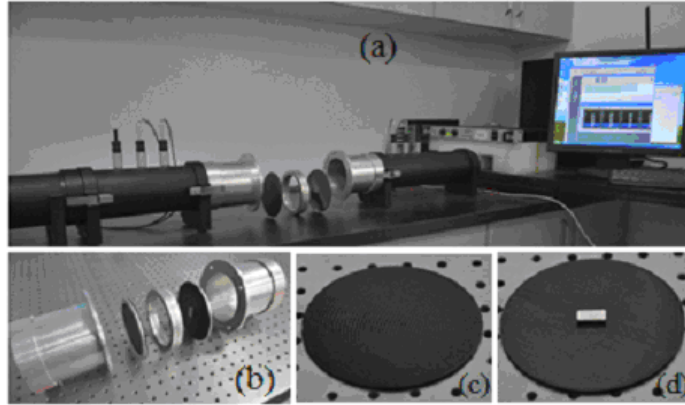


Figure 2. Experimental setup for STL measurements of fully clamped double-plates: (a) impedance tube (b) Sample holder, (c) Plain PLA, (d) Plain PLA with mass 2

3.2. Validation. Two test cases are considered in order to validate the theoretical model and numerical code developed in this study. Firstly, the present model is compared with results of Kim et al. [7] for plywood plate in Figure 3(a). The theoretical model for Kim et al. for rectangular plate was modeled using the parameters given, and the present model agree well for all frequencies. Secondly, STL predictions of the plain plate from the current model are compared with those obtained by using a commercially available FE code, COMSOL MultiphysicsTM and with experimental results using circular PLA plates. The present model, the numerical solution, and experiment data agree as shown in Figure 3(b). There is little discrepancy at the second

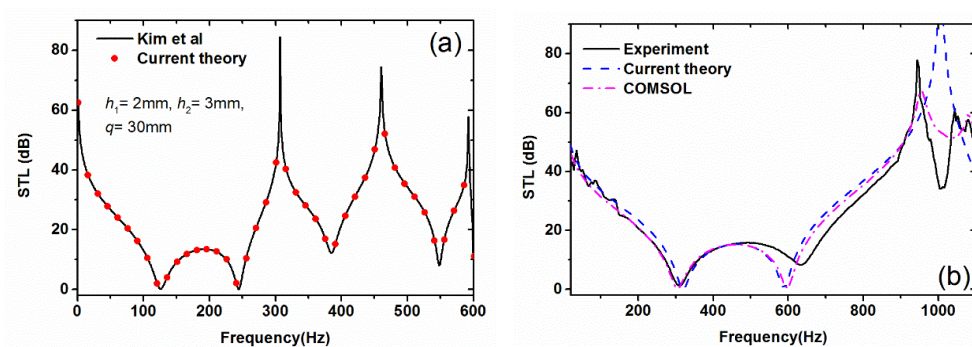


Figure 3. STL at low frequency of double PLA panel separated by air cavity without magnetic force: (a) comparison between the current study and Kim et al [7] (b) 1 mm thickness with 10 mm air cavity

resonance between the experiment and the current model. This discrepancy in the experimental values could be the result of the inability to accurately determine the air cavity gap in the experiment.

4. RESULTS AND DISCUSSION

The proposed analytical model is further applied for investigating the coupled vibroacoustic behaviour of the TAM. Consideration is paid to parameter effects such as thickness of plate, weight of the mass, cavity gap, and mode shapes of the plates on acoustic properties of the TAM. To quantify the effects of panel thickness, the STL versus frequency curve is presented in Figure 4. As expected, as the thickness increases the STL increases at low frequency. However, it is found that the frequency gap separation between the first and second resonances drops. This implies that as the thickness increases the acoustic resonance can be cancelled, even for the double plates. In addition, the current model as shown in Figure 4(b) is in close agreement with the

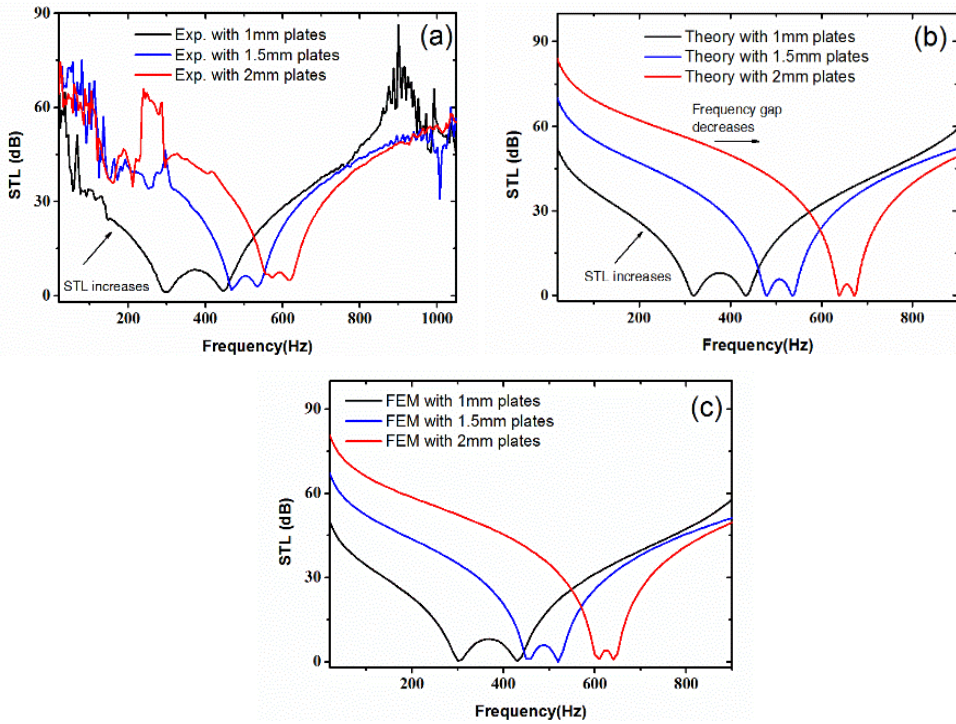


Figure 4. The effects of plate thickness on transmission loss 30 mm air cavity: (a) experimental data (b) theoretical data and (c) FEM simulations

numerical mode. For example for a 1 mm thick PLA, the numerical simulation has 300 Hz and 430 Hz for the first and second resonance, respectively, while for the current model, it has 320 Hz and 435 Hz, respectively.

Figure 5 shows the comparison of STL spectra for the effect of different masses for the experiments, current model and FEM results. Firstly, the mass shifted the plate-cavity-plate resonance from 520–300 Hz for experiment results whereas the shift is from 480–210 Hz and 480–240 Hz for the theory and FEM, respectively. It is observed that with a heavier attached mass, STL summits and valleys move toward the low frequency regime. Secondly, there is multiple modes vibration after the second resonance in the experiment results which is not captured in the theoretical and FEM results. Hence, in this frequency range the value of STL for experiments is lower compared to theory and COMSOL results. The reason for the excitation of these modes could be attributed to an unevenly damped plate, and/or to the structural flanking path as discussed by Carneal and Fuller [2]. This contributed to the lower STL values obtained in the experiment.

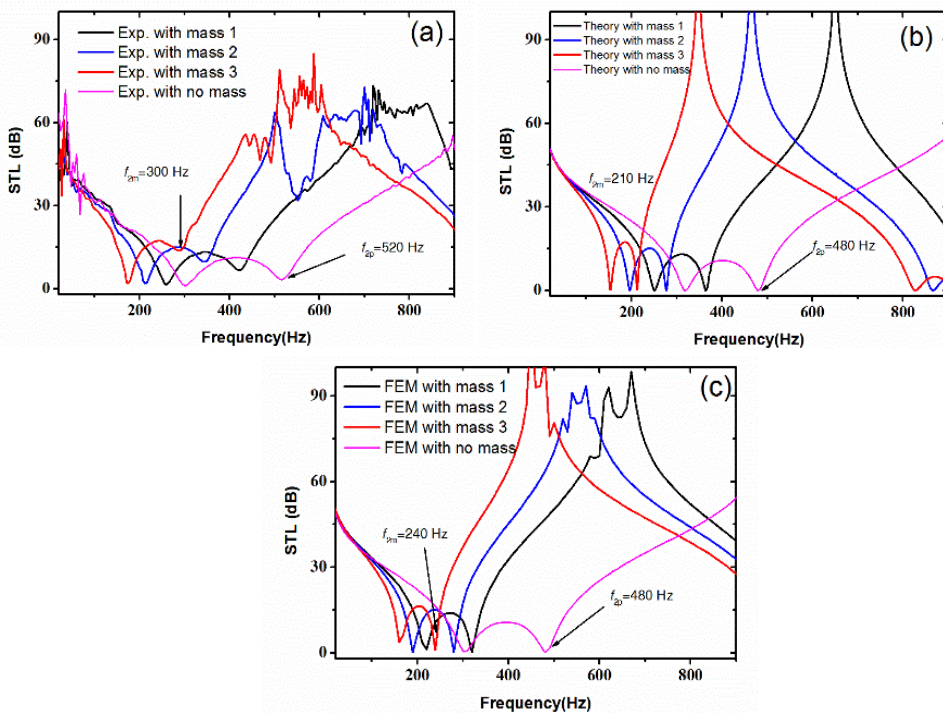


Figure 5. The effects of plate thickness on transmission loss of 30 mm air cavity as in Figure 4

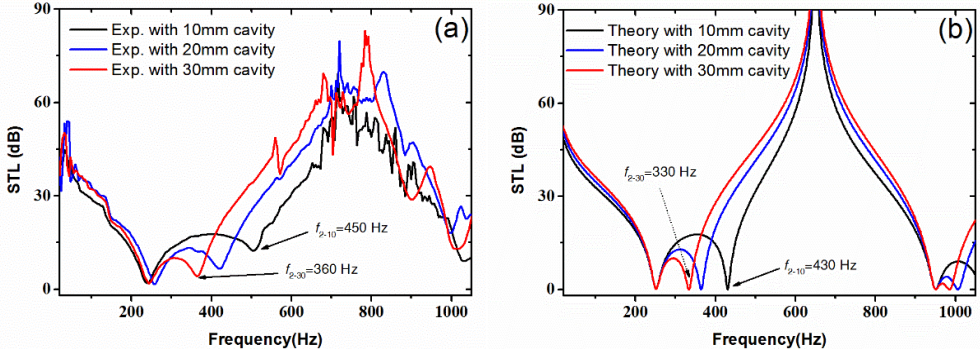


Figure 6. The effects of cavity gap on transmission loss: (a) transmission loss of 1 mm thick plate with mass 1 with different cavity gap (b) corresponding analytical solutions

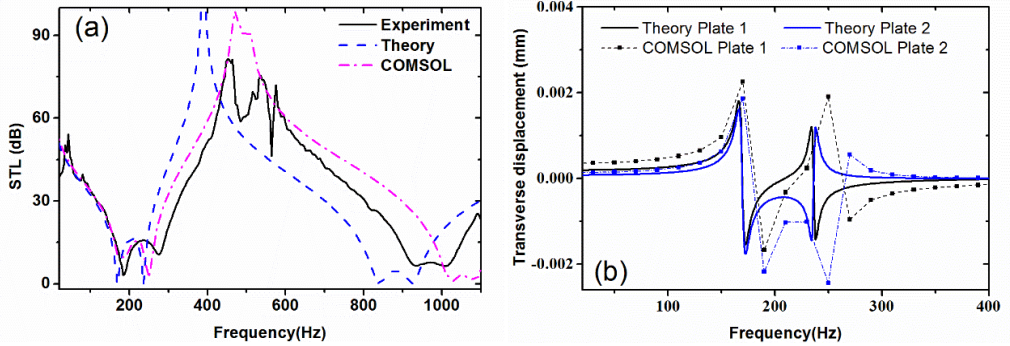


Figure 7. STL at low frequency of double PLA panel separated by air cavity with mass 2: (a) 1 mm thickness with 20 mm air cavity (b) transverse displacements for theory and FEM

The influence of the air cavity gap between the thin plates on the STL plot is displayed in Figure 6. The locations of mass-air-mass resonance shift to lower frequencies with increasing air cavity gap. The current model estimates the second resonance occurred around 430 and 330 Hz for 10 mm and 30 mm air cavity gap, respectively. The corresponding experiment occurred at 450 and 360 Hz respectively.

Figure 7 shows the STL spectra of double plates and their corresponding transverse displacement. The first two natural frequencies of the modes of TAMs obtained from the analytical method and FE analysis are $f_1^a = 170$ Hz, $f_2^a = 240$ Hz and $f_1^c = 179$ Hz and $f_2^c = 252.5$ Hz, respectively. The transverse displacement of the TAM shows that the incident panel and the radiating panel vibrate in out-of-phase between the structural and acoustic resonances. Very good agreement is observed for the first two resonant frequencies, which further confirms the accuracy and capability of the current

analytical model. The corresponding mode shapes from the analytical method and FE analysis are also shown in Figure 8. Results show that the two methods generally yield similar results. However, the effect of using a lumped mass in the derivation of the analytical mode is obviously seen in Figure 8(a), where the surface displacement area is not as wide as we have in Figure 8(b).

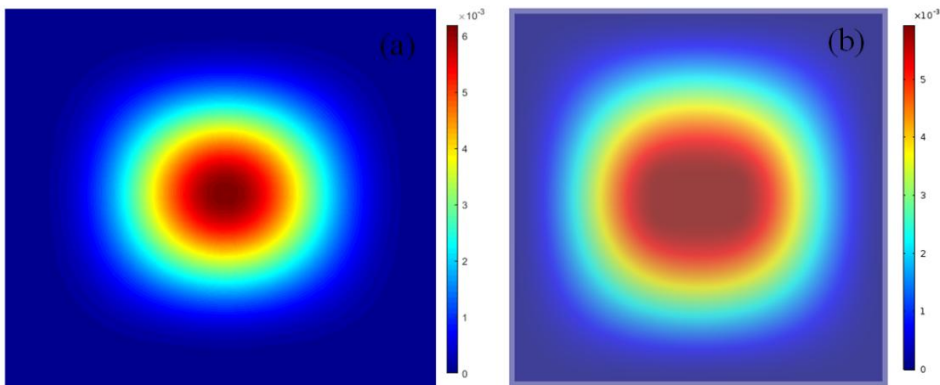


Figure 8. Panel deflection mode shapes of the TAM in Figure 6 under first resonance frequency: (a) analytical solution at $f_1^a = 170$ Hz, (b) COMSOL solution at $f_1^c = 179$ Hz

5. CONCLUSION

In this work, an analytical approach has been developed to investigate the vibroacoustic behavior of a finite double thin-plate attached with a mass in a rigid rectangular duct. Experimental measurements are subsequently performed to validate the theoretical predictions, with good overall agreement achieved for thin plates with mass and without mass. The influence of several key system parameters on the sound transmission loss capability of clamped double-thin plate panel has been systematically explored, including different mass magnitude, thickness of air cavity, and mode shapes.

REFERENCES

1. J. P. Carneal and C. R. Fuller. “Active structural acoustic control of noise transmission through double panel systems.” *AIAA Journal*, **33**, (1995), pp. 618–623. DOI: 10.2514/3.12623.
2. J. P. Carneal and C. R. Fuller. “An analytical and experimental investigation of active structural acoustic control of noise transmission through double panel systems.” *Journal of Sound Vibration*, **272**, (2004), pp. 749–771. DOI: 10.1016/S0022-460X(03)00418-8.

3. Y. Liu and C. Daudin. “Analytical modelling of sound transmission through finite clamped double-wall sandwich panels lined with poroelastic materials.” *Composite Structures*, **172**, (2017), pp. 359–373. DOI: 10.1016/j.compstruct.2017.03.024.
4. L. Cheng, Y. Y. Li, and J. X. Gao. “Energy transmission in a mechanically-linked double-wall structure coupled to an acoustic enclosure.” *The Journal of the Acoustical Society of America*, **117**, (2005), pp. 2742–2751. DOI: 10.1121/1.1886525.
5. J. Chen, Y. Chen, H. Chen, and Y. Yeh. “Bandwidth broadening for transmission loss of acoustic waves using coupled membrane-ring structure.” *Materials Research Express*, **3**, (2016), pp. 1–10. DOI: 10.1088/2053-1591/3/10/105801.
6. Y. Chen, G. Huang, X. Zhou, G. Hu, and Sun C. T. “Analytical coupled vibroacoustic modeling of membrane-type acoustic metamaterials: Membrane model.” *The Journal of the Acoustical Society of America*, **136**, (2014), pp. 2926–2934. DOI: 10.1121/1.4892870.
7. H. S. Kim, S. R. Kim, S. H. Lee, Y. H. Seo, and P. S. Ma. “Sound transmission loss of double plates with an air cavity between them in a rigid duct.” *The Journal of the Acoustical Society of America*, **139**, (2016), 2324–2333. DOI: 10.1121/1.4946987.
8. D. Young. “Vibration of rectangular plates by the Ritz method.” *Journal of Applied Mechanics*, **17**, (1950), 448–453.
9. R. D. Blevins. *Formulas for Natural Frequency and Mode Shape*. Krieger Publishing, 2001.
10. A. W. Leissa. *Vibration of Plates*. Tech. rep. NASA SP.160, Washington, 1969.
11. A. W. Leissa. “The free vibration of rectangular plates.” *Journal of Sound Vibration*, **31**, (1973), pp. 257–293. DOI: 10.1016/S0022-460X(73)80371-2.
12. A. O. Oyelade, O. M. Sadiq, and Fakinlede O. A. “Sound transmission through triple plates separated by air cavities in the low-frequency range.” *Acta Mechanica*, **230**, (2019), pp. 965–977. DOI: 10.1007/s00707-018-2318-9.
13. A. O. Oyelade, R. Yi C. Zhang, and G. Hu. “Analytical and experimental investigation on sound transmission of double thin plates with magnetic negative stiffness.” *International Journal of Applied Mechanics*, **10**, (2018), 1850054–1. DOI: 10.1142/S1758825118500540.

ANALYSIS OF STEADY STATE WEAR PROCESSES FOR INHOMOGENEOUS MATERIALS AND VARYING CONTACT LOADS

I. PÁCZELT ^a, Z. MRÓZ ^b AND A. BAKSA ^a

^aInstitute of Applied Mechanics, University of Miskolc, HUNGARY,

^bInstitute of Fundamental Technological Research, Warsaw, POLAND

istvan.paczelt@uni-miskolc.hu zmroz@ippt.pan.pl attila.baksa@uni-miskolc.hu

[Received: December 6, 2019, Accepted: June 8, 2020]

Abstract. The transient wear process on a frictional interface of two elastic bodies in relative steady sliding motion induces shape evolution of contact interface and tends to a steady state. Then wear growth develops at constant contact stress and strain distributions. In previous papers these cases were analyzed for the fixed sliding velocity between the bodies and for fixed loads [1–4]. The cases of periodic sliding under fixed normal loads were treated in [5]. The cases of periodic loads for fixed or varying sliding velocity were investigated in [6]. The variational procedure and minimization of the response functional corresponding to the wear dissipation power were applied. The modified Archard wear rule was assumed. The specific examples were solved assuming fixed values of wear parameters in the contact domain. In the present paper the previous analyses are extended to cases when the wear parameters can vary along the sliding path and similarly, the sliding velocity and normal load can vary periodically. The cases of a ring segment-on rotating disk and translating punch-on strip are considered, providing wear analysis accounting for temperature effect.

Mathematical Subject Classification: 74M10, 74M15

Keywords: contact problems, sliding wear, steady state, variational principle, optimal contact surface, p-version of finite elements

1. INTRODUCTION

In the papers Páczelt and Mróz [1, 2] a new variational principle was proposed aimed at characterization of steady wear processes. It is based on the minimum principle of wear dissipation power with the equilibrium condition of interacting bodies as a constraint. In the examples treated the wear parameters were supposed to be uniform in the contact zone. In the present paper, we shall extend the analysis by considering the wear process of inhomogeneous bodies.

A class of problems will be considered when the wear parameters are not fixed but can vary with point position in the contact zone. Also elastic moduli are allowed to vary with point position in the body domain. Such assumptions provide a more realistic approach when a surface treatment is applied to improve hardness and wear resistance of contact layers. A general theoretical framework is first developed and next the numerical wear analysis is presented for two specific problems, namely a ring brake and translating punch on a plane substrate. It is demonstrated that the varying

wear parameters affect essentially the contact pressure distribution and the wear rate in the steady state.

The wear rule specifies the wear rate $\dot{w}_{i,n}$ of the i^{th} body in the normal contact direction. Following the previous work [1, 2] the modified Archard wear law is

$$\dot{w}_{i,n} = \beta_i(\tau_n)^{b_i} \|\dot{\mathbf{u}}_\tau\|^{a_i} = \beta_i(\mu p_n)^{b_i} \|\dot{\mathbf{u}}_\tau\|^{a_i} = \beta_i(\mu p_n)^{b_i} v_r^{a_i} = \tilde{\beta}_i p_n^{b_i} v_r^{a_i}, \quad i = 1, 2 \quad (1.1)$$

where β_i , a_i and b_i are the wear parameters, μ is the friction coefficient, the relative tangential velocity is $\dot{\mathbf{u}}_\tau$, $\tilde{\beta}_i = \beta_i \mu^{b_i}$, $v_r = \|\dot{\mathbf{u}}_\tau\|$. The shear stress at the contact surface is denoted by τ_n and related to the contact pressure p_n by the Coulomb friction law $\tau_n = \mu p_n$. The unilateral contact occurs on the boundary portion S_c . In [1, 2] the wear rate vector was introduced, which is not only normal to the contact surface but also has tangential component. The elastic rates in the normal and tangential directions are denoted by $\dot{\mathbf{u}}_{e,n}^{(\alpha)}$ and $\dot{\mathbf{u}}_{e,\tau}^{(\alpha)}$, respectively. The rigid body rates are denoted by $\dot{\mathbf{u}}_{R,n}^{(\alpha)}$, $\dot{\mathbf{u}}_{R,\tau}^{(\alpha)}$. The relative tangential velocity has the elastic and rigid body portions

$$\dot{\mathbf{u}}_\tau = \dot{\mathbf{u}}_{e,\tau}^{(2)} + \dot{\mathbf{u}}_{R,\tau}^{(2)} - (\dot{\mathbf{u}}_{e,\tau}^{(1)} + \dot{\mathbf{u}}_{R,\tau}^{(1)}) = \dot{\mathbf{u}}_{e,\tau} + \dot{\mathbf{u}}_{R,\tau}, \quad \|\dot{\mathbf{u}}_\tau\| = v_r. \quad (1.2)$$

Rigid body velocity has two components:

1. The *sliding velocity* is prescribed by stated boundary conditions allowing for a rigid body motion and elastic displacements developed in a stressed state.
2. The *wear velocity* is defined by the the rigid body motion induced by wear, so that

$$\begin{aligned} \dot{\mathbf{u}}_{R,n}^{(w)} &= (\dot{\boldsymbol{\lambda}}_F + \dot{\boldsymbol{\lambda}}_M \times \Delta \mathbf{r}) \cdot \mathbf{n}_c, \\ \dot{\mathbf{u}}_{R,\tau}^{(w)} &= (\dot{\boldsymbol{\lambda}}_F + \dot{\boldsymbol{\lambda}}_M \times \Delta \mathbf{r}) - \dot{u}_{R,n} \mathbf{n}_c, \end{aligned} \quad (1.3)$$

where $\dot{\boldsymbol{\lambda}}_F$ and $\dot{\boldsymbol{\lambda}}_M$ are the relative translation and rotation velocities induced by wear, which should be determined from the contact problem solution, $\Delta \mathbf{r}$ is the position vector with respect to a reference point.

Assume now that the body B_1 plays the role of an indenter and its rigid body motion is associated with the wear process. The body B_2 executes the sliding motion on the contact surface.

The contact stress of interaction of bodies B_1 and B_2 is

$$\mathbf{t}^c = \mathbf{t}_1^c = -\mathbf{t}_2^c = -p_n(\mathbf{n}_c \pm \mu \mathbf{e}_{\tau 1}) - \mu_d p_n \mathbf{e}_{\tau 2} = -p_n \tilde{\mathbf{n}}_c, \quad (1.4)$$

where μ is the friction coefficient specifying the shear stress in sliding direction and μ_d is the friction coefficient associated with transverse wear velocity.

In the wear process the friction between two bodies depends not only on asperity interaction generating shear stress nearly oriented along the relative sliding velocity, but also on the direction of motion of the debris particle layer formed in the contact zone. In direction of the relative sliding velocity the friction coefficient is usually larger than in the transverse direction. In [2] three types of tangential wear dissipation models were introduced and discussed, one accounting only for wear particle slip and the other for the wear debris particle rotation and slip within the contact zone. The proper selection of the transverse friction model should be based on micromechanical

analysis and validation tests. The other reason for non-coaxial slip and friction force action is related to the anisotropic friction condition discussed in detail in Reference [7].

The vectors $\mathbf{e}_{\tau 1}, \mathbf{e}_{\tau 2}$ and \mathbf{n}_c provide the local reference triad. Here \mathbf{n}_c is the unit normal to the contact surface of body B_1 , $\mathbf{e}_{\tau 1}$ is the tangent unit vector coaxial with the sliding velocity and $\mathbf{e}_{\tau 2}$ is the transverse tangent unit vector. The sign + corresponds to the case when the relative velocity $\dot{\mathbf{u}}_\tau = \dot{\mathbf{u}}_\tau^{(2)} - \dot{\mathbf{u}}_\tau^{(1)} = -\|\dot{\mathbf{u}}_\tau\|\mathbf{e}_{\tau 1} = -v_\tau \mathbf{e}_{\tau 1}$ is with the corresponding shear stress acting on the body B_1 along $-\mathbf{e}_{\tau 1}$.

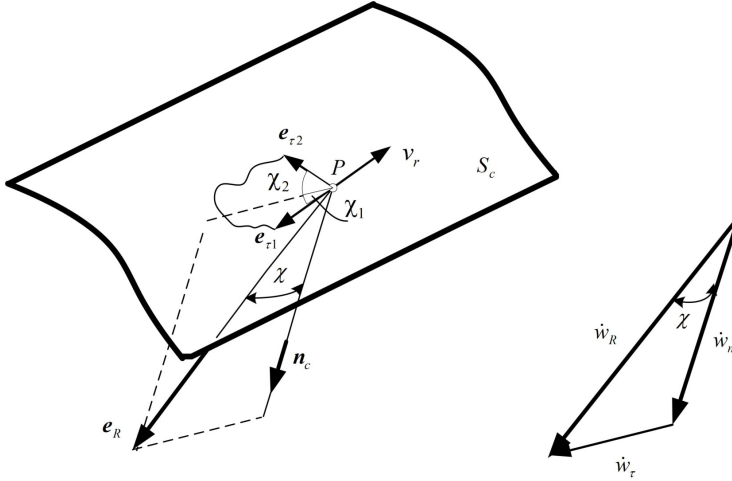


Figure 1. Wear rate vectors, local coordinate system

The wear rate vector for body B_i $i = 1, 2$ (see Figure 1) is

$$\dot{\mathbf{w}}_i = (-1)^i (\dot{w}_{i,n} \mathbf{n}_c - \dot{w}_{i,\tau 1} \mathbf{e}_{\tau 1} - \dot{w}_{i,\tau 2} \mathbf{e}_{\tau 2}), \quad (1.5)$$

where the tangential wear components can be regarded as the initial velocities for the wear debris transport in the contact layer.

A fundamental assumption was introduced, namely, at the steady state the wear rate vector is collinear with the rigid body wear velocity of B_1 , so that

$$\mathbf{e}_R = \frac{\dot{\lambda}_F + \dot{\lambda}_M \times \Delta \mathbf{r}}{\|\dot{\lambda}_F + \dot{\lambda}_M \times \Delta \mathbf{r}\|} \quad (1.6)$$

and

$$\begin{aligned} \dot{\mathbf{w}} &= \dot{\mathbf{w}}_2 - \dot{\mathbf{w}}_1 = \dot{\mathbf{w}}_R = \dot{w}_{2,R} \mathbf{e}_R - \dot{w}_{1,R} \mathbf{e}_R, \\ \dot{w}_{1,R} &= -\dot{w}_{1,R} \mathbf{e}_R, \dot{w}_{2,R} = \dot{w}_{2,R} \mathbf{e}_R. \end{aligned} \quad (1.7)$$

It has been shown [1, 2] that the steady state conditions can be obtained from minimization of the generalized wear dissipation power for the case of wear of two bodies

$$D_w^{(q)} = \sum_{i=1}^2 \left(\int_{S_c} (\mathbf{t}_i^c \cdot \mathbf{w}_i)^q dS \right)^{1/q} = \sum_{i=1}^2 C_i^{1/q}, \quad (1.8)$$

where q is the control parameter, usually $q \geq 0$.

Assume that the contact pressure $p_n(\mathbf{x})$ and the friction shear stress satisfy the global equilibrium conditions for the body B_1 , so we have

$$\begin{aligned}\mathbf{f} &= - \int_{S_c} \tilde{\mathbf{n}}_c p_n \, dS + \mathbf{f}_0 = \mathbf{0}, \\ \mathbf{m} &= - \int_{S_c} \Delta \mathbf{r} \times \tilde{\mathbf{n}}_c p_n \, dS + \mathbf{m}_0 = \mathbf{0},\end{aligned}\tag{1.9}$$

where \mathbf{f}_0 and \mathbf{m}_0 denote the resultant force and moment acting on the body B_1 , $\Delta \mathbf{r}$ is the position vector.

Introducing the Lagrange multipliers $\dot{\lambda}_F$ and $\dot{\lambda}_M$, the equilibrium conditions in (1.9), we can state the Lagrangian functional

$$L_{D_w}^{(q)} = L_{D_w}^{(q)}(p_n, \dot{\lambda}_F, \dot{\lambda}_M) = D_w^{(q)}(p_n) + (b+1)\dot{\lambda}_F \cdot \mathbf{f} + (b+1)\dot{\lambda}_M \cdot \mathbf{m},\tag{1.10}$$

where it is assumed that $b = b_1 = b_2$ [3].

Satisfying the stationary condition of (1.10), $\delta_{p_n} L_{D_w}^{(q)} = 0$, the contact pressure distribution is obtained in the form

$$p_n = \left(\frac{\dot{\lambda}_F \cdot \tilde{\mathbf{n}}_c + (\dot{\lambda}_M \times \Delta \mathbf{r}) \cdot \tilde{\mathbf{n}}_c}{\left(\tilde{\beta}_1 v_r^{a_1}\right)^q C_1^{\frac{1-q}{q}} + \left(\tilde{\beta}_2 v_r^{a_2}\right)^q C_2^{\frac{1-q}{q}}} (1 \mp \mu \tan \chi)^{-q} \right)^{\frac{1}{(b+1)q-1}}\tag{1.11}$$

and the equilibrium equations are

$$\begin{aligned}\mathbf{f}(\dot{\lambda}_F, \dot{\lambda}_M) &= - \int_{S_c} \tilde{\mathbf{n}}_c p_n \, dS + \mathbf{f}_0 = \mathbf{0}, \\ \mathbf{m}(\dot{\lambda}_F, \dot{\lambda}_M) &= - \int_{S_c} \Delta \mathbf{r} \times \tilde{\mathbf{n}}_c p_n \, dS + \mathbf{m}_0 = \mathbf{0}.\end{aligned}\tag{1.12}$$

Let us note that the orientation angle $\chi = \chi(\dot{\lambda}_F, \dot{\lambda}_M)$ depends on the Lagrange multiplier vectors and equations (1.12) are highly nonlinear. The Lagrange multiplier vectors $\dot{\lambda}_F, \dot{\lambda}_M$ can be calculated by applying the Newton-Raphson technique, as these variables are internal unknowns.

The control parameter q provides the transition from local to global response. In fact, for $q = 1$, these functionals provide the global measures but for $q \rightarrow \infty$ they represent local values of integrands. It has been shown that for $q = 1$, the optimal solution corresponds to steady state condition. Thus, this condition can be specified directly from (1.11) and (1.12) instead of integration of the wear rule (1.1) for the whole transient wear process until the steady state is reached. We shall first illustrate the applicability of the stationary conditions to the analysis of several specific examples.

In the work of Goryacheva [8] we find some examples for cases when the wear parameters are not uniform along the contact surface. Such a situation occurs for inhomogeneous bodies. In [8] (Chapter 7), a case was analyzed when one of the bodies

executes a rigid body translation displacement. The problem was solved analytically for special boundary conditions (contact surface of periodical character). We would like to analyze similar cases, when there is rigid body rotation and the contact surface is not only a plane. The heat generation in the contact zone is accounted for and the effect of temperature field on the steady wear state is analyzed. It is assumed that strains are small and the materials of the contacting bodies are linearly elastic. Our solution has been obtained by using the p -version finite element method [9, 10].

2. WEAR ANALYSIS IN RING SEGMENT-ON-ROTATING DISK TESTS

Consider first the interaction of stationary ring shoes with rotating disk of thickness t_{th} and radius R_0 (Figure 2). Assume the plane stress state within the rings and disk.

The shoes are loaded uniformly by the pressure \tilde{p} on the upper/lower boundary with the resulting force F_0 and may translate along the z -axis in order to arrange the interaction with disk at the contact surfaces specified by the angles $\pm\alpha_0$. The formulation will be for the upper shoe. In this case the rigid body wear velocity equals $\dot{\lambda}_F = -\dot{\lambda}_F \mathbf{e}_z$. The disk is rotated with the angular velocity ω in the clockwise or anticlockwise direction.

Following our main assumption (1.6), the wear rate vector is collinear with \mathbf{e}_z , thus

$$\begin{aligned} \mathbf{e}_R &= -\mathbf{e}_z, & \chi &= \alpha, \\ \mathbf{n}_c &= -\cos \alpha \mathbf{e}_z - \sin \alpha \mathbf{e}_x, & \mathbf{e} = \mathbf{e}_{\tau 1} &= \sin \alpha \mathbf{e}_z - \cos \alpha \mathbf{e}_x, & \mathbf{e}_{\tau 2} &= \mathbf{e}_y, \\ \tilde{\mathbf{n}}_c &= \mathbf{n}_c \pm \mu \mathbf{e}_\tau, \end{aligned} \quad (2.1)$$

where the lower sign ($-$) corresponds to the case of disk rotation in the anticlockwise direction and the upper sign ($+$) to the rotation in the opposite direction. The contact pressure distribution resulting from the stationary condition (1.11) is expressed as follows:

$$p_n = \left(\frac{\dot{\lambda}_F}{\sum_{i=1}^2 \left(\tilde{\beta}_i v_r^{a_i} \right)^q C_i^{\frac{1-q}{q}}} \right)^{\frac{1}{(b+1)q-1}} (\cos \alpha \mp \mu \sin \alpha)^{\frac{1-q}{(b+1)q-1}} (\cos \alpha)^{\frac{q}{(b+1)q-1}}. \quad (2.2)$$

The equilibrium condition of the shoe is

$$- \int_{-\alpha_0}^{\alpha_0} p_n (\mathbf{n}_c \pm \mu \mathbf{e}_\tau) \cdot \mathbf{e}_z R_0 t_{th} d\alpha = F_0 \quad (2.3)$$

and provides the expression for the loading force

$$F_0 = \int_{-\alpha_0}^{\alpha_0} \left(\frac{\dot{\lambda}_F}{\sum_{i=1}^2 \left(\tilde{\beta}_i v_r^{a_i} \right)^q C_i^{\frac{1-q}{q}}} \right)^{\frac{1}{(b+1)q-1}} (\cos \alpha \mp \mu \sin \alpha)^{\frac{1-q}{(b+1)q-1}+1} (\cos \alpha)^{\frac{q}{(b+1)q-1}} R_0 t_{th} d\alpha. \quad (2.4)$$

The wear rate component in the normal direction to the contact surface equals

$$\dot{w}_n = \left(\tilde{\beta}_1 (R_0 \omega)^{a_1} \right) \left(\frac{F_0}{\tilde{I}_{D_w}^{\mp(q=1)}} \right)^b \frac{\cos \alpha}{\tilde{\beta}_1 (R_0 \omega)^{a_1}} \neq const \quad (2.8)$$

and the wear rate along the vertical z -axis

$$\dot{w} = \dot{w}_R = \dot{\lambda}_F = \frac{\dot{w}_n}{\cos \alpha} = \left(\frac{F_0}{\tilde{I}_{D_w}^{\mp(q=1)}} \right)^b = const \quad (2.9)$$

is constant. The wear volume rate now equals

$$\dot{W} = \int_{-\alpha_0}^{\alpha_0} \dot{w}_n R_0 t_{th} d\alpha = \int_{-\alpha_0}^{\alpha_0} \dot{w}_v \cos \alpha R_0 t_{th} d\alpha = \left(\frac{F_0}{\tilde{I}_{D_w}^{\mp(q=1)}} \right)^b R_0 t_{th} 2 \sin \alpha_0. \quad (2.10)$$

Case B: At the end, we finalize our results for $q = 1$ at $\tilde{\beta}_i = \beta_i \mu^b$ and $v_r = \|\dot{\mathbf{u}}_\tau\|$. Then using (2.2) and (2.3) we have

$$F_0 = \int_{-\alpha_0}^{\alpha_0} \left(\frac{\dot{\lambda}_F}{\sum_{i=1}^2 \left(\tilde{\beta}_i v_r^{a_i} \right)} \right)^{\frac{1}{b}} (\cos \alpha \mp \mu \sin \alpha) (\cos \alpha)^{\frac{1}{b}} R_0 t_{th} d\alpha \quad (2.11)$$

and after introducing the integral

$$\tilde{I}_{D_w}^{\mp(q=1)} = \int_{-\alpha_0}^{\alpha_0} \left(\frac{1}{\sum_{i=1}^2 \left(\tilde{\beta}_i v_r^{a_i} \right)} \right)^{\frac{1}{b}} (\cos \alpha \mp \mu \sin \alpha) (\cos \alpha)^{\frac{1}{b}} R_0 t_{th} d\alpha \quad (2.12)$$

we obtain

$$\frac{F_0}{\tilde{I}_{D_w}^{\mp(q=1)}} = \left(\dot{\lambda}_F \right)^{\frac{1}{b}} \quad (2.13)$$

so the contact pressure is expressed as follows:

$$p_n = \frac{F_0}{\tilde{I}_{D_w}^{\mp(q=1)}} \left(\frac{\cos \alpha}{\sum_{i=1}^2 \left(\tilde{\beta}_i v_r^{a_i} \right)} \right)^{\frac{1}{b}}, \quad v_r = R_0 \omega. \quad (2.14)$$

The wear rate component in the contact normal direction equals

$$\dot{w}_n = \sum_{i=1}^2 \left(\tilde{\beta}_i v_r^{a_i} \right) \left(\frac{F_0}{\tilde{I}_{D_w}^{\mp(q=1)}} \right)^b \frac{\cos \alpha}{\sum_{i=1}^2 \left(\tilde{\beta}_i v_r^{a_i} \right)} \neq const \quad (2.15)$$

and the wear rate along the z -axis according to (2.9) is constant

$$\dot{w}_R = \left(\frac{F_0}{\tilde{I}_{D_w}^{+(q=1)}} \right)^b = \text{const.} \quad (2.16)$$

The wear volume rate now equals

$$\dot{W} = \int_{-\alpha_0}^{\alpha_0} \dot{w}_n R_0 t_{\text{th}} d\alpha = \int_{-\alpha_0}^{\alpha_0} \dot{w}_v \cos \alpha R_0 t_{\text{th}} d\alpha = \left(\frac{F_0}{\tilde{I}_{D_w}^{+(q=1)}} \right)^b R_0 t_{\text{th}} 2 \sin \alpha_0. \quad (2.17)$$

Example 1

Select the following specific parameter values: loading force $F_0 = 10$ kN, contact angle $\alpha_0 = \pm 30^\circ$, disk radius $R_0 = 200$ mm, and thickness $t_{\text{th}} = 10$ mm. The wear parameters are $\beta_1 = 0.0002$, $\beta_2 = 0$, $a = b = 1$, the friction coefficient is $\mu = 0.25$, the angular disk velocity $\omega = 2.5$ rad/s, $\tilde{\beta}_1 = \beta_1 \mu$, $\tilde{c} = \tilde{\beta}_1 (R_0 \omega) = \tilde{\beta}_1 v_r$, $\tilde{\beta}_2 v_r = 0$. The wear coefficient is equal to $\tilde{c} = c1 = 0.025$ in the intervals $-\alpha_0 \leq \alpha \leq -15$, $15 \leq \alpha \leq \alpha_0$ and in the middle zone $\tilde{c} = c1/2$. The wear resistance in the middle zone is greater than in the exterior zones.

Minimizing the wear dissipation power $D_w^{(q)}(p_n)$, the contact pressure is specified by (2.6). Figures 3 presents the pressure distribution for anticlockwise and clockwise disk rotation. The pressure distribution depends on the orientation of disk rotation. If q is close to 0.5 the contact pressure and wear distribution are highly localized at the contact zone perimeter or at the centre line.

Figures 4 presents the associated wear distribution for different values of q , the steady state wear process occurs for which $\dot{w}_v = \dot{w}_R = \text{const}$ and the pressure distribution is specified by (2.7). The steady state pressure distribution is symmetric with respect to the z -axis and does not depend on the friction coefficient.

Example 2

Consider now the loading shoe in the form of a thin ring segment of constant thickness $t_{\text{th}} = 10$ mm, subjected to the distributed load localized at the centre, so that the vertical traction is $\tilde{p} = 49.5$ MPa and the resultant force $F_0 = 10$ kN. Figure 5 presents the finite element mesh of the system and the initial contact pressure distribution with no gap (clockwise rotation). In the vertical direction there are 4 layers, along the long direction there are 11 elements. In the disk radial direction there are 4 elements, in the circumferential direction there are $15 + 11 + 15 = 41$ elements. For solution of the contact problem [11] the p -version finite element method [9] was used. The initial contact pressure distribution is highly localized near the centre line and due to friction on the right side boundary, (see Figure 5b).

The steady state of wear is reached when the contact pressure distribution specified by (2.7) for $q = 1$ is satisfied.

We would like consider the thermo-mechanical problem with angular velocity $\omega = 5$ rad/s. The friction heat is generated in the contact surface $S_c \in (r = 200$ mm, $\alpha_0 = \mp 30^\circ)$. Friction coefficient is $\mu = 0.25$. In the surface shoe $S_q \in (r = 200$ mm, $x = \mp 100$ mm), in the surface of the disc $S_q \in (r = 200$ mm) the heat convection

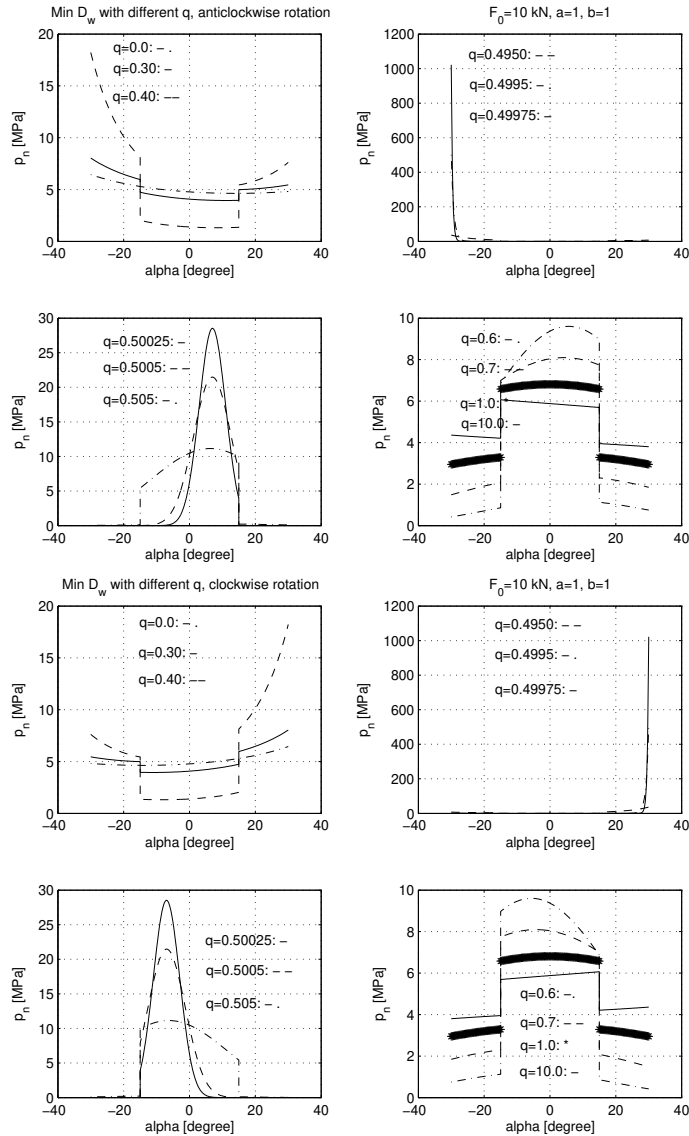


Figure 3. Contact pressure distribution for anticlockwise (rows 1,2), and clockwise (rows 3,4) disk rotation for different values of the control parameter q

condition is assumed, and in the surface $S_\theta \in (r = 50 \text{ mm})$ zero temperature is prescribed. The heat convection condition is also supposed in the whole plane surface. In view of anti-symmetry of the thermo-mechanical problem (we have two shoes)

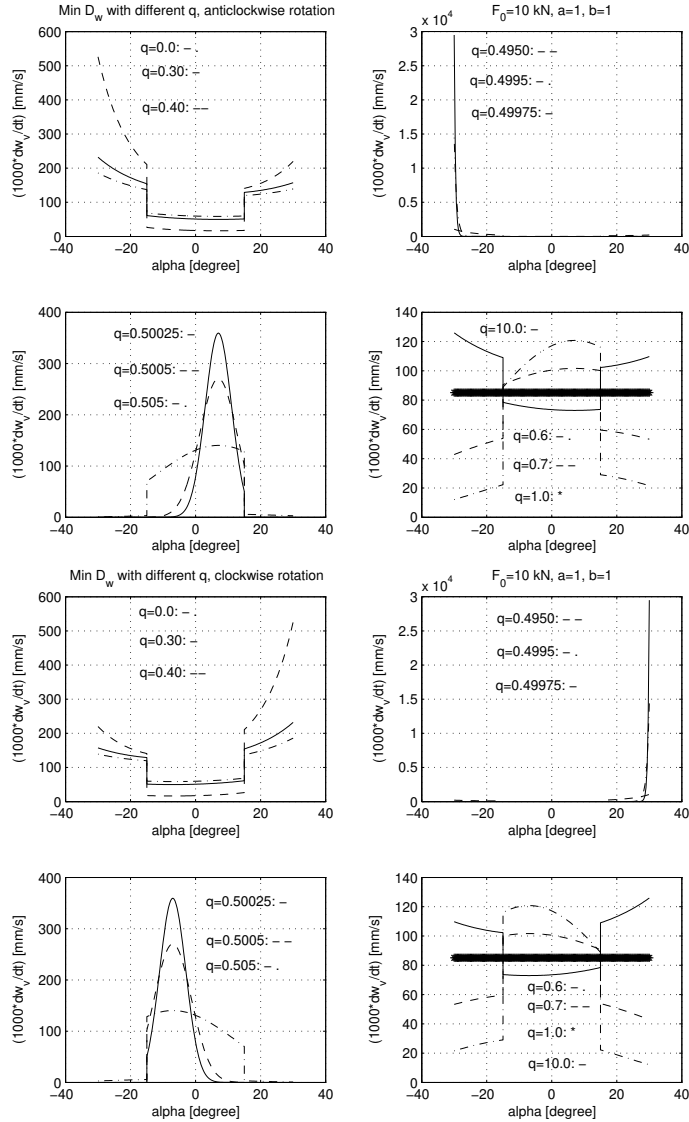


Figure 4. Vertical wear rate distribution for anticlockwise (rows 1,2), and clockwise (rows 3,4) disk rotations for different values of q

the thermo field must satisfy $\theta(x, z) = \theta(-x, -z)$ condition, that is in the axis x is $\theta(x) = \theta(-x)$, and for displacement field is $\mathbf{u}(x) = \mathbf{u}(-x)$.

We shall analyze different shoe (Body 1) variants.

1. Material homogeneity for whole body 1, and wear parameters are uniform.

2. Material homogeneity for whole body 1 and wear parameters are not uniform (see Example 1).
3. The shoe is made from different materials. In the finite element layer 1-2 in the interval material $-\alpha_0 \leq \alpha \leq -15$, $15 \leq \alpha \leq \alpha_0$ is steel, in the middle part material is a composite (see Figure 5c). The composite segment is in the region: $-\alpha^- \leq \alpha \leq \alpha^+$, $R_0 \leq r \leq R_0 + h_a$. Material parameters are given in Table 1. The remaining parts of the shoe and disk are made of steel. For the distribution of wear parameters, see Example 1.

Table 1. Mechanical and thermal parameters of the two materials.

	$K^{(i)}$ [W/mK]	h_c [W/m ² K]	$c^{(i)}$ [J/kgK]	$\alpha_\theta \cdot 10^5$ [1/K]	$E \cdot 10^{-5}$ [MPa]	$\nu^{(i)}$	$\rho^{(i)}$ [kg/m ³]
Mat. 1 steel	55	80	460	1	2	0.3	7800
Mat. 2 composite	5	80	1200	3	1.3	0.25	846

In the case of 1 and 2 calculations the material used was homogeneous (steel), but wear parameters in variant 2 were not uniform.

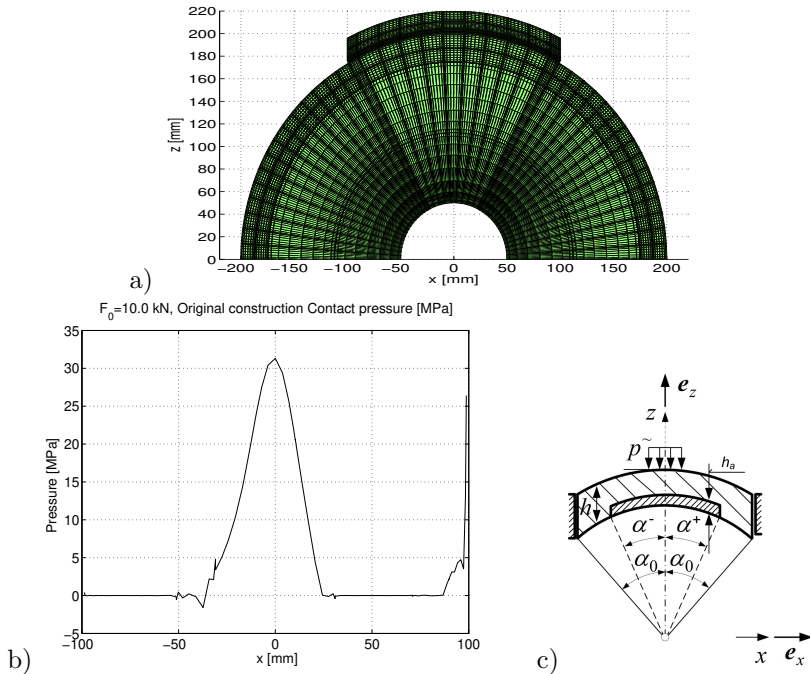


Figure 5. a) Finite element mesh for ring-disk system, b) initial contact pressure distribution (clockwise rotation), c) shoe geometry for Variant 3

Using the p -version of the finite element technique for the solution of contact shape optimization problem (cf. Páczelt [11], Páczelt and Baksa [12], Páczelt and Mróz [1]), the stationary pressure distribution is reached for a small gap introduced with respect to the initial contact shape. The thermal problem is solved by using the upwinding Petrov-Galerkin formulation [2]. Using this technique the finite element solution does not exhibit oscillation. The weak variational formulation of mechanical and thermal problem can induce niggling oscillations, see [2, 4]. The finite element problems were solved by the p -version finite element technique using polynomial order $p = 8$.

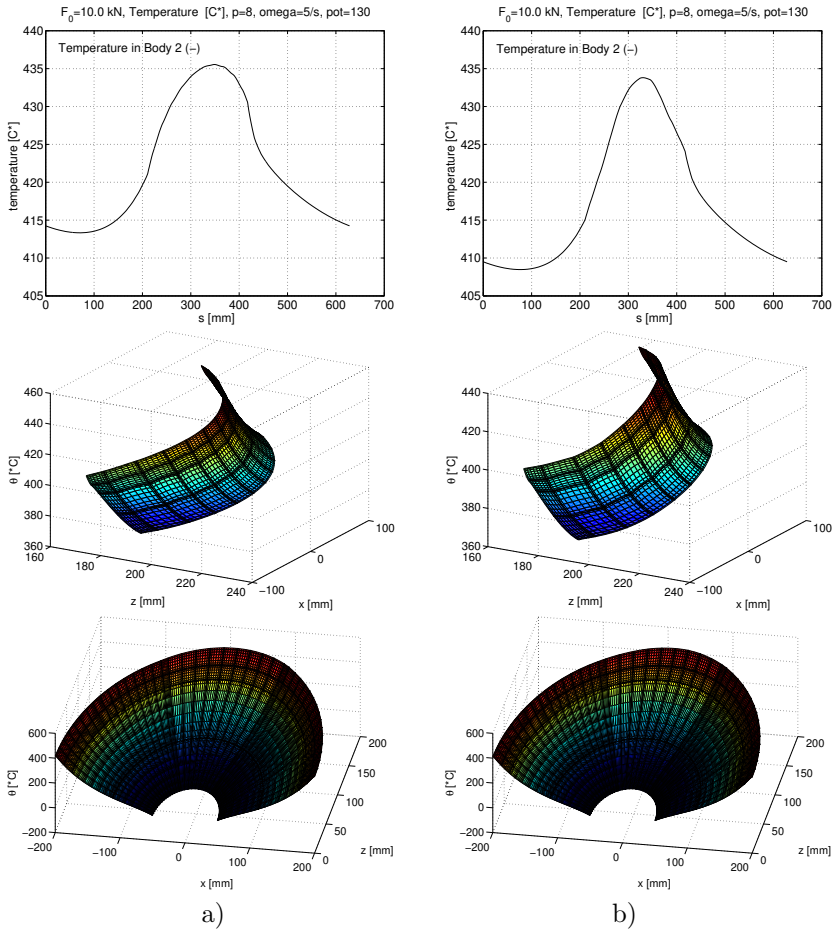


Figure 6. Temperature distribution in Body 2 along the radius ($r = R_0 = 200$ mm) (top row), temperature field in the punch (middle row), temperature field in the disk for clockwise rotation at angular velocity $\omega = 5$ rad/s (bottom row) for a) Variant 1 $\tilde{\beta} = const.$, b) Variant 2 $\tilde{\beta} \neq const.$

In Figure 6 the diagrams for Variants 1 and 2 can be seen. From top to bottom there are figures for temperature distribution on the disc boundary ($r = R_0 = 200$ mm),

inside the shoe, and inside the disc. Note that in Variant 2, the pressure is higher ($p_{n,max} = 6.887$ MPa) in the middle of the contact domain than in Variant 1 ($p_{n,max} = 5.286$ MPa), where the line has a little pick form. Also we can see that at the boundary point ($r = 200$ mm, $x = 100$ mm) the temperature is higher than at the leading edge point ($r = 200$ mm, $x = -100$ mm).

The total gap (shape) function is marked by the continuous line in Figure 7. The temperature distribution is marked by +, the gap without temperature effect is marked by o. The curves (-) and (o) indicate that the effect of temperature distribution is significant. Heat flux distribution for Variant 1 and 2 is shown in Figure 8. The difference between the two curves is very small.

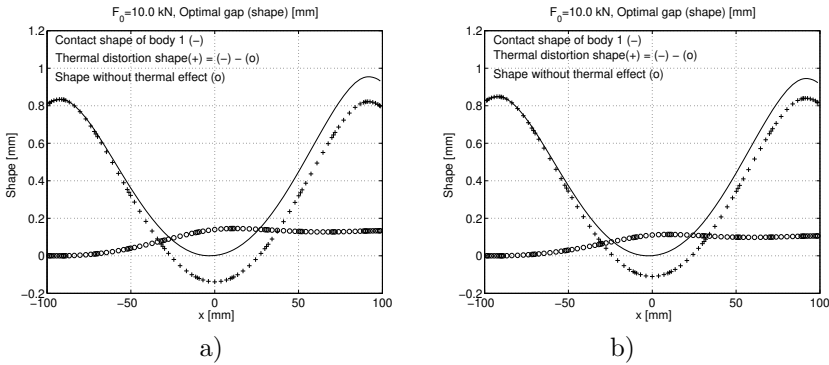


Figure 7. Shape at steady wear state: a) Variant 1, b) Variant 2

Variant 3. Temperature distribution is shown in Figure 9. The optimal normal gap (Figure 9b) differs from gaps of Variant 2 (see Figure 7b). The elastic Young moduli are different in the central regions.

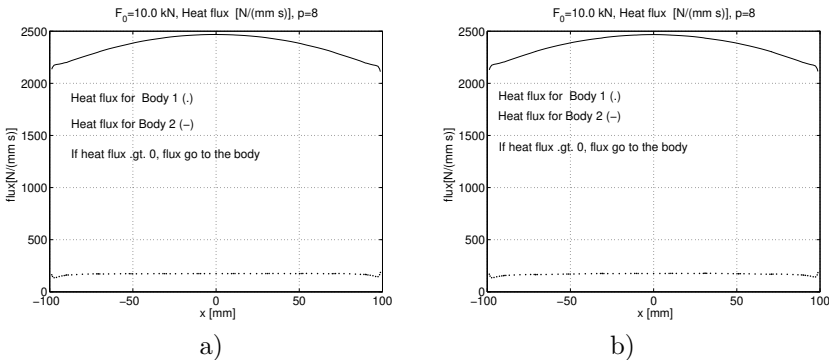


Figure 8. Heat fluxes: (a) Variant 1, (b) Variant 2

It is seen in Figure 9c that temperature is well isolated in the two layers, as in the central part of the region $x = 0$, $205 \leq z \leq 220$ the temperature is $\sim 350^\circ\text{C}$,

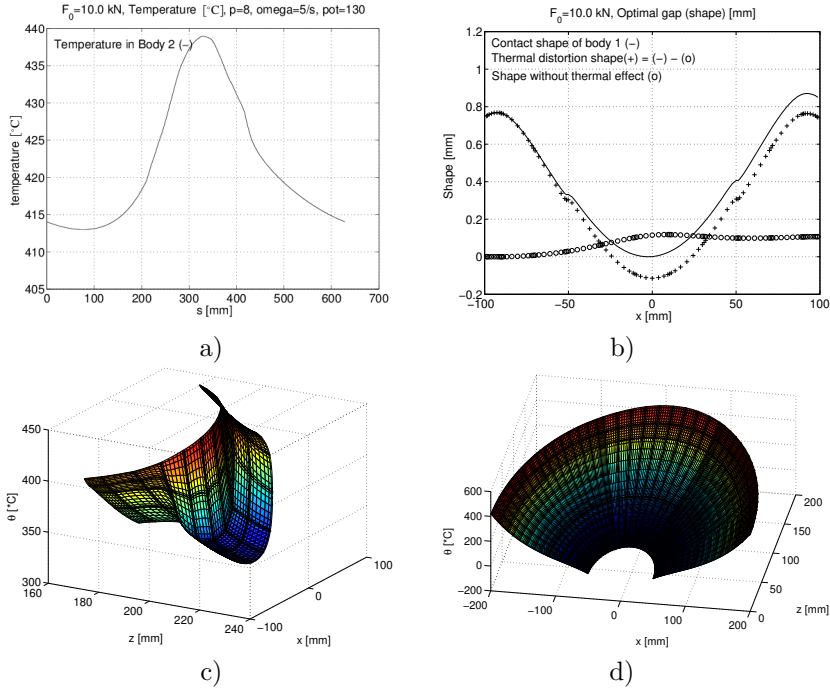


Figure 9. a) Temperature distribution in the Body 2 along the radius ($r = R_0 = 200$ mm), b) contact shape in the steady wear state, c) temperature field in the shoe, d) temperature field in the disk for clockwise rotation at angular velocity $\omega = 5$ rad/s. Material of the shoe is inhomogeneous, problem: Variant 3

which approximately is lower by $\sim 90^\circ\text{C}$ from the maximum $\sim 440^\circ\text{C}$. The numerical analysis demonstrates that high temperature is also within the disc. In the steady state along the outer radius ($r = R_0 = 200$ mm), the temperature varies by $\sim 25^\circ\text{C}$ in one rotation cycle.

One interesting point here is the heat flux partition between the shoe and the disc (see Figure 10). Because the disc rotates and its surface is larger than that of shoe, much heat is transferred from its body to the environment. As the conductivity coefficient is approximately 11 times smaller for material 2, in the center contact domain the heat flux is more oriented to the disc than to the shoe. The heat transfer ratio function has discontinuity in the interface of different materials.

3. BLOCK UNDERGOING RIGID BODY TRANSLATION AND ROTATION

Referring to Figure 11, consider a block (or punch) B_1 resting on a plane substrate B_2 . It is loaded by the force F_0 , also allowed to rotate around the pin O and translate relative to the substrate along the direction \tilde{e}_x normal to the contact plane S_c . The

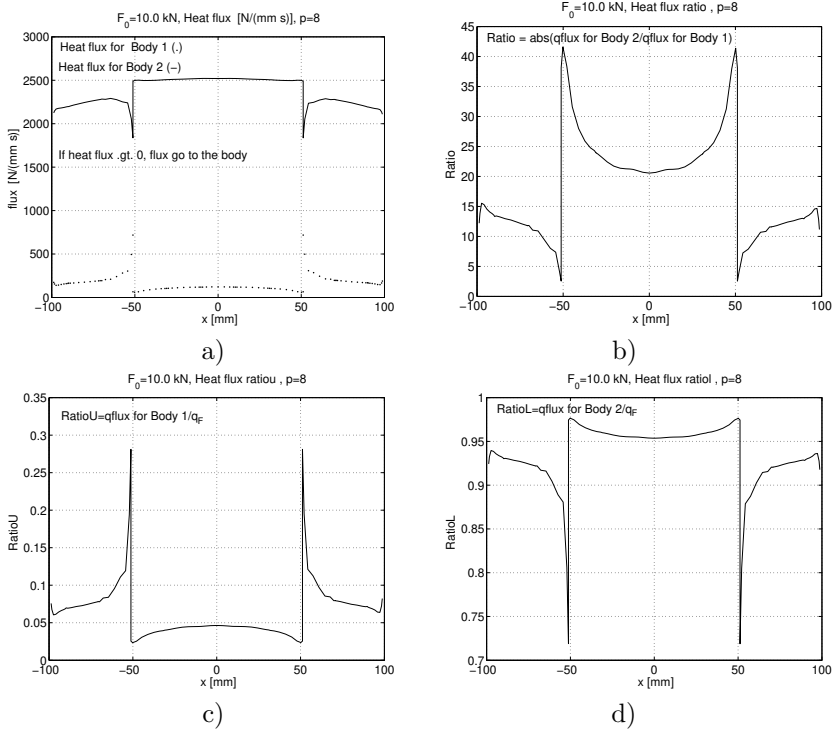


Figure 10. a) Heat flux for Body 1 and 2,
 b) Fluxratio: $\text{Ratio} = \text{Flux}2/\text{Flux}1$,
 c) Flux ratio for the shoe: $\text{Ratio}U = \text{Flux}1/q_F$, ($q_F = \mu p_n R_0 \omega$),
 d) Flux ratio for the disk: $\text{Ratio}L = \text{Flux}2/q_F$ at clockwise rotation at angular velocity $\omega = 5$ rad/s. Material of the shoe is heterogeneous, problem: Variant 3

position of pin O is fixed in the (\tilde{x}, \tilde{z}) reference system. The sliding velocity v_r of substrate B_2 relative to B_1 can be oriented in the rightward or leftward directions. In the \tilde{x}, \tilde{z} system the position of the pin O is $(\tilde{x}, \tilde{z}) = (l_{\tilde{x}}, O)$. In our case the vertical wear velocity is $\dot{\lambda}_F = -\dot{\lambda}_F \tilde{e}_x$, the angular velocity is $\dot{\lambda}_M = -\dot{\lambda}_M \tilde{e}_y$, so the rigid body velocity of the point P on the contact surface S_c is oriented along the vector

$$e_R = \frac{-(\dot{\lambda}_F \tilde{e}_x + \dot{\lambda}_M \tilde{e}_y \times \Delta \mathbf{r})}{H} = \frac{-(\dot{\lambda}_F + \dot{\lambda}_M \tilde{z}) \tilde{e}_x - \dot{\lambda}_M l_{\tilde{x}} \tilde{e}_z}{H} = -\cos \alpha \tilde{e}_x - \sin \alpha \tilde{e}_z, \quad (3.1)$$

where

$$H = \sqrt{(\dot{\lambda}_F + \dot{\lambda}_M \tilde{z})^2 + (\dot{\lambda}_M l_{\tilde{x}})^2}$$

where t_{th} is the block thickness in the lateral direction y . The \mp signs refer to rightward and leftward sliding velocities. The non-linear equations (3.4) provide the values of Lagrange multipliers $\dot{\lambda}_F$ and $\dot{\lambda}_M$ specifying the rigid body translation and rotation wear velocities. They can be solved by applying the iterative Newton-Raphson technique.

The steady state regime occurs for $q = 1$ and then we have $c = b$, $Z(q = 1) = \sum_{i=1}^2 \tilde{\beta}_i v_r^{a_i}$.

In this case the contact pressure can be given in a simple form:

$$p_n = \frac{\dot{\lambda}_F + \dot{\lambda}_M \tilde{z}}{Z(q = 1)} = \frac{\dot{\lambda}_F + \dot{\lambda}_M \tilde{z}}{\sum_{i=1}^2 \tilde{\beta}_i v_r^{a_i}}, \quad (3.5)$$

hence, the pressure variation is a linear function of distance from the supporting pin.

Example 3

The bodies in contact are shown in Figure 12 with finite element mesh. The punch dimension in the horizontal direction is $L = 60$ mm, its height is $h = 100$ mm. The substrate strip is assumed to translate in the left direction, its measures: horizontal $0 \leq x \leq 1670$, vertical $0 \leq z \leq 100$ mm. The punch is loaded on the upper boundary $z = 200$ mm by the uniform pressure $\tilde{p} = 16.66$ MPa corresponding to the resultant vertical force $F_0 = 10$ kN. The thickness of punch and strip is $t_{\text{th}} = 10$ mm. The pin position is $l_{\tilde{x}} = 20$ mm. The punch motion in the vertical direction and rotation is associated with the wear velocity at the contact surface. The punch is assumed to be made of two materials. The lower punch portion of height 20 mm is characterized by the material parameters of Material 2, see Table 1. The upper punch portion is

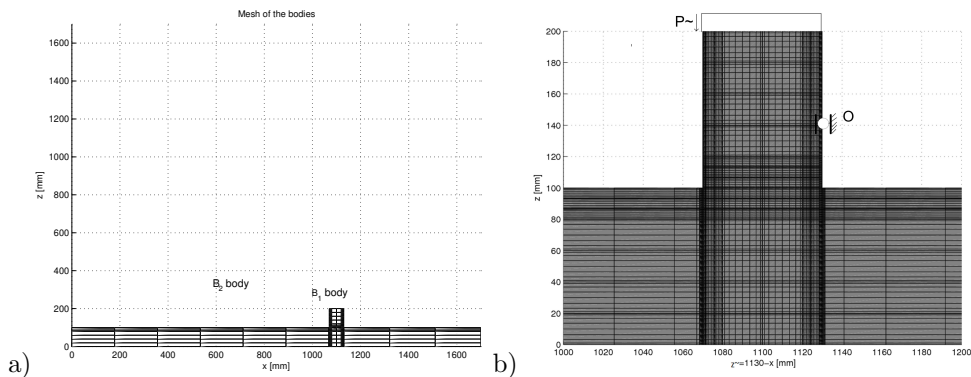


Figure 12. a) Finite element mesh, b) part of mesh for p -version finite element calculation. Load in the border $z = 200$ is $\tilde{p} = 16.66$ MPa, pin is located at the point $x = 1130$ mm, $z = 140$ mm, ($\tilde{z} = 0$, $\tilde{x} = 40$ mm)

assumed to be made of steel characterized by the parameters of Material 1. It is supposed that the ambient temperature θ_a of the surrounding medium is equal to zero. The coefficient of friction between bodies equals $\mu = 0.25$. On the boundaries $z = 0$ and $x = 1670$ mm the temperature is specified as $\theta_a = 0$, on the other parts of the boundary ($x \in S_q^{(i)}$, $i = 1, 2$) the heat flux is specified by the convection rule between the bodies and the surrounding medium. The contact pressure in the steady state is deduced from the principle of minimum of wear dissipation power defined by (3.5).

In order to specify the steady wear state, an infinite length model of strip should be used for calculation of the temperature field. In fact, for increasing sliding velocity the length of the strip should also be increased. For solution of this problem infinite elements must be used instead of adding new elements on the left of finite strip end [4]. The number of elements in z direction is 7, 8 elements in the x direction in punch and in the strip at punch on the left and right side 11 and 4 elements.

Assuming $a = b = 1$, $Z(q = 1) = 0.0002$, we can calculate the contact pressure distribution for right and leftward sliding directions.

In this example, problems for different variants of data will also be solved.

1. Variant 1. Wear parameters are uniform, strip is made from Material 1 and for punch material the parameters are characterized in the interval $100 < z < 120$ as Material 2, in the other part as Material 1.
2. Variant 2. Wear parameters are not uniform. In the part of punch $50 \leq \tilde{z} \leq 60$, $0 \leq \tilde{z} \leq 10$ there is $Z_1 = Z(q = 1) = 0.0002$, and interval $10 \leq \tilde{z} \leq 50$ there is $Z_2 = Z(q = 1) = 0.0001$, but material parameters are the same as in Variant 1.
3. Variant 3. Wear parameters are as in Variant 2, and only in the interval $10 \leq \tilde{z} \leq 50$, $0 \leq z \leq 20$ are material parameters for Material 2.
4. Variant 4. Material of all bodies is steel, and wear parameters are uniform, $Z = Z_1 = \text{const.}$

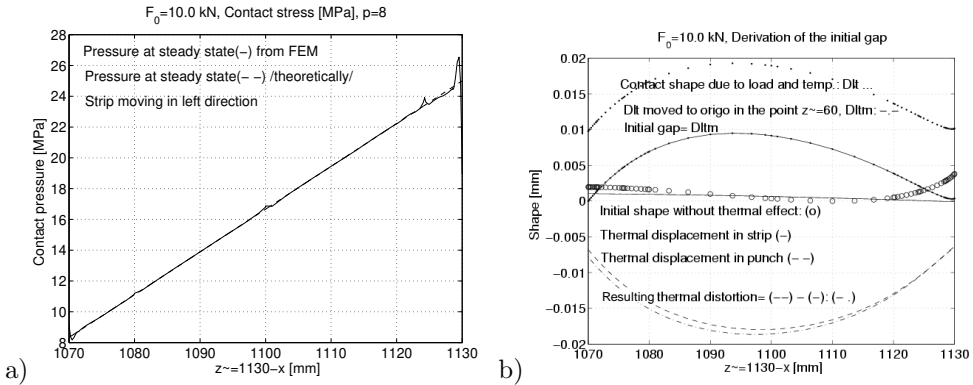


Figure 13. Variant 1: Solution of the const $\tilde{\beta}_1$ for leftward sliding direction of the strip: a) contact pressure distribution, b) contact surface gap form in the steady wear state

For Variant 1 the contact pressure is presented in Figure 13a, and the contact shape in Figure 13b. The difference between shapes specified neglecting (o) or accounting for temperature effect (— · —) is remarkable.

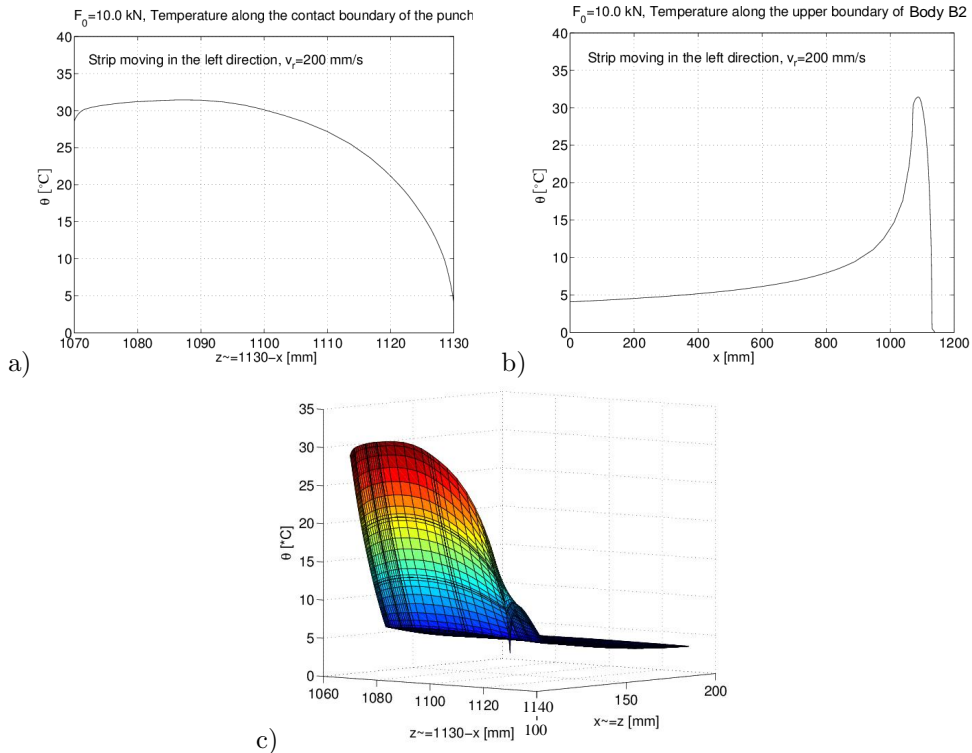


Figure 14. Variant 1: Temperature distribution for leftward sliding direction of the strip, a) in the shoe, b) in the strip, c) on the $x - z$ plane. The wear parameter is uniform.

The temperature distribution in the contact zone of shoe is shown in Figure 14a, and in the strip interface $z = 100$ mm is in Figure 14b. On the right side of the punch the temperature is practically zero, and on the left side far from punch position the temperature is very small. (The strip is moving in the left direction). The punch temperature on the left side is higher than that on the right side. The punch temperature also varies along direction z . It has a very different form for Variant 4 (see Figure 20b). In Variants 1-3 in the region of material 2 the gradient is very large, next it decreases to small values.

For Variant 4 the temperature variation is nearly constant. In other cases, material 2 provides a resistive barrier against the temperature transfer (see Figures 17, 19). Since upwinding Petrov-Galerkin technique was used for the numerical solution, the specified temperature field does not exhibit any oscillations.

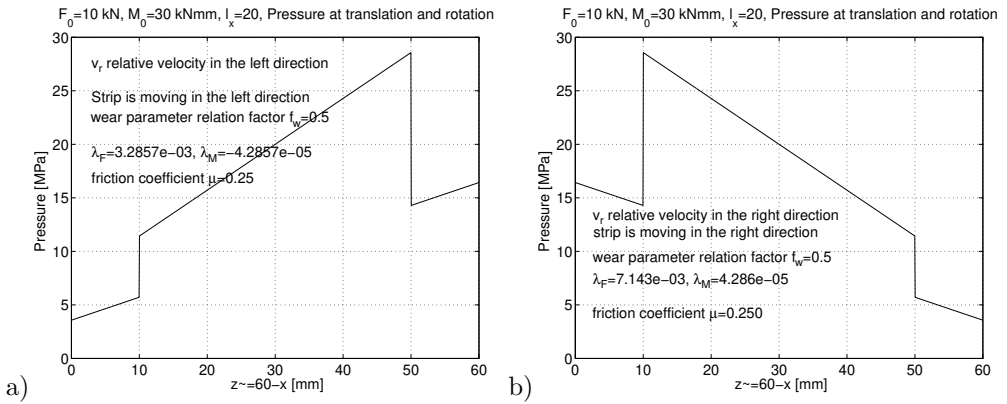


Figure 15. Variant 2,3: Contact pressure distribution for not uniform $\tilde{\beta}_1$: a) for leftward sliding direction of the strip, b) for rightward sliding direction of the strip, $f_w = Z_2/Z_1$

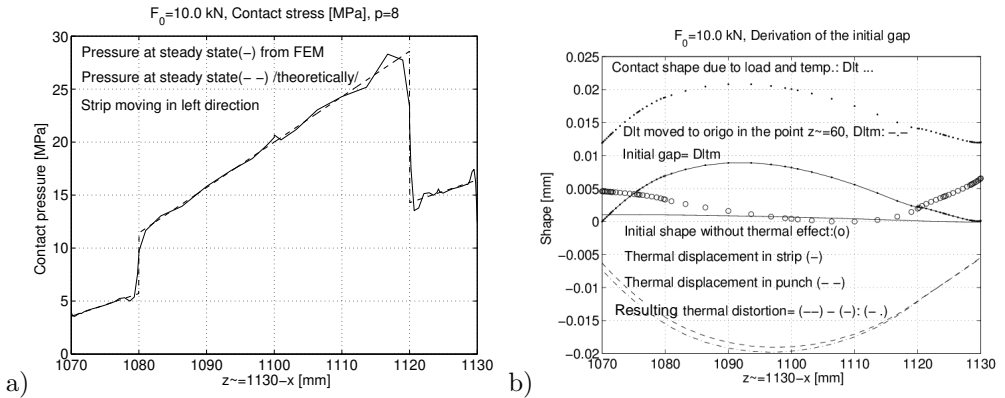


Figure 16. Variant 2: Solution of not uniform $\tilde{\beta}_1$ for leftward sliding direction of the strip: a) contact pressure distribution, b) contact gap for steady wear state, $f_w = Z_2/Z_1 = 0.5$

In Figure 15 the theoretically determined distributions of contact pressure for Variants 2 and 3 are shown for different sliding directions of the strip. Figures 16 and 17 present the collected pressure, wear shape and temperature fields for Variant 2. The results for Variant 3 are collected in Figures 18 and 19.

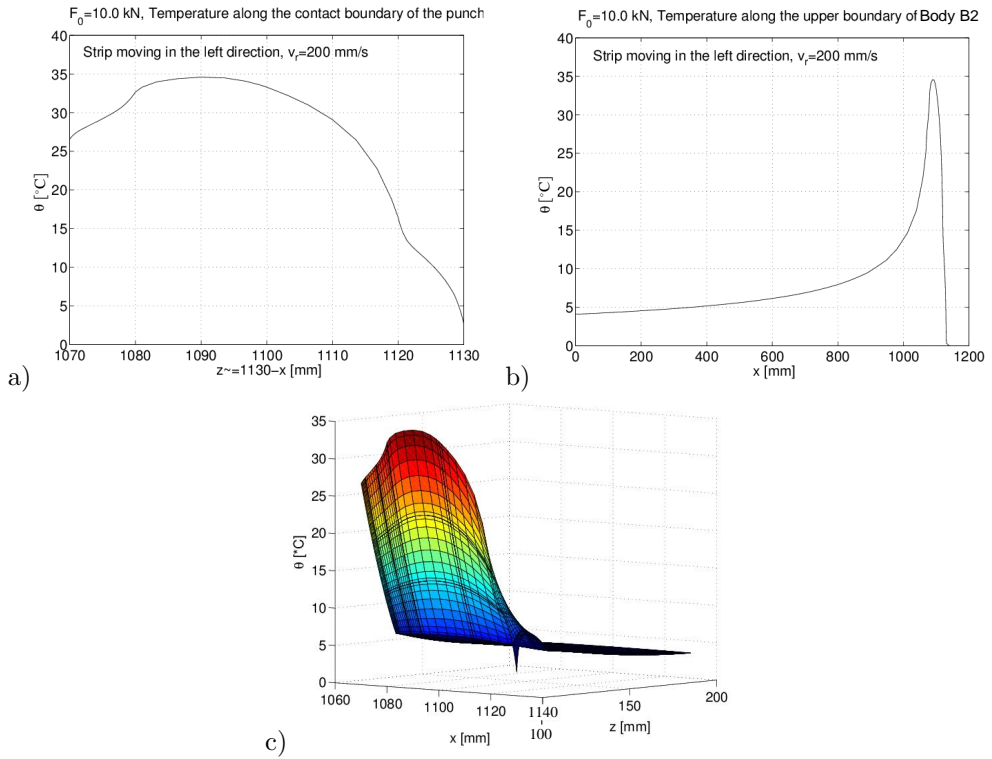


Figure 17. Variant 2: Temperature distribution for leftward sliding direction of the strip: a) in the shoe, b) in the strip, c) on the plane $x - z$. The wear parameter is non uniform, $f_w = Z_2/Z_1 = 0.5$.

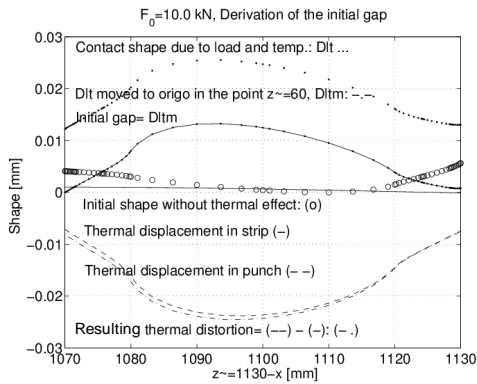


Figure 18. Variant 3: Solution for the non-uniform $\tilde{\beta}_1$ and leftward sliding direction of the strip: contact gap form for steady wear state

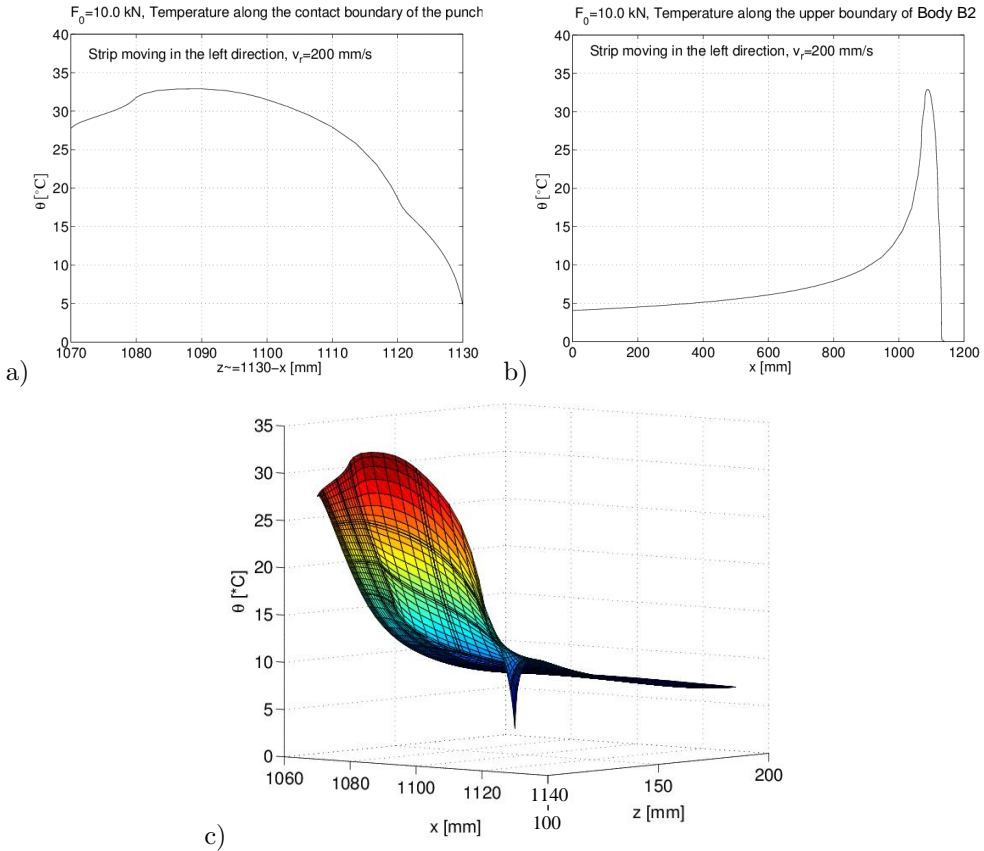


Figure 19. Variant 3: Temperature distribution for leftward sliding direction of the strip: a) in the shoe, b) in the strip, c) in the plane $x - z$. The wear parameter is not uniform, $f_w = Z_2/Z_1 = 0.5$.

Comparing results of Variants 2 and 3, it is noted that the temperature at the center of contact zone is a little bit larger for Variant 2 since then on both sides of the contact zone the material is steel and its coefficient of conductivity is larger. The initial gap at steady wear state is larger for Variant 3, since then the temperature distortions smaller relative to Variant 2 (see Figure 16b, Figure 18). Certainly, for the Variant 4 design (steel is used for all elements) the temperature is lowest relative to the other variants (see Figure 20).

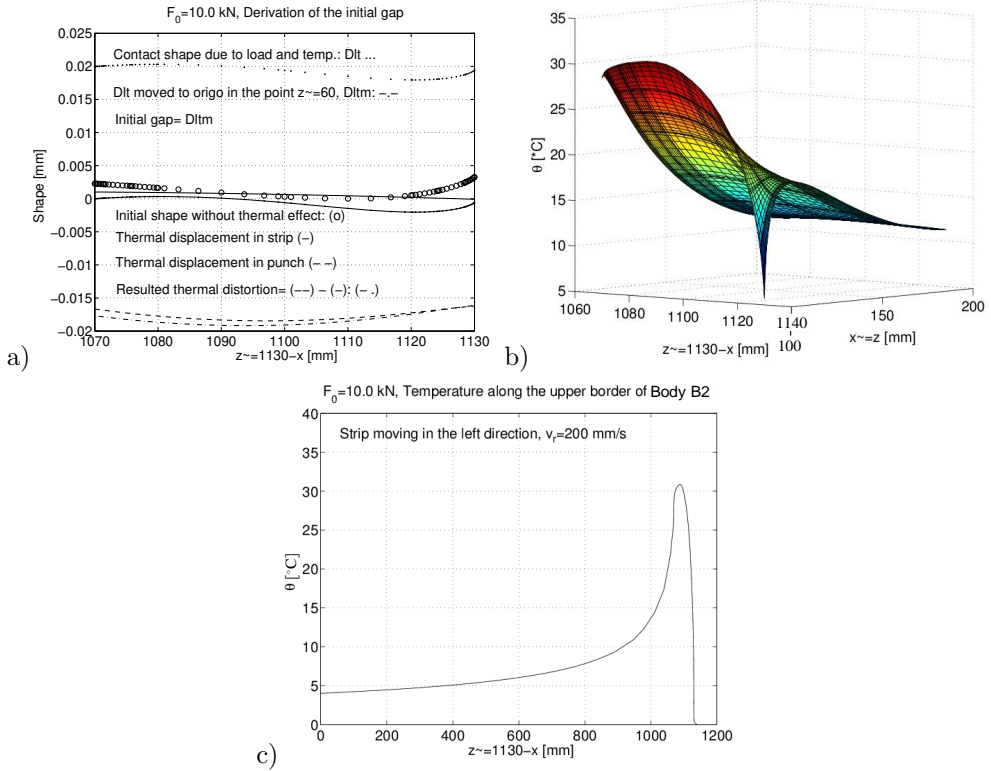


Figure 20. Variant 4: Material: steel, wear parameters are homogeneous. a) contact gap shape: b) temperature in the shoe (in the plane $x - z$), c) temperature in the strip

4. PERIODIC SLIDING: WEAR DISSIPATION IN PERIODIC MOTION AND MAIN PRESSURE IN A PERIODIC STEADY WEAR STATE

Consider now the periodic sliding motion, so that the relative displacement satisfies the condition

$$u_{\tau}(t) = u(t + T_*) , \tag{4.1}$$

where T_* is the period of sliding oscillation. In the steady wear state, the elastic stress and strain will vary periodically, thus

$$\varepsilon(t) = \varepsilon(t + T_*), \sigma(t) = \sigma(t + T_*). \tag{4.2}$$

The numerical treatments of oscillating sliding motion by Peigney [13] and Kim et. al. [14] and the analytical investigation of Goryacheva et. al. [15] indicate the existence of steady states attained in the wear process.

In this section we shall analyze the wear process induced by the reciprocal strip translation, assuming $\tilde{\beta}_1 \neq 0, \tilde{\beta}_2 = 0$, i.e. accounting only for punch wear.

In [5] the wear parameter $\tilde{\beta}_1$ was supposed to be uniform in the contact zone. In the present analysis it is assumed that the wear parameter varies along the sliding x coordinate. We investigate these problems without friction heat generation in the contact surface. The heat generation was taken into account in [16] at uniform wear parameters.

During the steady periodic response the wear increment accumulated during one cycle should be compatible at each point $x \in S_c$ with the rigid body punch motion.

In the analysis the contact pressure distribution is assumed to be fixed during a semi-cycle and varies discontinuously during sliding reversal in consecutive semi-cycles [5].

The wear dissipation work for periodic motion is

$$E_w = \frac{1}{2} \sum_{i=1}^2 \int_0^{T_*/2} \left(\int_{S_c^{(i)}} \mathbf{t}_i^{c+} \cdot \dot{\mathbf{w}}_i^+ dS \right) d\tau + \frac{1}{2} \sum_{i=1}^2 \int_{T_*/2}^{T_*} \left(\int_{S_c^{(i)}} \mathbf{t}_i^{c-} \cdot \dot{\mathbf{w}}_i^- dS \right) d\tau \quad (4.3)$$

where $\mathbf{t}_i^{c+}, \mathbf{t}_i^{c-}$ are the contact traction vectors and $\dot{\mathbf{w}}_i^+, \dot{\mathbf{w}}_i^-$ are the wear velocities of the i^{th} body in the progressive and reciprocal motion direction, T_* is the period of sliding motion, $T_* = 2\pi/\omega$ and ω is the angular velocity.

The strip slides periodically in the horizontal direction, thus we can write

$$\mathbf{u}_\tau = -u_0 \cos \omega \tau \mathbf{e}_x = u_0 \cos \omega \tau \mathbf{e}_{\tilde{z}}. \quad (4.4)$$

In our case the relative tangential velocity is (see Figure 11):

$$\mathbf{u}_\tau = \dot{\mathbf{u}}_\tau^{(2)} - \dot{\mathbf{u}}_\tau^{(1)} = -u_0 \omega \sin \omega \tau \mathbf{e}_{\tilde{z}} = -u_0 \omega \sin \omega \tau \mathbf{e}_\tau = -v_\tau \mathbf{e}_\tau \quad (4.5)$$

with the corresponding shear stress acting on the body B_1 along $-\mathbf{e}_\tau$. The integral over one period of the relative velocity between the bodies is

$$\int_0^{T_*/2} v_\tau d\tau = \int_{T_*/2}^{T_*} v_\tau d\tau = 2u_0 \quad (4.6)$$

In view of the wear rule (1.1) the wear dissipation for the punch of Figure 12 is

$$E_w = \frac{1}{2} \int_0^{T_*/2} \left(\int_{S_c^{(1)}} p_n^+ \dot{w}_{1,n}^+ dS \right) d\tau + \frac{1}{2} \int_{T_*/2}^{T_*} \left(\int_{S_c^{(1)}} p_n^- \dot{w}_{1,n}^- dS \right) d\tau \quad (4.7)$$

and for $\tilde{\beta}_1 \neq 0, \tilde{\beta}_2 = 0, a_1 = b_1 = 1$ there is

$$\frac{E_w}{2u_0} = \int_{S_c^{(1)}} \tilde{\beta}_1 \left\{ (p_n^+)^2 + (p_n^-)^2 \right\} dS = \frac{E_w^+}{2u_0} + \frac{E_w^-}{2u_0}. \quad (4.8)$$

In the steady wear state E_w reaches a minimum value. Let us note that p_n^+ and p_n^- are not uniformly distributed on the contact interface. Take the coordinate $\tilde{z} = 1130 - x$.

Assume the rigid body wear velocities for left (-) and right (+) directions of the substrate sliding motion in the following form:

$$\dot{\lambda}_F^- = -\dot{\lambda}_F^- \mathbf{e}_z, \dot{\lambda}_M^- = \dot{\lambda}_M^- \mathbf{e}_y, \dot{\lambda}_F^+ = -\dot{\lambda}_F^+ \mathbf{e}_z, \dot{\lambda}_M^+ = -\dot{\lambda}_M^+ \mathbf{e}_y. \quad (4.9)$$

Thus the velocities at an arbitrary point of punch are

$$-(\dot{\lambda}_F^- - \dot{\lambda}_M^- \tilde{z}) \mathbf{e}_z, \quad \text{or} \quad -(\dot{\lambda}_F^+ + \dot{\lambda}_M^+ \tilde{z}) \mathbf{e}_z. \quad (4.10)$$

After time integration there is $\Delta \lambda_{F,M}^+ = \int_0^{T_*/2} \dot{\lambda}_{F,M}^+ d\tau$, $\Delta \lambda_{F,M}^- = \int_{T_*/2}^{T_*} \dot{\lambda}_{F,M}^- d\tau$

and the displacements resulting from these velocities are

$$-(\Delta \lambda_F^+ + \Delta \lambda_M^+ \tilde{z}) \mathbf{e}_z \quad \text{and} \quad -(\Delta \lambda_F^- + \Delta \lambda_M^- \tilde{z}) \mathbf{e}_z. \quad (4.11)$$

Thus, the total wear accumulated during one sliding cycle is

$$\Delta w_n = \Delta w_n^+ + \Delta w_n^- = (\Delta \lambda_F^+ + \Delta \lambda_F^-) + (\Delta \lambda_M^+ - \Delta \lambda_M^-) \tilde{z}. \quad (4.12)$$

This value of the wear can be calculated from the wear law supposing $\tilde{\beta}_1 \neq 0$, $\tilde{\beta}_2 = 0$ and $a_1 = b_1 = 1$,

$$\Delta w_n = \Delta w_n^+ + \Delta w_n^- = U \tilde{\beta}_1 (p_n^+ + p_n^-) = U \tilde{\beta}_1 p_\Sigma = 2U \tilde{\beta}_1 p_m, \quad (4.13)$$

where $p_m = (p_n^+ + p_n^-)/2$ is the main cyclic pressure, $p_\Sigma = (p_n^+ + p_n^-) = 2p_m$ is the sum of contact pressure, $U = \int_0^{T_*/2} v_r d\tau = 2u_0$.

Comparing (4.12), (4.13), it is seen that the distribution of the modified mean contact pressure values of consecutive semi-cycles must be a linear function of position, thus

$$p_{\text{mod}\Sigma}(\tilde{z}) = \tilde{\beta}_1(\tilde{z}) p_\Sigma(\tilde{z}) = \tilde{\beta}_1(\tilde{z}) 2p_m(\tilde{z}) = \tilde{\beta}_1(\tilde{z}) 2(p_m^C + p_m^L \tilde{z}), \quad (4.14)$$

i.e.

$$\begin{aligned} \Delta w_n = \Delta w_n(\tilde{z}) &= \Delta w_n^+ + \Delta w_n^- = (\Delta \lambda_F^+ + \Delta \lambda_F^-) + (\Delta \lambda_M^+ - \Delta \lambda_M^-) \tilde{z} = \\ &= \tilde{\beta}_1(\tilde{z}) \int_0^{T_*/2} \|\dot{\mathbf{u}}_\tau\| d\tau 2(p_m^C + p_m^L \tilde{z}) = U \tilde{\beta}_1(\tilde{z}) 2(p_m^C + p_m^L \tilde{z}) = \\ &= U \tilde{\beta}_1(\tilde{z}) p_\Sigma(\tilde{z}) = U p_{\text{mod}\Sigma}(\tilde{z}), \end{aligned} \quad (4.15)$$

where $\Delta \lambda_{F,M}^\pm$ is the increment of rigid body wear velocities in the half period time.

Using the equilibrium equations for summed loads, the summed pressure for the steady wear state is determined for $\tilde{\beta}_1 = \text{const}$ as

$$\begin{aligned} p_m^C &= \frac{F_0}{S_c} - \frac{3F_0(-L + 2\tilde{z}_F)}{LS_c}, p_m^L = \frac{6F_0(-L + 2\tilde{z}_F)}{L^2 S_c}, \\ p_\Sigma &= 2p_m = p_n^+ + p_n^- = 2(p_m^C + p_m^L \tilde{z}) \end{aligned} \quad (4.16)$$

where \tilde{z}_F is the coordinate of the resultant load $F_0 = F_0(p^-)$. For non-negativity of p_m there should be $L/2 \leq \tilde{z}_F \leq 2L/3$. Here S_c is the area of contact zone.

For $\tilde{\beta}_1 \neq \text{const}$ it turns out that the summed contact pressure is linear but not-continuous function (see Figure 15), but the modified function $p_{\text{mod}\Sigma}(\tilde{z}) = \tilde{\beta}_1(\tilde{z})p_\Sigma(\tilde{z})$ is linear and continuous.

The equilibrium equations are

$$F_0 = t_{\text{th}} \int_0^L p_m(\tilde{z}) d\tilde{z}, \quad M_0 = t_{\text{th}} \int_0^L \tilde{z} p_m(\tilde{z}) d\tilde{z}. \quad (4.17)$$

In view of Figure 21, where the distribution of mean cyclic contact pressure is presented, we can write the following algebraic equation system for calculation of the values p_m^C, p_m^L

$$\begin{bmatrix} A_{11} & A_{12} \\ A_{21} & A_{22} \end{bmatrix} \begin{bmatrix} p_m^C \\ p_m^L \end{bmatrix} = \frac{1}{t_{\text{th}}} \begin{bmatrix} F_0 \\ M_0 \end{bmatrix}, \quad (4.18)$$

where

$$A_{11} = \tilde{z}_1 + \frac{\tilde{\beta}_s}{\tilde{\beta}_m}(\tilde{z}_4 - \tilde{z}_1) + \tilde{z}_5 - \tilde{z}_4,$$

$$A_{12} = A_{21} = \frac{1}{2} \left[\tilde{z}_1^2 + \frac{\tilde{\beta}_s}{\tilde{\beta}_m}(\tilde{z}_4^2 - \tilde{z}_1^2) + \tilde{z}_5^2 - \tilde{z}_4^2 \right],$$

$$A_{22} = \frac{1}{3} \left[\tilde{z}_1^3 + \frac{\tilde{\beta}_s}{\tilde{\beta}_m}(\tilde{z}_4 - \tilde{z}_1)(\tilde{z}_1^2 + \tilde{z}_4^2 + \tilde{z}_1\tilde{z}_4) + (\tilde{z}_5 - \tilde{z}_4)(\tilde{z}_4^2 + \tilde{z}_5^2 + \tilde{z}_4\tilde{z}_5) \right].$$

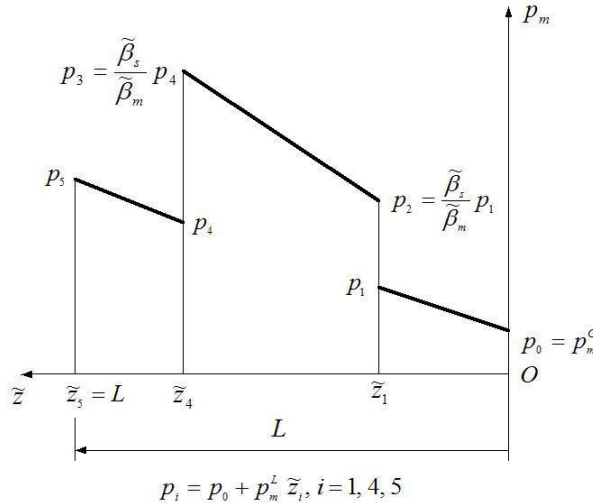


Figure 21. Distribution of the main cyclic pressure, $(\tilde{\beta}_s/\tilde{\beta}_m = 2)$

Here $\tilde{\beta}_s$ is the wear parameter for interval $0 \leq \tilde{z} \leq \tilde{z}_1$ and $\tilde{z}_4 \leq \tilde{z} \leq \tilde{z}_5$. In the interval $\tilde{z}_1 \leq \tilde{z} \leq \tilde{z}_4$ the wear parameter is $\tilde{\beta}_m$.

The wear increment in one period (as was mentioned the contact pressure is fixed in half period)

$$\Delta w_n = \tilde{\beta}_1 [p_n^+ + p_n^-] (u_0 \omega) \int_0^{T_*/2} |\sin \omega \tau| d\tau = \tilde{\beta}_1 2p_m 2u_0,$$

which using (4.16) provides the simple relation

$$\Delta w_n = \Delta w_n(\tilde{z}) = 2U\tilde{\beta}_1(p_m^C + p_m^L\tilde{z}) = U\tilde{\beta}_1(\tilde{z})p_\Sigma(\tilde{z}) = Up_{\text{mod}\Sigma}(\tilde{z}). \quad (4.19)$$

The averaged wear rate in one period

$$\dot{\bar{w}}_n = \frac{\Delta w_n}{T_*} = \tilde{\beta}_1 \frac{U(p_n^+ + p_n^-)}{T_*} = \frac{Up_{\text{mod}\Sigma}}{T_*}. \quad (4.20)$$

If the rigid body wear velocity $\lambda_M^+ = \lambda_M^- = 0$, then in the steady periodic wear regime the uniform wear increment is accumulated during the full cycle at each point of the contact zone and the following condition should be satisfied:

$$\tilde{\beta}_1(\tilde{z})(p_n^+(\tilde{z}) + p_n^-(\tilde{z})) = \tilde{\beta}_1(\tilde{z})2p_m(\tilde{z}) = \tilde{\beta}_1(\tilde{z})p_\Sigma(\tilde{z}) = p_{\text{mod}\Sigma}(\tilde{z}) = \text{const.} \quad (4.21)$$

The steps of time integration of the wear rate rule can be found in [5].

Example 4

Let us analyze the wear of the punch (Body 1) shown in Figure 12. The following geometric parameters are assumed: the punch width is $L = 60$ mm, its height is $h = 100$ mm, the thickness of punch and strip is $t_{\text{th}} = 10$ mm.

The wear parameters are: $\tilde{\beta}_1 = 1.25\pi \cdot 10^{-5}$, $\tilde{\beta}_2 = 0$, $a = b = 1$, the coefficient of friction is $\mu = 0.25$. The horizontal displacement of the substrate is $u_\tau = -u_0 \cos \omega \tau$, where $u_0 = 1.5$ mm, $\omega = 10$ rad/s, τ is the time. The material parameters are presented in Table 1.

The upper parts of the punch and strip are assumed to be made of the same material (Material 1, see Table 1). The lower punch portion of height 20 mm is characterized by the parameters of Material 2, see Table 1.

4.1. Symmetric load (Load case 1). Consider a symmetric punch loading on the upper boundary $z = 200$ mm at the uniform pressure $\tilde{p} = 16.66$ MPa corresponding to the resultant vertical force $F_0 = 10$ kN.

In the intervals $50 \leq \tilde{z} \leq 60$, $0 \leq \tilde{z} \leq 10$ the wear parameter $\tilde{\beta}_{10} = \tilde{\beta}_1$, and interval $10 \leq \tilde{z} \leq 50$, $\tilde{\beta}_{1m} = \tilde{\beta}_1/2$.

Then the modified summa of contact pressure is

$$p_{\text{mod}}(\tilde{z}) = \frac{\beta_1(\tilde{z})p_\Sigma(\tilde{z})}{\tilde{\beta}_{10}} \quad \text{if } 50 \leq \tilde{z} \leq 60, \quad 0 \leq \tilde{z} \leq 10$$

and

$$p_{\text{mod}}(\tilde{z}) = \frac{\beta_1(\tilde{z})p_\Sigma(\tilde{z})}{\tilde{\beta}_{1m}} \quad \text{if } 10 \leq \tilde{z} \leq 50.$$

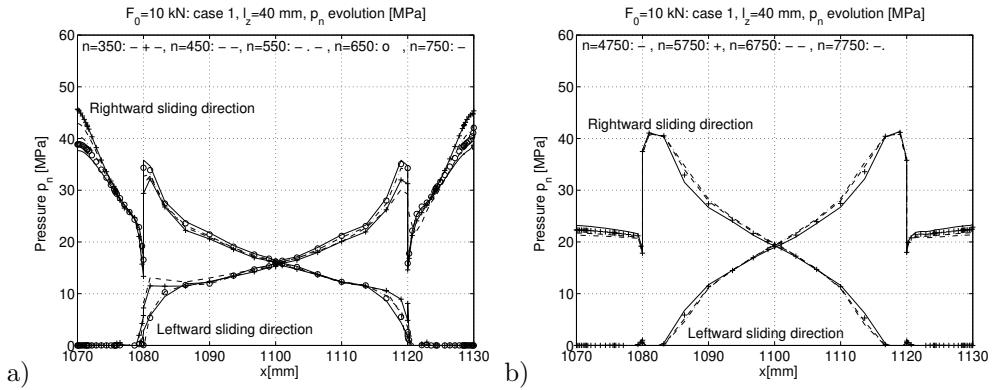


Figure 22. Contact pressure at different time steps

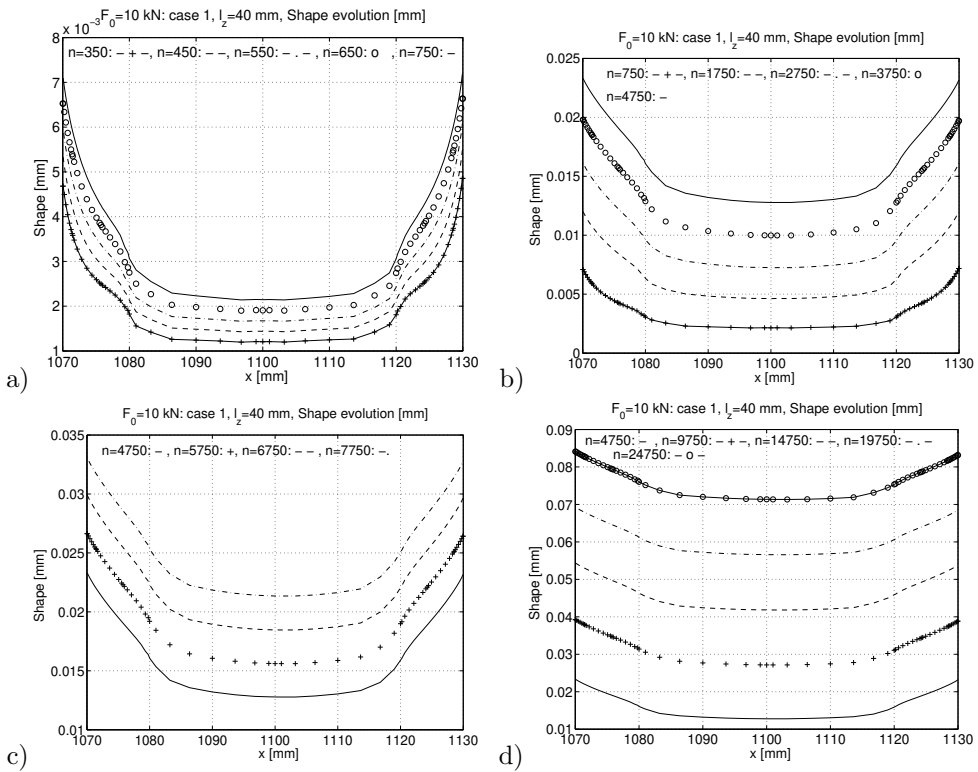
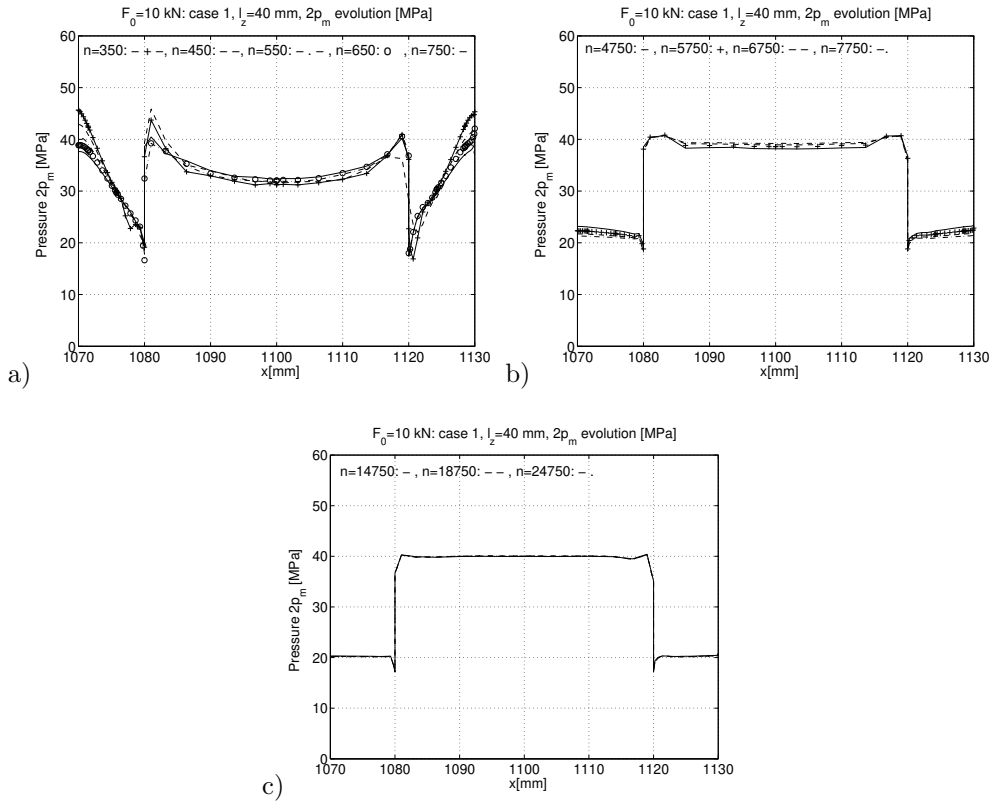


Figure 23. Shape evolution in the wear process



In our case the modified summa of contact pressure is $p_{\text{mod}}(\tilde{z}) = 20 \text{ MPa}$. In fact, we have from (4.18) ($p_m^C = p_0/2$)

$$2\tilde{p}L = 2\tilde{p}60 = p_010 + p_040 \cdot 2 + p_010 = p_0100, \quad p_0 = 1.2\tilde{p} = p_{\text{mod}}(\tilde{z}).$$

In the steady wear state this relation must be preserved in each period. In this case, Body 1 translates in the vertical direction at the constant velocity $\dot{\lambda}_F$. The numerical solution follows this theoretical result (see Figures 22–25). Here n is the number of half periods. It is clear that after $n \geq 14000$ the steady cyclic wear state is reached, the functions of sum of contact pressures (Figure 24) and the modified sum of contact pressures (Figure 25) are fixed in time.

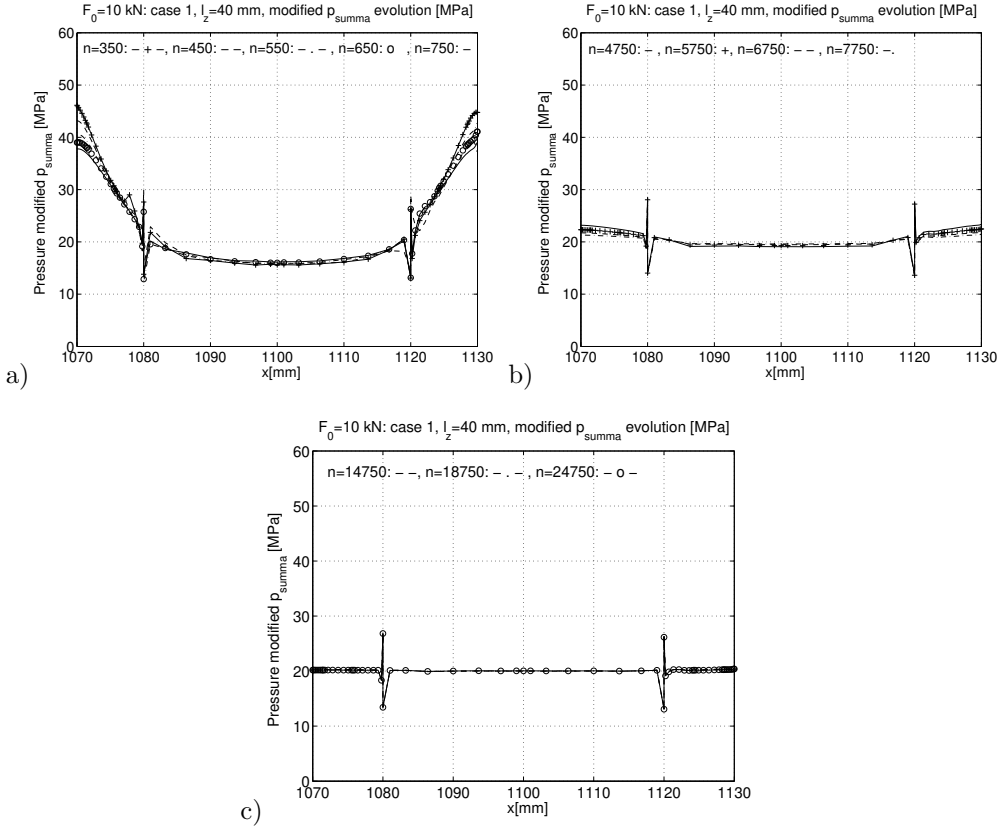


Figure 25. Modified sum of contact pressures in one cycle

4.2. Non-symmetric load (Load case 2). Let us now analyze the case of eccentric load when the resultant vertical force is $F = 10$ kN. The pressure $\tilde{p} = 20$ MPa is applied in the interval $10 \leq \tilde{z} \leq 60$. The resultant position coordinate is $\tilde{z}_F = 35$ mm.

Solving (4.18) we find $p_m^C = 3.572$ MPa, $p_m^L = 0.2143$ MPa/mm.

The numerical analysis results are shown in Figures 26-29. They demonstrate a good approximation of the theoretical values of the modified summed contact pressure. The maximum of difference is smaller than 5% (see Figure 29).

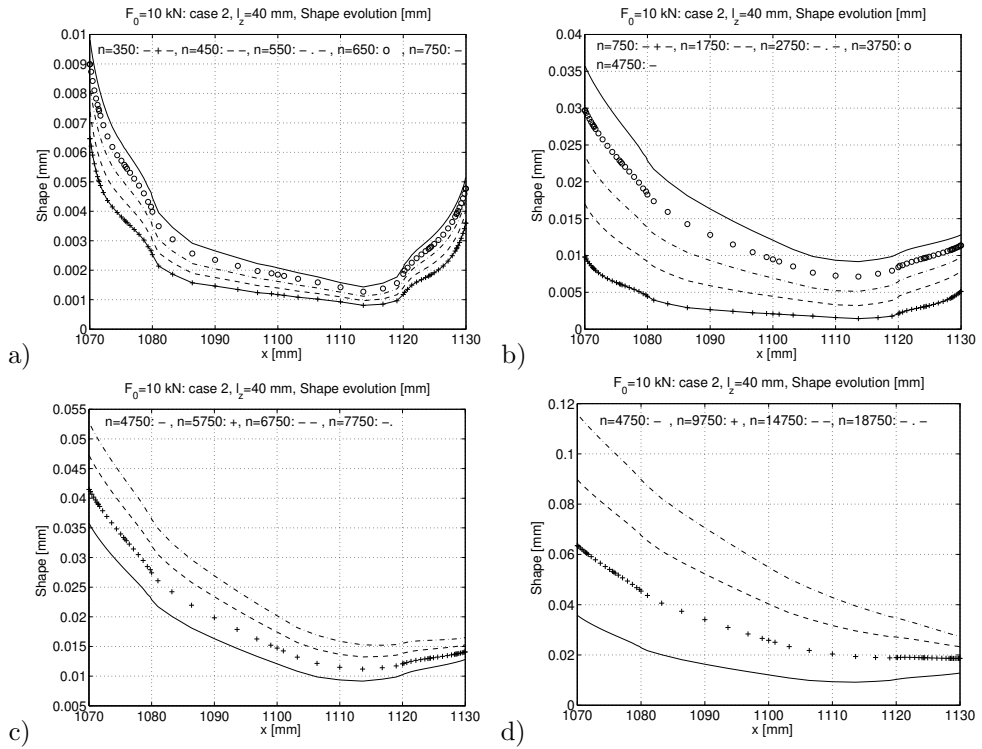


Figure 26. Shape evolution in the wear process

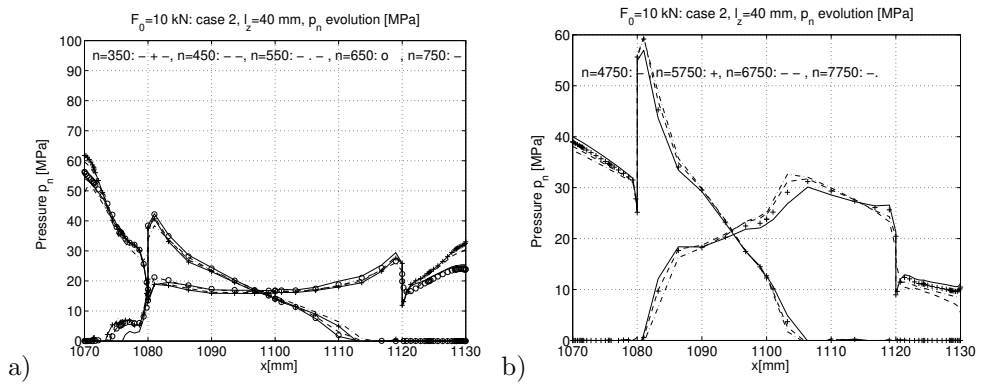


Figure 27. Contact pressure at different time steps

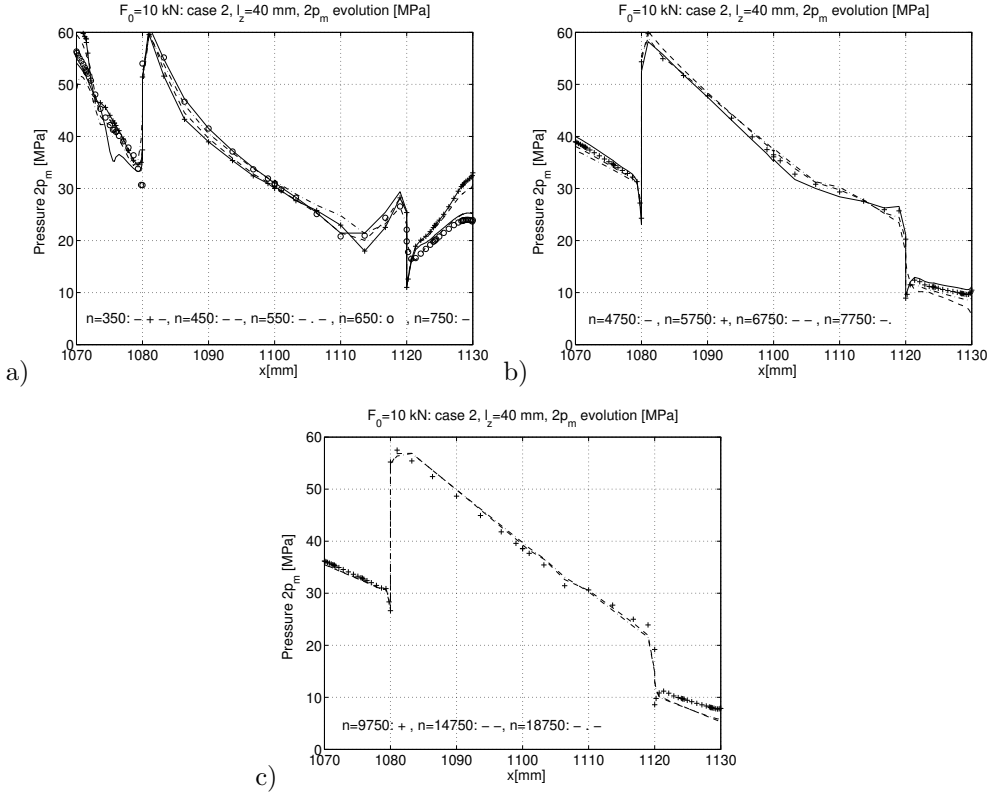


Figure 28. Summa of contact pressures in one cycle

At the interface of different material the stress state exhibits a singularity, which is manifested by a discontinuity of the contact stresses (see Figures 27-29).

5. STEADY STATE CONDITIONS FOR PERIODIC LOADING

Consider now the steady state wear problem for the case of a punch sliding monotonically on a flat substrate and subjected to periodic normal loading. The steady state conditions at each point of the contact zone are now expressed as follows:

$$u_\tau(t) = u_\tau(t + T_*), \quad \boldsymbol{\sigma}(t) = \boldsymbol{\sigma}(t + T_*), \quad \boldsymbol{\varepsilon}(t) = \boldsymbol{\varepsilon}(t + T_*), \quad (5.1)$$

where T_* is the period of loading, $\boldsymbol{\sigma}$ and $\boldsymbol{\varepsilon}$ are the stress and the strain fields. The related cyclic wear increment accumulated during one cycle is assumed to be compatible with the rigid body wear motion of punch, thus

$$w_n(x, t + T_*) - w_n(x, t) = \Delta w_n(x, T_*) = (\Delta \boldsymbol{\lambda}_F + \Delta \boldsymbol{\lambda}_M \times \Delta \boldsymbol{r}) \cdot \boldsymbol{n}_c, \quad (5.2)$$

where $\Delta \boldsymbol{\lambda}_F$ and $\Delta \boldsymbol{\lambda}_M$ are the translational and rotational cyclic wear increments.

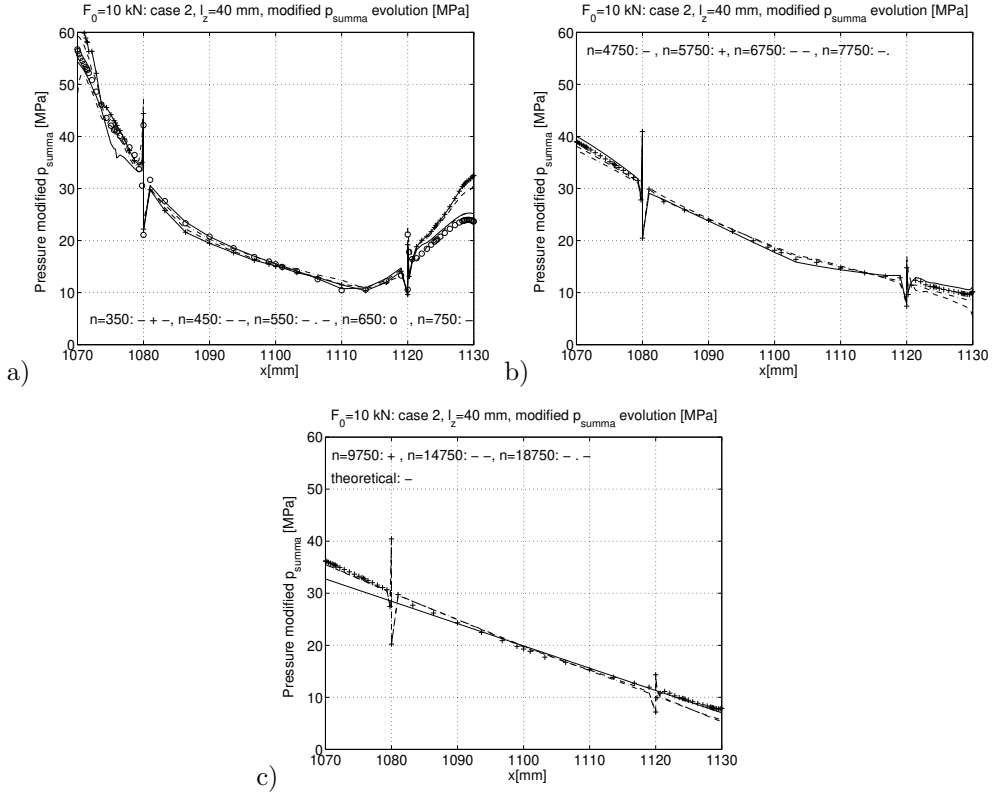


Figure 29. Modified sum of contact pressures in one cycle

For the simplification of calculations of the relative velocity between the bodies it is assumed that

$$\dot{\mathbf{u}}_{\tau} = \dot{\mathbf{u}}_{R,\tau}^{(2)} - \dot{\mathbf{u}}_{R,\tau}^{(1)} = \dot{\mathbf{u}}_{R,\tau} = -\|\dot{\mathbf{u}}_{\tau}\| \mathbf{e}_{\tau 1} = -v_r \mathbf{e}_{\tau 1} = -v_r \mathbf{e}_x \quad (5.3)$$

since the elastic and wear relative velocities are very small as compared to specified rigid body velocities $\dot{\mathbf{u}}_{R,\tau}^{(1)}$ and $\dot{\mathbf{u}}_{R,\tau}^{(2)}$ generating the sliding regime

$$\|\dot{\mathbf{u}}_{e,\tau}\| = \left\| \dot{\mathbf{u}}_{e,\tau}^{(2)} - \dot{\mathbf{u}}_{e,\tau}^{(1)} + \dot{\mathbf{w}}_{2,\tau} - \dot{\mathbf{w}}_{1,\tau} \right\| \ll \|\dot{\mathbf{u}}_{R,\tau}\| = \left\| \dot{\mathbf{u}}_{R,\tau}^{(2)} - \dot{\mathbf{u}}_{R,\tau}^{(1)} \right\|. \quad (5.4)$$

The substrate is assumed to slide monotonically in the leftward direction. The analysis presented pertains to the case when wear of punch or combined wear of punch and substrate occurs. Then the cyclic wear increment at the contact is controlled by the rigid body motion of one of the contacting bodies. The contact shape evolution during consecutive cycles assures stress and strain periodicity.

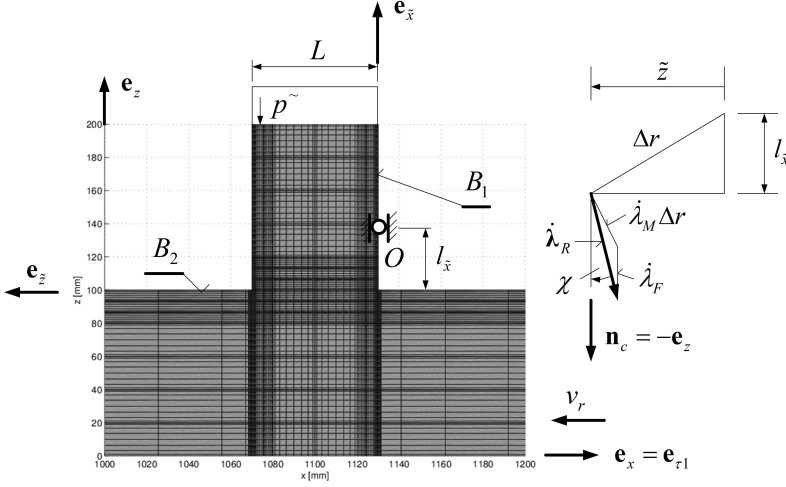


Figure 30. Mesh of punch constrained at O and of central part of the strip. Rigid body wear velocity λ_R . Strip is moving in leftward direction.

To simplify the analysis, only the case of punch wear is considered and the wear parameters are $\tilde{\beta}_1 \neq 0$, $\tilde{\beta}_2 = 0$, $a = b = 1$. In paper [6] it was supposed that wear parameters are uniform. In the following it is assumed that wear parameters are non-uniform.

Consider the periodic loading applied to punch B_1 in the direction $-e_z$. (see Figure 30). The resultant vertical load is now expressed as

$$\mathbf{F} = -F\mathbf{e}_z = F = F_0 + F_A |\sin \omega \tau| \geq 0, \quad (5.5)$$

where F_0 is the constant load, F_A and ω are the load amplitude and frequency. In view of the constraint at O , the load generates the resulting moment M_0^y with respect to the y axis. The period of loading is $T_* = 2\pi/\omega$.

The loading on the upper punch boundary by uniform pressure $p\tilde{}$ is applied with the resulting load F . Referring to Figure 30, it is assumed that during the wear process the punch is allowed to translate in the normal contact direction and rotate around the constraining pin O .

The average load value in one cycle is

$$\bar{F} = \frac{1}{T_*} \int_0^{T_*} F \, d\tau = F_0 + \frac{2}{\pi} F_A. \quad (5.6)$$

The integrated wear velocity at the position x of the contact zone in one loading period is

$$\Delta \lambda_{F,M}(x) = \int_0^{T_*} \dot{\lambda}_{F,M}(x, \tau) \, d\tau \quad (5.7)$$

and the average wear velocity field is expressed as follows

$$\bar{\dot{\lambda}}_{F,M}(x) = \frac{\Delta \lambda_{F,M}}{T_*} = \frac{1}{T_*} \int_0^{T_*} \dot{\lambda}_{F,M}(x, \tau) \, d\tau. \quad (5.8)$$

The cyclic wear increment for the punch allowed to translate in the normal contact direction is

$$\Delta w_{1,n}(x) = \int_0^{T_*} \tilde{\beta}_1(x) p_n(x, \tau) v_r \, d\tau = \tilde{\beta}_1(x) v_r \int_0^{T_*} p_n(x, \tau) \, d\tau \quad (5.9)$$

and the average value in one period is

$$\Delta \bar{w}_{1,n}(x) = \frac{\Delta w_{1,n}(x)}{T_*} = \tilde{\beta}_1(x) v_r \frac{\int_0^{T_*} p_n(x, \tau) \, d\tau}{T_*}. \quad (5.10)$$

The wear volume in one period equals

$$\begin{aligned} \Delta W &= \int_{S_c} \Delta w_{1,n}(x) \, dS = \int_{S_c} \int_0^{T_*} \tilde{\beta}_1(x) p_n(x, \tau) v_r \, d\tau \, dS = \\ &= v_r \int_0^{T_*} \int_{S_c} \tilde{\beta}_1(x) p_n(x, \tau) \, dS \, d\tau = v_r \int_0^{T_*} F_\beta(\tau) \, d\tau \end{aligned} \quad (5.11)$$

since from the equilibrium equation it follows that $\int_{S_c} \tilde{\beta}_1(x) p_n(x, \tau) \, dS = F_\beta(\tau)$ and the average wear volume increment is

$$\Delta \bar{W} = \frac{\Delta W}{T_*} = \frac{v_r}{T_*} \int_0^{T_*} F_\beta(\tau) \, d\tau = v_r \bar{F}_\beta. \quad (5.12)$$

It is seen that $\Delta \bar{W}$ is explicitly related to the average modified load value \bar{F}_β . The contact traction vector in our case is expressed as $\mathbf{t}^c = \mathbf{t}_1^c = -\mathbf{t}_2^c = p_n \mathbf{e}_z - \mu p_n \mathbf{e}_x$, the wear velocity vectors are

$$\dot{\mathbf{w}}_R = \dot{\mathbf{w}}_2 - \dot{\mathbf{w}}_1, \dot{\mathbf{w}}_i = (-1)^i [-\dot{w}_{i,n} \mathbf{e}_z + \dot{w}_{i,\tau} \mathbf{e}_x], \quad i = 1, 2,$$

since the relative velocity is

$$\dot{\mathbf{u}}_\tau = \dot{\mathbf{u}}_x = \dot{\mathbf{u}}_{2,x} - \dot{\mathbf{u}}_{1,x} = -v_r \mathbf{e}_{\tau 1} = -v_r \mathbf{e}_x$$

and $\dot{w}_{i,\tau} = \dot{w}_{i,n} \tan \chi$, [6]. The punch width is equal to L . The thickness of two bodies is t_{th} , so the contact zone area equals $S_c = t_{th} L$. The position of the pin O in the vertical direction is denoted by $l_{\tilde{x}}$ (see Figure 30). Let $\tilde{z} = 1130 - x$ denote the typical contact point position relative to the right perimeter of contact zone.

Let us define the wear dissipation in one cycle of sliding motion

$$E_w = \frac{1}{2} \int_0^{T_*} \left(\int_{S_c} \mathbf{t}_1^c \cdot \dot{\mathbf{w}}_1 \, dS \right) d\tau \quad (5.13)$$

and the equilibrium equations for the punch

$$F - \int_{S_c} p_n \, dS = 0, \quad (5.14)$$

$$M - \int_{S_c} p_n [\tilde{z} + \mu l_{\tilde{x}}] \, dS = 0$$

where \tilde{z}_F is the position coordinate of the resultant load F .

The steady state conditions will be determined by minimizing the average wear dissipation in one cycle subject to punch equilibrium equations (5.14). The Lagrangian averaged functional is now expressed as follows

$$\begin{aligned} \bar{L}_w = & \frac{E_w}{T_*} - \frac{1}{T_*} \int_0^{T_*} \dot{\lambda}_F \left(\int_{S_c} p_n \, dS - F \right) d\tau - \\ & \frac{1}{T_*} \int_0^{T_*} \dot{\lambda}_M \left\{ \int_{S_c} p_n [\tilde{z} + \mu l_{\tilde{x}}] \, dS - M \right\} d\tau \end{aligned} \quad (5.15)$$

where in view of (5.13), there is

$$E_w = \frac{1}{2} \int_0^{T_*} \int_{S_c} \tilde{\beta}_1 v_r (p_n)^2 \{1 + \mu \tan \chi\} \, dS \, d\tau \quad (5.16)$$

and χ is the orientation angle of the wear velocity vector relative to the normal contact vector, thus $\tan \chi = \frac{\dot{\lambda}_M l_{\tilde{x}}}{\dot{\lambda}_F + \dot{\lambda}_M \tilde{z}}$, because

$$\dot{\mathbf{w}}_R = -\dot{\mathbf{w}}_1, \dot{\mathbf{w}}_1 = - \left[\dot{\lambda}_F + \dot{\lambda}_M \tilde{z} \right] \mathbf{e}_z - \dot{\lambda}_M l_{\tilde{x}} \mathbf{e}_x, \quad \mathbf{e}_R = \frac{\dot{\mathbf{w}}_R}{\|\dot{\mathbf{w}}_R\|}$$

(see Figure 30).

The Lagrangian multipliers represent the rigid body wear velocity components. Considering the variation of (5.15) and (5.16), the following expression is obtained:

$$\begin{aligned} \delta \bar{L}_w = & \frac{1}{T_*} \int_0^{T_*} \int_{S_c} \left\{ \tilde{\beta}_1 v_r p_n \{1 + \mu \tan \chi\} - \dot{\lambda}_F - \dot{\lambda}_M (\tilde{z} + \mu l_{\tilde{x}}) \right\} \delta p_n \, dS \, d\tau - \\ & - \frac{1}{T_*} \int_0^{T_*} \delta \dot{\lambda}_F \left(\int_{S_c} p_n \, dS - F \right) d\tau - \frac{1}{T_*} \int_0^{T_*} \delta \dot{\lambda}_M \left(\int_{S_c} (\tilde{z} + \mu l_{\tilde{x}}) p_n \, dS - M \right) d\tau = 0. \end{aligned} \quad (5.17)$$

Since the variations of contact pressure and of the rigid body wear velocity are arbitrary, the relative velocity v_r is independent of time and can be written

$$\delta \bar{L}_w = \int_{\tilde{S}_c} \left\{ \tilde{\beta}_1 v_r \bar{p}_n \{1 + \mu \tan \chi\} - \bar{\lambda}_F - \bar{\lambda}_M (\tilde{z} + \mu l_{\tilde{x}}) \right\} \delta p_n \, dS - \delta \lambda_F \left(\int_{\tilde{S}_c} \bar{p}_n \, dS - \bar{F} \right) - \delta \lambda_M \left(\int_{\tilde{S}_c} (\tilde{z} + \mu l_{\tilde{x}}) \bar{p}_n \, dS - \bar{M} \right) = 0. \quad (5.18)$$

First, we determine the contact average pressure related to wear velocity components

$$\bar{p}_n = \frac{\bar{\lambda}_F + \bar{\lambda}_M \tilde{z}}{\tilde{\beta}_1 v_r} \quad (5.19)$$

and then from the equilibrium equations for average states we have

$$\int_{\tilde{S}_c} \bar{p}_n \, dS - \bar{F} = 0, \quad \int_{\tilde{S}_c} (\tilde{z} + \mu l_{\tilde{x}}) \bar{p}_n \, dS - \bar{M} = 0, \quad (5.20)$$

where \bar{F} is calculated from (5.6). From (5.19) it follows that modified contact pressure $\tilde{\beta}_1(\tilde{z})\bar{p}_n(\tilde{z})$ is a linear function of the \tilde{z} , but the pressure at different positions in the contact zone, where the wear parameter is constant: $\tilde{\beta}_1(\tilde{z}) = \tilde{\beta}_s$ or $\tilde{\beta}_1(\tilde{z}) = \tilde{\beta}_m$ is also linear, with differing inclination (see Figure 31).

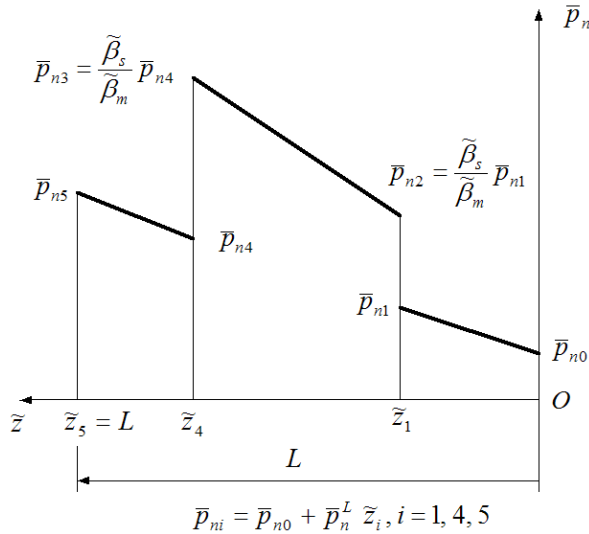


Figure 31. Average contact pressure distribution in the contact zone

When the wear parameters vary along the contact domain, then referring to Figure 31, the following system of algebraic equations for average rigid wear velocities is

used:

$$\begin{bmatrix} B_{11} & B_{12} \\ B_{21} & B_{22} \end{bmatrix} \begin{bmatrix} \bar{\lambda}_F \\ \bar{\lambda}_M \end{bmatrix} = \frac{1}{t_{\text{th}}} \begin{bmatrix} \bar{F} \\ \bar{M} \end{bmatrix} \tilde{\beta}_s v_r \quad (5.21)$$

where

$$B_{11} = \tilde{z}_1 + \frac{\tilde{\beta}_s}{\tilde{\beta}_m} (\tilde{z}_4 - \tilde{z}_1) + \tilde{z}_5 - \tilde{z}_4, \quad B_{12} = \frac{1}{2} \left[\tilde{z}_1^2 + \frac{\tilde{\beta}_s}{\tilde{\beta}_m} (\tilde{z}_4^2 - \tilde{z}_1^2) + \tilde{z}_5^2 - \tilde{z}_4^2 \right],$$

$$B_{21} = B_{12} + \mu l_{\tilde{x}} B_{11}, \quad B_{22} = \frac{1}{3} \left[\tilde{z}_1^3 + \frac{\tilde{\beta}_s}{\tilde{\beta}_m} (\tilde{z}_4^3 - \tilde{z}_1^3) + \tilde{z}_5^3 - \tilde{z}_4^3 \right] + \mu l_{\tilde{x}} B_{12}.$$

Solving (5.21), the contact pressures are expressed by the relations

$$\bar{p}_n = \frac{\bar{\lambda}_F + \bar{\lambda}_M \tilde{z}}{\tilde{\beta}_s v_r} \quad \text{if } 0 \leq \tilde{z} \leq \tilde{z}_1, \quad \tilde{z}_4 \leq \tilde{z} \leq \tilde{z}_5; \quad (5.22)$$

$$\bar{p}_n = \frac{\bar{\lambda}_F + \bar{\lambda}_M \tilde{z}}{\tilde{\beta}_m v_r} \quad \text{if } \tilde{z}_1 \leq \tilde{z} \leq \tilde{z}_4.$$

The average rigid body wear velocities for the case of uniform wear parameter $\tilde{\beta}_1(\tilde{z}) = \text{const}$ are expressed in the form

$$\bar{\lambda}_F = \tilde{\beta}_1 v_r \frac{\bar{F}}{S_c} \left[1 - \frac{6}{L} (z_F - \frac{L}{2} - \mu l_{\tilde{x}}) \right], \quad \bar{\lambda}_M = \tilde{\beta}_1 v_r \frac{\bar{F}}{S_c} \frac{12}{L^2} (z_F - \frac{L}{2} - \mu l_{\tilde{x}}) \quad (5.23)$$

and the average contact pressure distribution is

$$\bar{p}_n = \frac{\bar{F}}{S_c} \left\{ 1 + \left(-\frac{6}{L} + \frac{12}{L^2} \tilde{z} \right) (z_F - \frac{L}{2} - \mu l_{\tilde{x}}) \right\}. \quad (5.24)$$

The analysis presented referred to the specific problem of a plane punch sliding on a flat substrate. However, the method can be applied to any case of the relative sliding of two bodies for periodically varying normal load. We can therefore make a general statement.

Theorem. For the cases of periodic normal loading and monotonic relative sliding between two bodies, the average contact wear form and pressure distribution can be specified in terms of the average load from the minimization of the wear dissipation power in one period.

Remark 1: If the punch is not allowed for rigid body rotation ($\dot{\lambda}_M = 0$, $l_{\tilde{x}} = 0$, $\tilde{z}_F = L/2$), and wear parameters are uniform, then

$$\bar{p}_n = \bar{F}/S_c, \quad S_c = t_{\text{th}} \tilde{z}_5 = t_{\text{th}} L.$$

If wear parameters are not uniform then $\bar{\lambda}_F = \frac{\bar{F}}{t_{\text{th}} B_{11}} \tilde{\beta}_s v_r$. The contact pressure then is

$$\bar{p}_n = \frac{\bar{F}}{t_{\text{th}} B_{11}} \quad \text{if } 0 \leq \tilde{z} \leq \tilde{z}_1, \quad \tilde{z}_4 \leq \tilde{z} \leq \tilde{z}_5 \quad \text{and} \quad \bar{p}_n = \frac{\bar{F}}{t_{\text{th}} B_{11}} \frac{\tilde{\beta}_s}{\tilde{\beta}_m} \quad \text{if } \tilde{z}_1 \leq \tilde{z} \leq \tilde{z}_4.$$

Remark 2: When the relative sliding velocity depends on time (for instance varies periodically), then in variational equations (5.17) and (5.18) the term $\frac{1}{T_*} \int_0^{T_*} v_r p_n d\tau = \overline{v_r p_n} = \bar{v}_r \bar{p}_n + \frac{1}{T_*} \int_0^{T_*} \tilde{v}_r \tilde{p}_n d\tau$, where \tilde{v}_r and \tilde{p}_n are the fluctuation values, so the result for the average contact pressure (5.22) will only be approximate.

6. CONCLUDING REMARKS

The present paper also demonstrated that the minimum of the wear dissipation power at $q = 1$ gives the pressure distribution of the steady wear state at arbitrary wear parameters. When the heat generation on the contact surface is accounted for, the contact pressure is the same as in the case when the heat generation is neglected, but the steady wear contact shape is totally different.

In the case of periodic sliding, the modified sum of contact pressures is determined and used to specify the accumulated wear, with no need for time integration of the wear rule.

Acknowledgement. The present research was partially supported by the Hungarian Academy of Sciences, by grant NKFIH 115701.

REFERENCES

1. I. Páczelt and Z. Mróz. “On the analysis of steady sliding wear process.” *Tribology International Journal*, **42**, (2009), pp. 275–283. DOI: 10.1016/j.triboint.2008.06.007.
2. I. Páczelt and Z. Mróz. “Numerical analysis of steady thermo-elastic wear regimes induced by translating and rotating punches.” *Computers and Structures*, **89**, (2011), pp. 2495–2521. DOI: 10.1016/j.compstruc.2011.06.001.
3. I. Páczelt and Z. Mróz. “Optimal shapes of contact interfaces due to sliding wear in the steady relative motion.” *International Journal of Solids and Structures*, **44**, (2007), pp. 895–925. DOI: 10.1016/j.ijsolstr.2006.05.027.
4. Z. Mróz and I. Páczelt. “Analysis of Thermo-Elastic Wear Problems.” *Journal of Thermal Stresses*, **34**, (2011), pp. 569–606. DOI: 10.1080/01495739.2011.564026.
5. I. Páczelt, Z. Mróz, and A. Baksa. “Analysis of steady wear processes for periodic sliding.” *Journal of Computational and Applied Mechanics*, **10**, (2015), pp. 231–268. DOI: 10.32973/jcam.2015.014.
6. I. Páczelt and Z. Mróz. “Analysis of wear processes for periodic loading.” *Key Engineering Materials*, **681**, (2015), pp. 117–141. DOI: 10.4028/www.scientific.net/KEM.681.117.
7. Z. Mróz, S. Kucharski, and I. Páczelt. “Anisotropic friction and wear rules with account for contact state evolution.” *Wear*, **396-397**, (2018), pp. 1–11. DOI: 10.1016/j.wear.2017.11.004.
8. I. G. Goryacheva. *Contact Mechanics in Tribology*. Dordrecht, Kluwer Academic Publishers, 2010. DOI: doi:10.1007/978-94-015-9048-8.

-
9. B. Szabó and I. Babuska. *Introduction to Finite Element Analysis : Formulation, Verification and Validation*. New York, Wiley-Interscience, 2011.
 10. I. Páczelt and A. Baksa. “Examination of contact optimization and wearing problems.” *Journal of Computational and Applied Mechanics*, **3**, (2002), pp. 61–84. URL: <http://www.mech.uni-miskolc.hu/jcam>.
 11. P. Wriggers. *Computational Contact Mechanics*. Springer, 2006. DOI: 10.1007/978-94-015-9048-8.
 12. I. Páczelt. “Iterative methods for solution of contact optimization problems.” *Archives of Mechanics*, **52**, (2000), pp. 685–711. URL: <http://am.ippt.pan.pl/am/article/view/v52p685>.
 13. U. Peigney. “Simulating wear under cyclic loading by a minimization approach.” *International Journal of Solids and Structures*, **41**, (2004), pp. 6783–6799. DOI: 10.1016/j.ijsolstr.2004.05.022.
 14. N. H. Kim, D. Won, D. Burris, B. Holtkamp, G. C. Gessel, P. Swanson, and W. G. Sawyer. “Finite element analysis and experiments of metal/metal wear in oscillatory contacts.” *Wear*, **258**, (2005), pp. 1787–1793. DOI: 10.1016/j.wear.2004.12.014.
 15. I. G. Goryacheva, P. T. Rajeev, and T. N. Farris. “Wear in partial slip contact.” *Journal of Tribology ASME*, **123**, (2001), pp. 848–856. DOI: 10.1115/1.1338476.
 16. I. Páczelt and Z. Mróz. “Analysis of thermo-mechanical wear problems for reciprocal punch sliding.” *Advances in Engineering Software*, **80**, (2015), pp. 139–155. DOI: 10.1016/j.advengsoft.2014.09.012.

SOME REMARKS ON THE APPLICATION OF TREFFTZ'S METHOD

GYÖRGY RICHLIK

Department of Vehicle Elements and Vehicle-Structure Analysis
Budapest University of Technology and Economics
richlik@kme.bme.hu

[Received: January 14, 2020, Accepted: April 8, 2020]

Abstract. The purpose of the present paper is to determine the Green function matrix of some simple rod structures for the extended Trefftz's method. An interesting proof is given for the sum of a well-known series.

Mathematical Subject Classification: 34L15, 34B27

Keywords: Green function matrix, Trefftz's method

1. INTRODUCTION

The estimation of natural frequencies for elastic continuous beam structures is possible in several ways, for example with the method of Trefftz. The application of this procedure essentially leads to the explicit construction of the Green function matrix. Usually a lot of work is needed to determine the elements of the Green function matrix. Nowadays, the application of some software – Maple, Mathematica, Derive, etc. – can help us to solve this problem. Our goal is to show the construction of the elements of the Green function matrix in the case of a simple frame structure. In connection with our example we are going to deal with the sum of a well-known series. We remark that the concept of the Green function matrices using a bit different approach can be attributed to G. Obádovics and G. Szeidl [1–3].

2. SUMMARY OF AN EXTENSION OF TREFFTZ'S METHOD

Consider the interval $[a, b] = \{t \in \mathfrak{R} : a \leq t \leq b \ a, b \in \mathfrak{R}\}$ denote the set of all Lebesgue integrable n -vector functions with real-valued coordinates by $L^2(a, b)$ where \mathfrak{R} is the set of all real numbers. If $\mathbf{x}, \mathbf{y} \in L^2(a, b)$ are n -vector functions with the property that the product $\mathbf{y}^T \mathbf{x}$ is integrable, then

$$\langle \mathbf{x}, \mathbf{y} \rangle = \int_a^b \mathbf{y}(t)^T \mathbf{x}(t) dt \quad (1)$$

is the inner product. If \mathbf{A} is an invertible differential operator then, on the basis of [4], its inversion is given by the formula

$$\mathbf{x}(t) = (\mathbf{A}^{-1}\mathbf{y})(t) = \int_a^b \mathbf{G}(t, s)\mathbf{y}(s) ds. \quad (2)$$

Its kernel is the function matrix $\mathbf{G}(\mathbf{t}, \mathbf{s})$, which we can find by using

$$(\mathbf{A}\mathbf{x})(t) = \int_a^b (\mathbf{A}\mathbf{G})(t, s)\mathbf{y}(s)ds = \mathbf{y}(t). \quad (3)$$

According to [4] and (3) we have the following equations:

$$\mathbf{A}\mathbf{G} = \delta_{\mathbf{A}}, \quad \mathbf{M}\mathbf{G} = \mathbf{0}, \quad (4)$$

where the boundary conditions are given by the relation $\mathbf{M}\boldsymbol{\xi} = \mathbf{0}$, $\delta_{\mathbf{A}} = \delta\mathbf{E}$, while \mathbf{E} is a unit matrix and δ is Dirac's distribution [5].

Let \mathbf{A}^{-1} be a real symmetric positive compact self-adjoint operator. Then $\mathbf{G}(t, s) = \mathbf{G}(s, t)$, $\forall t, s \in [a, b]$ and the eigenvalues λ_i of \mathbf{A}^{-1} are all real and nonnegative. Moreover we have [4, 5]

$$\int_a^b \text{Spur } \mathbf{G}(t, t)dt = \sum_k \lambda_k \quad (5)$$

and if $j \leq k$ then, according to Trefftz [6] and (5) we obtain an estimation of the j^{th} eigenvalue

$$\lambda_j \leq \mu_j + \int_a^b \text{Spur } \mathbf{G}(t, t)dt - \sum_{i=1}^k \mu_i := \nu_j \quad (6)$$

in which μ_j is a lower bound for the j^{th} eigenvalue. Equation (6) is a new extension of Trefftz's method - see equation (3.5) in [4] for further details.

3. A SIMPLE BEAM STRUCTURE

Let us consider the bending vibrations of a simply supported uniform beam divided mentally into two parts (Figure 1).

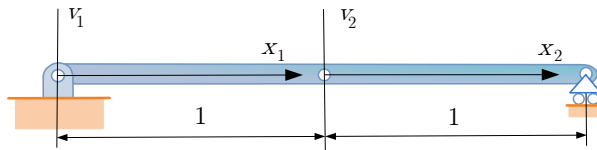


Figure 1. Simply supported beam

If $x_1, x_2 \in [0, 1]$ then the boundary value problem [7] is

$$\mathbf{A}\mathbf{v} - \alpha^2\mathbb{B}\mathbf{v} = \mathbf{0} \quad (7)$$

where

$$\mathbf{v} = \begin{bmatrix} v_1(x_1) \\ v_2(x_2) \end{bmatrix}, \quad \mathbf{A}\mathbf{v} = \begin{bmatrix} \frac{d^4}{dx_1^4} & 0 \\ 0 & \frac{d^4}{dx_2^4} \end{bmatrix} \begin{bmatrix} v_1(x_1) \\ v_2(x_2) \end{bmatrix}, \quad \mathbf{B}\mathbf{v} = \frac{q^2}{p^2} \begin{bmatrix} v_1(x_1) \\ v_2(x_2) \end{bmatrix}, \quad (8)$$

α is the natural circular frequency, while p and q depend on the material and geometrical parameters of the beam. Equation (7) is associated with the following boundary conditions:

$$\begin{aligned} v_1(0) = \frac{d^2 v_1}{dx_1^2}(0) = v_2(1) = \frac{d^2 v_2}{dx_2^2}(1) = 0, \quad v_1(1) = v_2(0), \\ \frac{dv_1}{dx_1}(1) = \frac{dv_2}{dx_2}(0), \quad \frac{d^2 v_1}{dx_1^2}(1) = \frac{d^2 v_2}{dx_2^2}(0), \quad \frac{d^3 v_1}{dx_1^3}(1) = \frac{d^3 v_2}{dx_2^3}(0). \end{aligned} \quad (9)$$

The operator \mathbf{A} is self-adjoint. This statement is a consequence of the transformation

$$\begin{aligned} \langle \mathbf{A}\mathbf{u}, \mathbf{v} \rangle &= \int_0^1 \begin{bmatrix} \frac{d^4 u_1(x)}{dx^4} & \frac{d^4 u_2(x)}{dx^4} \end{bmatrix}^T \begin{bmatrix} v_1(x) \\ v_2(x) \end{bmatrix} dx = \\ &= \int_0^1 \left[v_1(x) \frac{d^4 u_1(x)}{dx^4} + v_2(x) \frac{d^4 u_2(x)}{dx^4} \right] dx = \\ &= [\dots]_0^1 + \int_0^1 \left[u_1(x) \frac{d^4 v_1(x)}{dx^4} + u_2(x) \frac{d^4 v_2(x)}{dx^4} \right] dx = \\ &= \int_0^1 \begin{bmatrix} u_1(x) & u_2(x) \end{bmatrix}^T \begin{bmatrix} \frac{d^4 v_1(x)}{dx^4} \\ \frac{d^4 v_2(x)}{dx^4} \end{bmatrix} dx = \langle \mathbf{u}, \mathbf{A}\mathbf{v} \rangle \quad \forall \mathbf{u}, \mathbf{v} \in L^2(0, 1) \end{aligned}$$

in which $[\dots]_0^1 = 0$ due to the boundary conditions.

According to (4) we have the following equations:

$$\begin{aligned} \frac{d^4 G_{ii}(x, t)}{dx^4} &= \delta(x - t), \quad i = 1, 2, \\ \frac{d^4 G_{ij}(x, t)}{dx^4} &= 0 \quad i, j = 1, 2 \wedge i \neq j. \end{aligned} \quad (10)$$

After solving differential equations (10) the elements of the Green function matrix for the beam shown in Figure 1 are given by

$$\begin{aligned} G_{ii}(x, t) &= H(x - t) \int_t^x \int_t^u (s - t) ds du + \\ &+ \frac{x^3}{6} \beta_{ii}^1(t) + \frac{x^2}{2} \beta_{ii}^2(t) + x \beta_{ii}^3(t) + \beta_{ii}^4(t), \quad i = 1, 2 \end{aligned}$$

and

$$G_{ij}(x, t) = \frac{x^3}{6}\beta_{ij}^1(t) + \frac{x^2}{2}\beta_{ij}^2(t) + x\beta_{ij}^3(t) + \beta_{ij}^4(t), \quad i, j = 1, 2 \wedge i \neq j$$

where H is Heaviside's distribution and the functions β_{ij}^k are to be determined by using the boundary conditions [5, 7].

Since \mathbf{A}^{-1} is also self-adjoint, it can easily be seen that $G_{12}(x, t) = G_{2,1}(x, t)$ since

$$G_{12}(x, t) = \frac{1}{12}x((t^3 - 3t^2 + (x^2 - 1)t - x^2 + 3))$$

and

$$G_{21}(x, t) = \frac{1}{12}t(x^3 - 3x^2 + (t^2 - 1)x - t^2 + 3).$$

It should be noted that

$$G_{11}(x, t) = H(x - t) \int_t^x \int_t^u (s - t) ds du + \frac{1}{12}x^3(t - 2) + \frac{1}{12}xt(t^2 - 6t + 8), \quad (11)$$

$$G_{22}(x, t) = H(x - t) \int_t^x \int_t^u (s - t) ds du + \frac{1}{12}x^3(t - 1) + \frac{1}{4}x^2(t - 1) + \frac{1}{12}xt(t^2 - 3t + 2) + \frac{1}{12}(t^3 - 3t^2 + 2). \quad (12)$$

Making use of (11) and (12) we can get for (5) that

$$\int_0^1 \text{Spur } \mathbf{G}(x, x) dx = \int_0^1 G_{11}(x, x) dx + \int_0^1 G_{22}(x, x) dx = \frac{8}{45}. \quad (13)$$

Consequently, there is no further objection to our applying Trefftz's method in this simple example, because the estimation (6) can now be easily used. To proceed we determine the Green function $[G(x, t) \ x, t \in [0, 2]]$ of the simply supported uniform beam:

$$G(x, t) = H(x - t) \int_t^x \int_t^u (s - t) ds du + \frac{1}{12}x^3(t - 2) + \frac{1}{12}xt(t^2 - 6t + 8).$$

Since $G(x, t) = G_{11}(x, t)$ we shall also find that

$$\int_0^2 G(x, x) dx = \frac{8}{45}.$$

4. THE SUM OF A WELL-KNOWN SERIES

Solving the frequency equation of the simply supported uniform beam shown in Figure 1, natural circular frequencies can be given by the equation

$$\alpha_n = \frac{n^2 \pi^2 p}{4q} \quad (14)$$

where n is an integer [3, 8]. Setting p and q to one, the sum of the series $\sum_n 1/n^4$ is obtained from (5):

$$\sum_n \lambda_n = \sum_n \frac{1}{\alpha_n^2} = \sum_n \frac{16}{n^4 \pi^4} = \frac{16}{\pi^4} \sum_n \frac{1}{n^4} = \frac{8}{45} = \int_0^1 \text{Spur} \mathbf{G}(x, x) dx$$

thus

$$\sum_n \frac{1}{n^4} = \frac{\pi^4}{90}. \quad (15)$$

5. CONCLUDING REMARKS

The purpose of the above discussion has been to show the determination of the Green function matrix for a simple beam structure. With the procedure shown above we can use estimation (6) in similar structures. In addition, we have obtained an interesting proof for the sum of the series (15).

REFERENCES

1. J. G. Obádovics. "On the Boundary and Initial Value Problems of Differential Equation Systems." In Hungarian. PhD thesis. Hungarian Academy of Sciences, 1967.
2. G. Szeidl. "Effect of Change in Length on the Natural Frequencies and Stability of Circular Beams." In Hungarian. PhD thesis. Department of Mechanics, University of Miskolc, Hungary, 1975. 158 pp.
3. G. Szeidl and L. P. Kiss. *Mechanical Vibrations, an Introduction*. Foundations of Engineering Mechanics. Springer, 2020. Chap. 8-10. URL: <https://www.springer.com/gp/book/9783030450731>.
4. G. Richlik. "The inverse of differential operators and an extension of Trefftz's method." *Journal of Computational and Applied Mechanics*, **1**(2), (2000), pp. 179–189.
5. G. Richlik. "Bracketing of the eigenfrequencies of ordinary differential operators with the application of Green's matrix." MA thesis. Eötvös Loránd University, Budapest, Hungary, 1985.
6. E. Trefftz. "Über Fehlerschätzung bei Berechnung von Eigenwerten." *Mathematische Annalen*, **108** (1933), pp. 595–604. DOI: 10.1007/BF01452853.

7. G. Rihlik and G. Tóth. “Application of Trefftz-Fichera’s method for improvable bracketing of the natural angular eigenfrequencies of a beam subject to bending vibration.” *Acta Technica Hungarorum*, **92**(3-4), (1981), pp. 393–404.
8. W. W. Seto. *Mechanical Vibrations*. Schaum’s Outline Series. McGraw-Hill, Singapore, 1964.

Notes for Contributors

to the Journal of Computational and Applied Mechanics

Aims and scope. The aim of the journal is to publish research papers on theoretical and applied mechanics. Special emphasis is given to articles on computational mechanics, continuum mechanics (mechanics of solid bodies, fluid mechanics, heat and mass transfer) and dynamics. Review papers on a research field and materials effective for teaching can also be accepted and are published as review papers or classroom notes. Papers devoted to mathematical problems relevant to mechanics will also be considered.

Frequency of the journal. Two issues a year (approximately 80 pages per issue).

Submission of Manuscripts. Submission of a manuscript implies that the paper has not been published, nor is being considered for publication elsewhere. Papers should be written in standard grammatical English. The manuscript is to be submitted in electronic, preferably in pdf, format. The text is to be 130 mm wide and 190 mm long and the main text should be typeset in 10pt CMR fonts. Though the length of a paper is not prescribed, authors are encouraged to write concisely. However, short communications or discussions on papers published in the journal must not be longer than 2 pages. Each manuscript should be provided with an English Abstract of about 50–70 words, reporting concisely on the objective and results of the paper. The Abstract is followed by the Mathematical Subject Classification – in case the author (or authors) give the classification codes – then the keywords (no more than five). References should be grouped at the end of the paper in numerical order of appearance. Author’s name(s) and initials, paper titles, journal name, volume, issue, year and page numbers should be given for all journals referenced.

The journal prefers the submission of manuscripts in \LaTeX . Authors should select the $\mathcal{A}\mathcal{M}\mathcal{S}\text{-}\text{\LaTeX}$ article class and are not recommended to define their own \LaTeX commands. Visit our home page for further details concerning how to edit your paper.

For the purpose of refereeing the manuscripts should be sent either to Balázs Tóth (Balazs.TOTH@uni-miskolc.hu) or György SZEIDL (Gyorgy.SZEIDL@uni-miskolc.hu).

The eventual supply of an accepted for publication paper in its final camera-ready form will ensure more rapid publication. Format requirements are provided by the home page of the journal from which sample \LaTeX files can be downloaded:

<http://www.mech.uni-miskolc.hu/jcam>

These sample files can also be obtained directly (via e-mail) from Balázs TÓTH (Balazs.TOTH@uni-miskolc.hu), upon request.

One issue of the journal and ten offprints will be provided free of charge and mailed to the correspondent author. Since JCAM is an open access journal each paper can be downloaded freely from the homepage of the journal.

The Journal of Computational and Applied Mechanics is abstracted in Zentralblatt für Mathematik and in the Russian Referativnij Zhurnal.

Secretariat of the Vice-Rector for Research and International Relations, University of Miskolc

Responsible for publication: Prof. Dr. Tamás Kékesi

Published by the Miskolc University Press under the leadership of Attila Szendi

Responsible for duplication: Works manager Erzsébet Pásztor

Number of copies printed: 75

Put to the Press on June 24, 2020

Number of permission: TNRT.2020–98.ME.

ISSN 2732–0189 (Online)

ISSN 1586–2070 (Print)

A Short History of the Publications of the University of Miskolc

The University of Miskolc (Hungary) is an important center of research in Central Europe. Its parent university was founded by the Empress Maria Teresia in Selmecebánya (today Banská Štiavnica, Slovakia) in 1735. After the first World War the legal predecessor of the University of Miskolc moved to Sopron (Hungary) where, in 1929, it started the series of university publications with the title *Publications of the Mining and Metallurgical Division of the Hungarian Academy of Mining and Forestry Engineering* (Volumes I.-VI.). From 1934 to 1947 the Institution had the name Faculty of Mining, Metallurgical and Forestry Engineering of the József Nádor University of Technology and Economic Sciences at Sopron. Accordingly, the publications were given the title *Publications of the Mining and Metallurgical Engineering Division* (Volumes VII.-XVI.). For the last volume before 1950 – due to a further change in the name of the Institution – *Technical University, Faculties of Mining, Metallurgical and Forestry Engineering, Publications of the Mining and Metallurgical Divisions* was the title.

For some years after 1950 the Publications were temporarily suspended.

After the foundation of the Mechanical Engineering Faculty in Miskolc in 1949 and the movement of the Sopron Mining and Metallurgical Faculties to Miskolc, the Publications restarted with the general title *Publications of the Technical University of Heavy Industry* in 1955. Four new series - Series A (Mining), Series B (Metallurgy), Series C (Machinery) and Series D (Natural Sciences) - were founded in 1976. These came out both in foreign languages (English, German and Russian) and in Hungarian.

In 1990, right after the foundation of some new faculties, the university was renamed to University of Miskolc. At the same time the structure of the Publications was reorganized so that it could follow the faculty structure. Accordingly three new series were established: Series E (Legal Sciences), Series F (Economic Sciences) and Series G (Humanities and Social Sciences). The latest series, i.e., the series H (European Integration Studies) was founded in 2001. The eight series are formed by some periodicals and such publications which come out with various frequencies.

Papers on computational and applied mechanics were published in the

Publications of the University of Miskolc, Series D, Natural Sciences.

This series was given the name Natural Sciences, Mathematics in 1995. The name change reflects the fact that most of the papers published in the journal are of mathematical nature though papers on mechanics also come out.

The series

Publications of the University of Miskolc, Series C, Fundamental Engineering Sciences

founded in 1995 also published papers on mechanical issues. The present journal, which is published with the support of the Faculty of Mechanical Engineering and Informatics as a member of the Series C (Machinery), is the legal successor of the above journal.



Journal of Computational and Applied Mechanics

Volume 15, Number 1 (2020)

Contents

Contributed Papers

- Endre KOVÁCS: New stable, explicit, first order method to solve the heat conduction equation 3–13
- Akintoye Olumide OYELADE: An investigation on transmission loss of clamped doubled thin plate with added mass 15–26
- István PÁCZELT, Zenon MRÓZ and Attila BAKSA: Analysis of steady state wear processes for inhomogeneous materials and varying contact loads 27–66
- György RICHLIK: Some remarks on the application of Trefftz's method 67–72